Seismic properties and anisotropy of the continental crust: Predictions based on mineral texture and rock microstructure

Bjarne S. G. Almqvist, David Mainprice

AGU PUBLICATIONS

Reviews of Geophysics

REVIEW ARTICLE
10.1002/2016RG000552

Key Points:
- A review of seismic properties of the continental crust, rock texture, mineral composition and cracked media
- Database of single-crystal elastic constants
- Description of modeling schemes currently available to model seismic properties of rocks

Supporting Information:
- Supporting Information S1
- Data Set S1

Correspondence to:
B. S. G. Almqvist,
Bjarne.Almqvist@geo.uu.se

Citation:
Almqvist, B. S. G., and D. Mainprice (2017), Seismic properties and anisotropy of the continental crust: Predictions based on mineral texture and rock microstructure, *Rev. Geophys.*, *55*, 367–433, doi:10.1002/2016RG000552.

Received 22 DEC 2016
Accepted 20 MAR 2017
Accepted article online 22 MAR 2017
Published online 21 MAY 2017

Seismic properties and anisotropy of the continental crust: Predictions based on mineral texture and rock microstructure

Bjarne S. G. Almqvist[1] and David Mainprice[2]

[1]Department of Earth Sciences, Uppsala University, Uppsala, Sweden, [2]Géosciences Montpellier, Université de Montpellier, Montpellier, France

Abstract Progress in seismic methodology and ambitious large-scale seismic projects are enabling high-resolution imaging of the continental crust. The ability to constrain interpretations of crustal seismic data is based on laboratory measurements on rock samples and calculations of seismic properties. Seismic velocity calculations and their directional dependence are based on the rock microfabric, which consists of mineral aggregate properties including crystallographic preferred orientation (CPO), grain shape and distribution, grain boundary distribution, and misorientation within grains. Single-mineral elastic constants and density are crucial for predicting seismic velocities, preferably at conditions that span the crust. However, high-temperature and high-pressure elastic constant data are not as common as those determined at standard temperature and pressure (STP; atmospheric conditions). Continental crust has a very diverse mineral composition; however, a select number of minerals appear to dominate seismic properties because of their high-volume fraction contribution. Calculations of microfabric-based seismic properties and anisotropy are performed with averaging methods that in their simplest form takes into account the CPO and modal mineral composition, and corresponding single crystal elastic constants. More complex methods can take into account other microstructural characteristics, including the grain shape and distribution of mineral grains and cracks and pores. Dynamic or active wave propagation schemes have recently been developed, which offer a complementary method to existing static averaging methods generally based on the use of the Christoffel equation. A challenge for the geophysics and rock physics communities is the separation of intrinsic factors affecting seismic anisotropy, due to properties of crystals within a rock and apparent sources due to extrinsic factors like cracks, fractures, and alteration. This is of particular importance when trying to deduce crustal composition and the state of deformation from seismic parameters.

1. Introduction

The motivation for this review is the tremendous increase in interest over the past 30 years to link seismic properties of minerals and rocks in the crust with geologic processes (tectonic processes in particular). Spurring this interest is rapid development in seismic methods and large-scale geophysical projects that allow for high-resolution imaging of the crust. Large data sets and increased resolution have stimulated a critical evaluation of seismic data that results from large and long-term seismic experiments, such as USArray (http://www.usarray.org) and similar European (e.g., AlpArray and IberArray), Chinese (NECESS Array) and Australian (WOMBAT) efforts [*Rawlinson and Fishwick*, 2011; *Liu and Niu*, 2011; *Long et al*., 2014; *AlpArray Seismic Network*, 2015; http://iberarray.ictja.csic.es/]. Seismic arrays in continental settings often yield high-resolution images of seismic velocities of the continental crust in different crustal settings. Predecessors to these recent experiments are also of importance in spurring the interest in structure and composition of the continental crust (e.g., see summary of *Mooney and Meissner* [1992]). Reflection and wide-angle refraction seismic experiments, from the late 1970s to early 1990s, should be mentioned, with prominent examples such as COCORP (Consortium for Continental Reflection Profiling) [*Oliver et al*., 1976; *Brown et al*., 1986], LITHOPROBE (probing the lithosphere) [*Clowes et al*., 1987, 1998], BIRPS (British Institutions Reflection Profiling Syndicate) [*Matthews and the BIRPS Group*, 1990], and BABEL (Baltic and Bothnian Echoes from the Lithosphere) [*BABEL Working Group*, 1990, 1993]. Additionally, seismic profiles across orogens, such as ECORS (Etude Continentale et Océanique par Réflexion et Réfraction Sismiques) [*ECORS Pyrenees team*, 1988], INDEPTH (International Deep Profiling of Tibet and the Himalaya) [e.g., *Zhao et al*., 1993; *Nelson et al*., 1996; *Brown et al*., 1996], and more recently TAIGER (Taiwan Integrated Geodynamics Research) [e.g., *Wu et al*., 2014] and HiCLIMB

(Himalayan-Tibetan Continental Lithosphere During Mountain Building) [*Nábělek et al*., 2009] have yielded crucial information on the structure of the continental crust in collisional plate tectonic settings.

Notably, seismic anisotropy has become increasingly important in the investigation of continental crust. Seismic anisotropy in upper crustal settings is often taken to be negligible, or seismic velocities were considered isotropic [e.g., *Hirn et al*., 1987], with the exception of sedimentary basins with a classical layered structure [e.g., *Sayers*, 2005]. Interpretation of seismic anisotropy is often tied to crustal ductile deformation that produces strong preferred alignment of crystallographic axes and hence texture in rocks [e.g., *Shapiro et al*., 2004; *Schulte-Pelkum et al*., 2005; *Nábělek et al*., 2009; *Ozacar and Zandt*, 2009; *Endrun et al*., 2011; *Schulte-Pelkum and Mahan*, 2014]. The integration of seismological results with mineral texture and microstructural information therefore provides a very powerful combination that enables inferences regarding deformation in different tectonic settings that are otherwise not possible [i.e., *Moschetti et al*., 2010; *Huang et al*., 2015; *Long*, 2015; *Cossette et al*., 2015a, 2015b; *Xie et al*., 2015]. A significant challenge lies in extracting the contribution of intrinsic seismic properties resulting from texture and microstructure to the overall seismic signal. In particular, to the upper crust, the crack and fracture networks have large influence on the seismic properties. The effects of fractures and cracks in more deeply situated middle and lower crust are poorly constrained but may be of importance, especially in the presence of fluids with high pore pressure. It is now established that fluids may be present down to depths of at least 9 km by direct drilling in the German Continental Deep Drilling Program (KTB) project [e.g., *Emmermann and Lauterjung*, 1997; *Huenges et al*., 1997]. Contributions from both texture and crack and fracture networks to the seismic properties and anisotropy are therefore likely throughout much of the continental crust.

Current interpretation of crustal seismic data relies on knowledge of seismic properties of rocks and rock-forming minerals. Quantified seismic properties provide the link between the seismic observations and geological characteristics, such as the modal mineral composition and deformation regime. It is therefore crucial that high-quality measurements of elastic stiffness tensors are available for the most abundant minerals, at temperature and pressure conditions relevant to the crust. The link between geophysical and geological data is based on (1) observation made on natural samples collected in the field that are thought of as representative for the crust and upper mantle and (2) constraints from experimental mineral and rock physics measurements performed in the laboratory.

Deriving seismic properties from minerals and rocks begin at the scale of a single crystal; in this context the crystal may be a synthetic or natural crystal of gem quality with few defects and well-defined homogenous composition. Many physical properties are, in fact, governed by the crystallographic properties of minerals, and their relationships are well described in textbooks by *Nye* [1957] and *Kittel* [2005]. Intrinsic crystal properties dictate the magnitude of a physical property along different crystallographic axes, and a physical property in an aggregate of crystals is determined by the statistical distribution of all crystals that make up the aggregate. Equilibrium properties, including elasticity and other physical properties of geophysical interest have symmetric physical tensor properties, with the exception of piezoelectricity [e.g., *Mainprice et al*., 2014].

The database for elastic constants of single crystals is essential for the understanding of the seismic signature of the crust, in particular for the in situ settings of the middle and lowermost crust, which are out of reach for direct sampling. In order to understand seismic properties of these regions, it is necessary to investigate samples that were once situated in the middle and lower crust, from outcrops (or drill core), xenoliths, or geological terranes exposed at Earth's surface. Laboratory measurements and predictive modeling based on mineral composition and crystal orientation data are commonly used to infer seismic wave speeds in these samples.

Most of the research on predictive seismic properties based on rock texture has focused on the mantle [e.g., *Mainprice et al*., 2000; *Fouch and Rondenay*, 2006; *Mainprice*, 2015] and how texture influences flow in the lithospheric part of the mantle [*Silver*, 1996; *Savage*, 1999; *Long*, 2013]. However, layer stripping techniques have been developed assuming layer structure in the crust [e.g., *Liu and Niu*, 2012; *Rümpker et al*., 2014], revealing significant anisotropy of converted *P* to *S* waves with splitting delay time of 0.3 s in Iran and up to 0.5 s under the Tibetan Plateau. Furthermore, it is becoming increasingly evident that the continental crust can be significantly anisotropic due to presence of fractures [e.g., *Leary et al*., 1990]. Other sources of crustal anisotropy are expected from different geological processes occurring in the crust (plastic deformation, depositional sedimentary fabrics, and emplacement of igneous rocks) [e.g., *Mainprice and Nicolas*, 1989]. Mineral textures that develop in association with these processes are important to understand in order to interpret their contribution to observed seismic anisotropy.

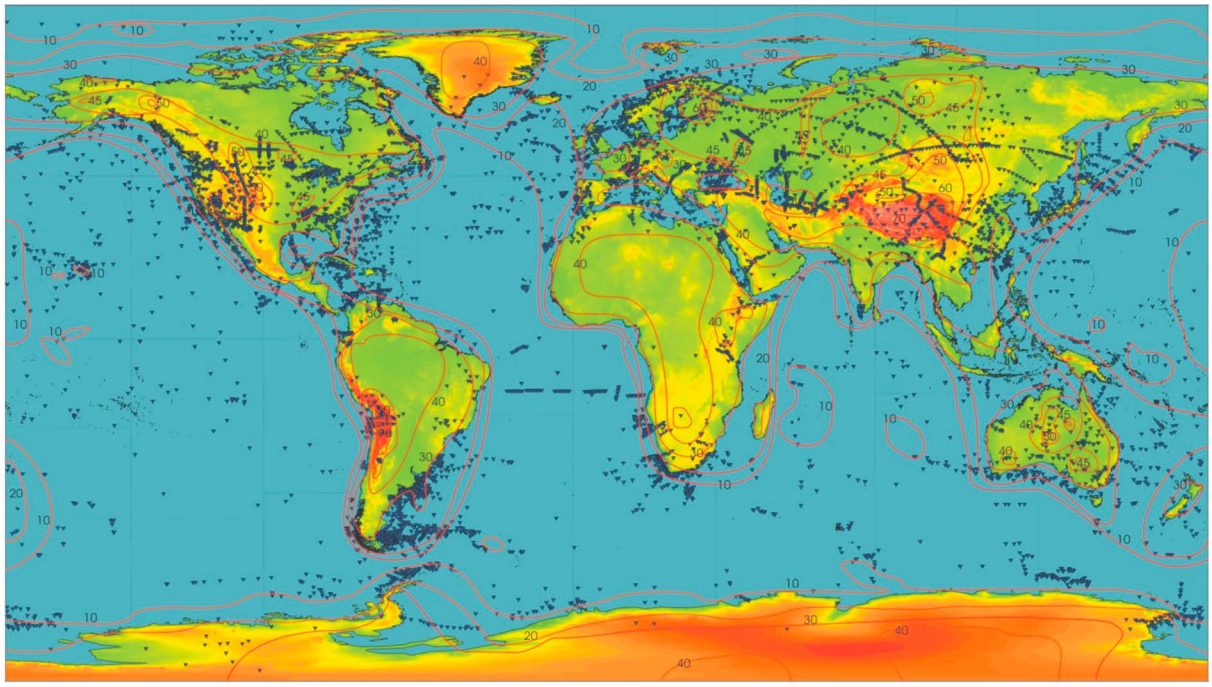

Figure 1. Crustal thickness map, adapted from *Mooney* [2015]. Red contour lines indicate 10 km intervals. Most of the continental crust vary in thickness from ~30 km to ~50 km. Exceptions are in orogenic settings (i.e., Himalaya-Tibet and the Andes) where crustal thicknesses can reach >70 km. Oceanic crust is in contrast much thinner, generally in the order of 10 km.

This review therefore addresses the state of the art of current understanding on how predictions of seismic velocity and anisotropy from mineral texture and microstructures may reveal information on the structure and composition of the continental crust and discusses future research venues that appear promising in terms of interpreting seismic characteristics from rock micro-fabric data. Particular emphasis is placed on the generally inaccessible ductile middle and lower crust regions in continental settings. The role of fractures and cracks is also covered in the predictive modeling schemes, which is particularly relevant for the upper crust but likely also of importance to the deeper crust. The manuscript is divided into five parts. The first part covers the background of crustal composition and seismic properties of crustal rocks, in general, from perspectives of laboratory measurements and predictive modeling. The second part introduces theory of elasticity and seismic wave propagation, as used in predictive modeling of seismic properties. The third part is concerned with quantification of elastic constants of minerals and provides a summary database of current elastic constants for common rock-forming minerals and references to appropriate sources for further access to elastic constants. In the fourth part, we introduce the different averaging schemes commonly used to calculate seismic properties and apply the methods to calculate seismic velocities and anisotropy for a middle crustal amphibolite from the central Scandinavian Caledonides. The fifth part discusses predicted seismic properties in sedimentary, igneous, and metamorphosed/deformed rock types, as well as in the regions of the upper, middle, and lower continental crust. This discussion also covers the different contributions of texture and microstructure and the problem of resolving the intrinsic seismic properties arising because of minerals and micro-fabric, from the apparent seismic properties as observed in seismology.

1.1. Seismic Properties of the Continental Crust

The crust refers to the outermost shell of the Earth, with the Mohorovičić (Moho) discontinuity marking its basal boundary to the underlying mantle. The position of the Moho can be ambiguous in the sense that it is considered to mark both the seismic and petrologic transitions to the mantle, although these may not necessarily coincide. The continental and oceanic crust comprises <1% by volume of planet Earth, but their importance to our planet far outweighs their contribution by volume. The crust holds the record of Earth's development through geologic time, its natural resources, and it is fundamental to societal challenges such as earthquakes and volcanic eruptions [*Mooney*, 2015]. Seismic methods have developed significantly in the

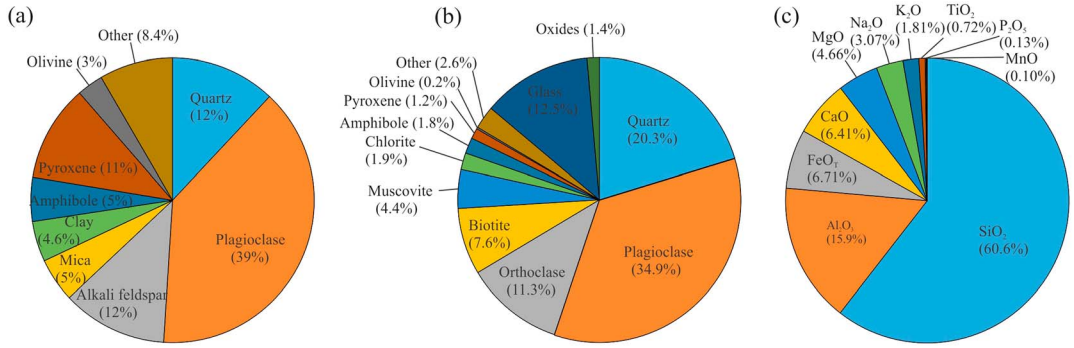

Figure 2. Composite mineral composition of the continental crust, based on compilations of (a) *Ronov and Yaroshev* [1967] and (b) *Nesbitt and Young* [1984] and later reproduced by *McLennan and Taylor* [1999]. Nesbitt and Young's compilation is based on the exposed crust at Earth's surface. (c) Average major oxide chemical composition of the continental crust based on compilation of *Rudnick and Gao* [2003].

past 25 years, yielding a highly resolved picture of the continental crust. Depth to the Moho underneath continents is generally between 30 and 50 km, but it can range from 25 to 70 km (Figure 1) [*Mooney*, 2015].

As pointed out by *McLennan and Taylor* [1999], the determination of mineral composition of continental crust is not straightforward, simply because most continental crust present at the surface may not be representative of the crust at depth. Modal mineral and chemical element composition is therefore necessarily based on the exposed crust available at the Earth's surface (Figures 2a–2c). Silicate minerals comprise by far the volumetrically most important component of the continental crust, where framework silicates (i.e., feldspars and quartz) make up ~60% by volume of the continental crust. A large number of studies have been carried out in the study of seismic properties of continental crust in relation to crustal composition, with prominent contributions from *Rudnick and Fountain* [1995], *Christensen and Mooney* [1995], *Christensen* [1996], *Rudnick and Gao* [2003, 2014], and *Hacker et al*. [2015]. *Christensen* [1996] illustrated seismic velocities and Poisson's ratio (or V_p/V_s ratio) for a range of compositions, spanning the lithologies of the crystalline crust (Figure 3). The dependence of seismic velocities on the mineral composition of the different rock types is important, but it has been remarked that velocity alone may not be a good indicator to distinguish composition (see discussion by *Hacker et al*. [2015]). The seismic properties can be divided into compressional (*P*) and shear (*S*) body wave velocities, the ratio between the *P* and *S* waves (V_p/V_s), and their directional dependence, known as seismic anisotropy. In anisotropic media the shear wave splits into two orthogonally polarized waves with fast (V_{s1}) and slow (V_{s2}) components. The effect is known as shear wave splitting ($dV_s = V_{s1} - V_{s2}$) and is analogous to the birefringence of light through an anisotropic crystal (e.g., calcite). It should be mentioned that in an isotropic media there is one V_p/V_s ratio, but in anisotropic medium there are two ratios V_p/V_{s1} and V_p/V_{s2} [e.g., *Mainprice et al*., 2008; *Mainprice and Ildefonse*, 2009]. Here we recommend using V_p/V_s rather than Poisson's ratio as it is defined as the ratio of axial strain to the transverse strain, where as V_p/V_s in the isotropic case relates to compressional and shear strains. It is physically more reasonable to use V_p/V_s or V_p/V_{s1} and V_p/V_{s2} respectively for isotropic and anisotropic media, which can be measured by seismology. For stable Cratonic crust, *Mooney* [2015] shows a general velocity profile, where the upper crust V_p ranges from 5.6 to 6.4 km/s, the middle crust V_p from 6.5 to 6.9, and the lower crust show V_p from 7.0 to 7.4 km/s. The Moho transition in a cratonic setting is marked by a sharp increase in V_p in the uppermost mantle, which ranges from ~7.8 to 8.2 km/s.

Seismic anisotropy is of particular value in studying tectonic- and deformation-related processes, but the source that gives rise to anisotropy can be challenging to identify. Crack networks and fractures, particularly in the upper continental crust, are also of relevance in directionally controlling seismic velocities. Indications exist that the stress field has an important effect on seismic anisotropy in the crust, because of crack networks orienting parallel to the maximum stress axis [*Crampin et al*., 2015]. *Lin and Schmandt* [2014] show significant azimuthal anisotropy across large portions of the upper to middle crust of the United States, where the seismic fast directions correlate with the axis of horizontal maximum stress. However, the authors also note that fast axes of maximum horizontal stress are generally parallel with the strike of the structural trend and fabric of rocks in different tectonic terranes across the United States. It can therefore be difficult to separate the seismic effects originating from oriented cracks and fractures, from the structural fabric of rocks. *Fu et al*. [2016] noted

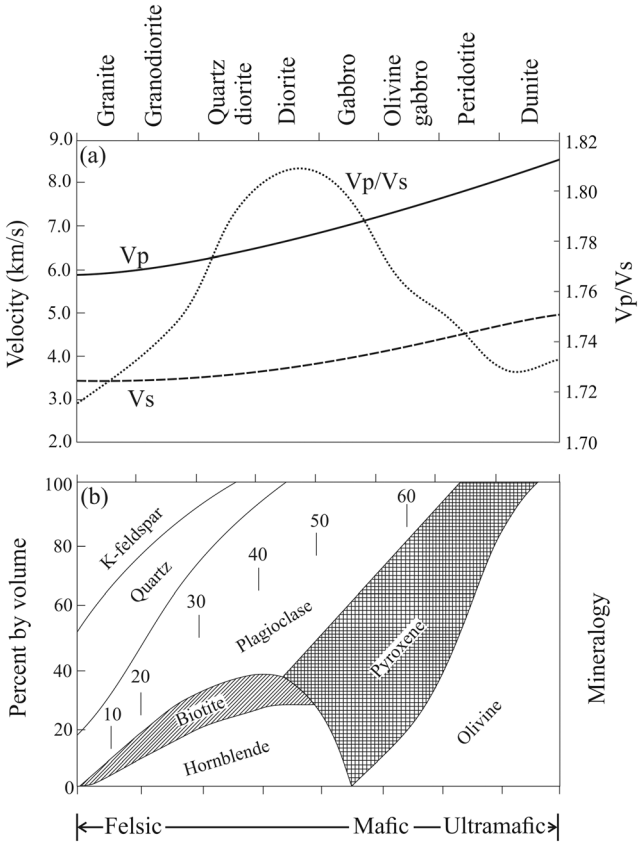

Figure 3. (a) Seismic compressional velocity (V_p), shear wave velocity (V_s), and V_p/V_s ratio, expressed as a function of crustal and upper mantle lithology. (b) Lithology (felsic, mafic, and ultramafic) as function of mineral composition. This image is modified from *Christensen* [1996].

the coincidence of fast azimuthal axis with the NE-SW maximum horizontal compressive stress axis (σ_{Hmax}) in the North China Basin and Taihang Mountains (northern China), for Rayleigh waves with a period between 10 and 16 s. However, this axis also corresponded to the strike of previous structural and mineral fabric that developed during compressional tectonics in the late Paleozoic to middle Mesozoic [*Fu et al*., 2016]. The combined effects of present-day stress field and existing structural fabric therefore probably integrate their effects on the azimuthal seismic anisotropy. At greater Rayleigh wave periods (≥25 s), corresponding to deeper crustal levels, *Fu et al*. [2016] noted a strong radial anisotropy, which they attributed to distributed lateral crustal flow that produces a crystallographic preferred orientation (CPO)-related vertical transverse isotropic (VTI) symmetry. Seismic anisotropy observed at the crust-mantle transition may be useful to distinguish deformation regimes in the lowermost crust and its possible coupling (or decoupling) to the underlying mantle. *Legendre et al*. [2015] used Rayleigh wave azimuthal anisotropy to determine that the crust is decoupled from the lithosphere in the eastern parts of the Tibetan Plateau. Based on the azimuthal anisotropy, they determined that flow regimes were different in the lower Tibetan crust, compared to the underlying lithosphere. A coincidence of seismic anisotropy in the near-lying Yangtze and Sino-Korean cratons suggested that crust and lithosphere flow were coupled in these areas [*Legendre et al*., 2015]. Another recent study indicates that deformation below the Newport-Inglewood Fault in Los Angeles Basin localized in a narrow zone that penetrates the crust and mantle portions of the lithospheric [*Inbal et al*., 2016]. This study suggests that deformation in crust and mantle may become locally coupled, and hence, anisotropic signals associated with crust and mantle deformation would be challenging to separate.

Figure 4 shows seismic V_p and V_s profiles from three contrasting tectonic settings in continental interiors, including Basin and Range (Figure 4a), central eastern Tibet (Figure 4b), and the North China Craton (Figure 4c). The Basin and Range area in western United States has been subject to intense research in terms of its geologic and tectonic development. It is considered as a classical area for extensional tectonics, chiefly through its distinct pattern of faults at the surface, which can project deeper through the upper crust using seismic reflection surveys [e.g., *Wernicke*, 1981; *Wernicke et al*., 1988; *McQuarrie and Wernicke*, 2005]. More recently, the deeper crustal structure has been studied using surface waves, which enables a link between mainly brittle upper crustal deformation with middle to lower crustal ductile flow [*Moschetti et al*., 2010; *Xie et al*., 2015] (Figure 4a). Figure 4a indicates that the Basin and Range area has fairly low V_p and V_s, with a gradually increasing V_p that is lower than 6.0 km/s in the upper and middle crust and increases abruptly to >6.3 km/s at ~17 km depth [*Lerch et al*., 2007]. The transition at the Moho is marked by a sharp transition from ~6.7 km/s to 7.9 km/s. In a similar way the V_s gradually increases, from 3.0 to 3.9 km/s, throughout the crust, but there is no marked transition from the middle to lower crust, as seen for V_p. The transition at the Moho sees a marked increase in V_s, up to 4.2 to 4.5 km/s, depending on the polarization of the shear wave

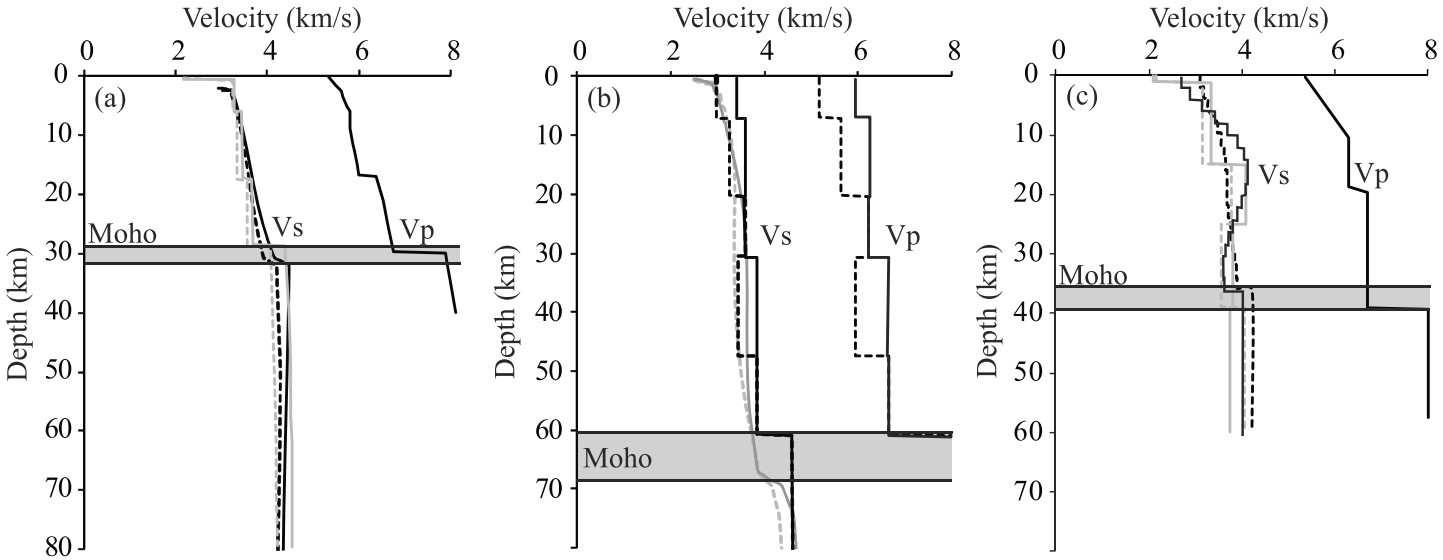

Figure 4. Seismic *P* and *S* wave velocities through three sections of continental crust. (a) Basin and Range in western United States, (b) central eastern Tibet, and (c) central North China Craton. The data shown consist of the horizontal and vertical components of *S* wave velocities (V_{sh} and V_{sv}) and the average *P* wave velocity (V_p). For V_s the solid line indicates V_{sh} and the dashed line indicates V_{sv}. Sources for the data in central eastern Tibet are *Xie et al*. [2013] and *Sherrington et al*. [2004]; *Xie et al*. [2015], *Moschetti et al*. [2010], and *Lerch et al*. [2007] for the Basin and Range profiles; and *Fu et al*. [2016], *Cheng et al*. [2013], and *Tian et al*. [2009] for the central North China Craton profiles.

(Figure 4a). *Xie et al*. [2015] identified radial anisotropy ($V_{sh} - V_{sv}/V_{s\text{-average}}$) ranging from 3 to 6% in the middle and lower crust throughout the Basin and Range area. In general, both the range and maximum strength of seismic anisotropy increases with depth, becoming largest in the lower parts of the lower crust. Using the calculated seismic velocity data of *Erdman et al*. [2013], which were calculated using a collection of geological samples from the Basin and Range province, *Xie et al*. [2015] manage to constrain the interpretation of seismic data using geological information. No anisotropy in V_p is available from the Basin and Range province.

Another region of prominent crustal flow is identified in the Tibetan part of the Himalaya-Tibet orogeny [*Royden et al*., 1997; *Shapiro et al*., 2004]. Many studies have been carried out with the goal to understand the crustal structure using the seismic signature in Himalaya-Tibet, which was the goal of the different INDEPTH projects. Surface waves and receiver functions have been used in central and eastern Tibet for the purpose of mapping seismic anisotropy throughout the crust [e.g., *Sherrington et al*., 2004; *Xie et al*., 2013; *Hacker et al*., 2014]. V_p display on average an increase from ~5.5 to 6.2 km/s throughout the upper and middle crust of this part of Tibet, although significant anisotropy is evident in the uppermost 20 km. An increase in bulk V_p is seen at ~30 km depth, which is also accompanied by strong V_p anisotropy (AV_p) from 30 km to 50 km depth; the slow V_p direction is actually slower at these depths compared to bulk V_p at shallower depths. The bulk V_s increases fairly gradually throughout the crust, from ~3.2 to 3.8 km/s. The Moho transition is marked by an abrupt increase in bulk V_s, to 4.6 km/s. Figure 4b shows the radial anisotropy related to horizontal and vertical polarized V_s, as well as V_p. Using receiver functions, *Sherrington et al*. [2004] noted a range in *S* wave anisotropy from 4% up to 14% in the crustal portion of central Tibet. They furthermore indicated that the anisotropy vary with depth and likely arise from a combination of preexisting rock fabrics and the effect of present-day deformation. The former effect was considered more important at the upper and middle crustal depths, whereas the latter was considered more important in the lower parts of the crust. Azimuthal anisotropy in middle and lower crust vary in orientation across the Tibetan Plateau, with mainly a N-S fast seismic velocity axis in the southern part of the Plateau and an E-W fast axis in the central part of the Plateau. *Xie et al*. [2013] mapped seismic anisotropy in central eastern Tibet using surface waves, and at midcrustal level they found an average radial shear wave anisotropy of 4.8% ± 1.4%, which they explained as arising from distributed flow of the ductile portion of the crust.

The last example comes from the North China Craton (NCC) in northern China (Figure 4c). A craton is generally considered fairly inactive in terms of crustal deformation, but there are indications that part of the craton

has undergone lithospheric extension since the Late Jurassic to Early Cretaceous [e.g., *Menzies and Xu*, 1998; *Kusky et al*., 2007]. A number of different explanations that give rise to crustal extension have been proposed, including delamination, chemical and thermal erosion, presence of a mantle plume, and magmatic underplating. A series of recent seismic experiments have been carried out across the NCC, with target to investigate its crustal structure [e.g., *Tian et al*., 2009; *Cheng et al*., 2009; *Fu et al*., 2016]. Bulk V_p increases gradually in the upper to middle crust, from 5.3 to 6.3 km/s. The middle to lower crust shows a fairly abrupt increase in V_p to 6.7 km/s. The Moho transition is very sharp, with an increase in V_p to 8.0 km/s. The shear wave velocity profile of the NCC is different than those observed in the Basin and Range and central eastern Tibet. A gradual increase in V_s, from 2.9 to 3.9 km/s, is observed down to ~17 km depth. Very strong shear wave anisotropy is observed at ~17 km depth. At greater depths the bulk V_s decreases gradually to a minimum of ~3.7 km/s, at the depth of the Moho. The Moho transition is sharp, and bulk V_s increases to 4.1 km/s. Both *Cheng et al*. [2013] and *Fu et al*. [2016] present strong radial seismic anisotropy at middle to lower crustal depths. In the eastern part of the NCC a thin layer with low V_{sv}, at depths from ~30 to 40 km, was identified by *Cheng et al*. [2013]. The authors explain the strong radial anisotropy (>8 %) as related to prominent extensional deformation in this part of the NCC. A more recent study by *Fu et al*. [2016] recognized azimuthal anisotropy in northern NCC, with a NW-SE fast axis trend that could be traced through the entire crust, into the upper mantle. The authors suggested that at lower crustal levels, and in the mantle, the azimuthal anisotropy is related to lithospheric-scale extension. *Fu et al*. [2016] also showed radial anisotropy, where a negative radial anisotropy occurred in the upper crust ($V_{sv} > V_{sh}$), which switched to a positive radial anisotropy ($V_{sh} > V_{sv}$) in the middle and lower crust (similar to that observed by *Cheng et al*. [2013] for eastern NCC).

1.2. Laboratory Measurements

Laboratory measurements using ultrasonic waves (e.g., pulse transmission technique) have been enormously successful in contributing fundamental data to constrain seismic velocities in rocks [e.g., *Birch*, 1960a, 1961; *Christensen*, 1965, 1971, 1979, 1996; *Fountain*, 1976; *Burlini and Fountain*, 1993; *Kern*, 1978; *Kern and Richter*, 1981; *Kern et al*., 1995, 1996, 1999, 2008; *Ji et al*., 2007]; data from such measurements have since the 1940s provided the primary constraints on crustal and upper mantle seismic interpretations. However, there are restrictions on laboratory measurements that include (1) the presence of grain boundary microcracks at standard pressure and temperature (STP) conditions, which results in lower velocity compared to rocks present in the crust; (2) rock samples affected by retrograde metamorphic alteration as they are exhumed (and exposed) at Earth's surface; and (3) limited number of orientations of rocks underdetermines the directional seismic properties, resulting in incomplete definition of elastic constants. Some remedies exist to compensate for these measurement-related restrictions. Laboratory equipment has been developed to conduct measurements at elevated pressures, in order to provide results that can be compared to rocks situated in the crust and upper mantle, thus reducing the influence of microcracks. In addition, laboratory measurements are also performed at elevated temperatures in order to simulate the effect of temperature conditions in the Earth.

The effect of pressure on closure of grain boundary cracks and porosity is an important aspect of laboratory measurements and as such warrants further discussion. As hydrostatic confining pressures exceed a specified confining pressure, the majority of pores and microcracks between grains are generally considered to be closed. The specified pressure is known as the closure pressure (P_C), and any further increase in velocity, as a function pressure, should be related to compression of the crystal structure of minerals. A range of different P_C has been reported, depending on rock type and shape of microcracks or pores [e.g., *Walsh*, 1965]. Above the P_C of grain boundary cracks and pores, the pressure derivative of the velocity may therefore be used to extrapolate velocities to pressure conditions in deeper regimes of the crust and upper mantle. *Christensen* [1974] made the observation that microcracks/pores may affect laboratory velocities to pressures exceeding 1 GPa, which jeopardizes the use of velocity pressure derivatives obtained at lower experimental pressure conditions (i.e., <1 GPa; Figure 5). Extrapolating pressure derivatives for velocities in a rock that is influenced by microcracks and pores may yield error in velocities of up to 50% [*Christensen*, 1974] compared to the case if only the velocity pressure derivatives of the crystals were considered. Crack-influenced velocity is an important factor for discrepancies between laboratory-measured elastic wave velocities and the seismic velocities predicted from rock textures.

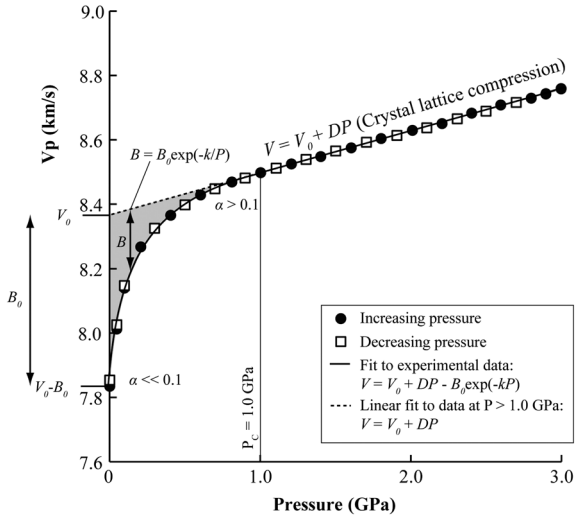

Figure 5. Pressure dependence of an ultrasonic wave, measured in the laboratory (modified from *Christensen* [1974]). At low hydrostatic confining pressure the velocity is strongly influenced by microcracks (represented by gray shaded area), whereas this effect diminishes gradually at higher pressures. α represents the aspect ratio, where thin cracks (with $\alpha \ll 1$) tend to close preferentially at low pressures, whereas cracks and pores that approach shapes of a sphere ($\alpha > 0.1$) are much harder to close and can remain open at very high confining pressure. Other variables shown in the figure are introduced in the text.

Ji et al. [2003] compared calculated seismic properties of two types of fresh eclogite from the Dabie-Sulu ultrahigh-pressure province with laboratory measurements conducted on the same material investigated by *Kern et al*. [2002]. The calculated velocities were found to be consistently higher than laboratory-measured velocities, and even at confining pressures up to 600 MPa, the difference in V_p was ~200 to 400 m/s. This indicates that microcracks were not fully closed, even at very high confining pressures used during laboratory experiments. *Ji et al*. [2007] subsequently carried out a detailed study on the influence of pressure on closure of microcracks and pores in rocks. They used a set of 66 samples obtained from surface outcrops and drill core from the Chinese Continental Scientific Drilling (CCSD) project. The sample set consisted of a range of different rock types from the Dabie-Sulu high- and ultrahigh-pressure terranes. Strong pressure dependence and hysteresis effects were found for laboratory-measured velocities at pressures <400 MPa, in samples that were taken from surface outcrops and from the shallow parts of the borehole (≤700 m depth). Samples from the deeper parts of the CCSD borehole (3000 to 4600 m depth) showed a much weaker effect of the pressure hysteresis (i.e., the velocities measured during pressurization were more similar to velocities during depressurization). The results indicate that rocks from shallower portions of the crust generally show a different response to the applied confining pressure compared to more deeply situated crustal rocks. *Ji et al*. [2007] argued that decompression of rocks creates abundant microcracks in rocks at the surface, which can potentially be in-filled with secondary minerals that cement the void spaces when filtered with supracrustal fluids. The new minerals can act as elastically soft boundaries between primary minerals and hence produce the strong dependence on pressure and hysteresis. In comparison, rocks obtained from greater depths have not previously been decompressed, and any cracks that form when exposed to ambient pressure conditions will form crack networks that are relatively easily closed during laboratory measurements. The implication is profound, because great care is needed when making comparison and extrapolation of laboratory velocities made on surface-collected (or near-surface) rocks to depths of middle to lower crustal conditions.

Several different models have been developed to derive the closure of microcracks and pores as a function of pressure [e.g., *Walsh*, 1965; *Zimmerman et al*., 1986; *Eberhart-Phillips et al*., 1989; *Wepfer and Christensen*, 1991; *Wang et al*., 2005a, 2005b; *Ji et al*., 2007; *Ullemeyer et al*., 2011; *Madonna et al*., 2012]. In Figure 5 we show application of one of the models, which is expressed by

$$V = V_0 + \mathrm{D}P - B_0 \exp(-kP) \tag{1}$$

Equation (1) uses a number of empirically fit variables to laboratory velocity data, in order to indicate the pressure dependence of the measured velocity. The equation consists of a linear portion that is related to the compression of crystal lattice, $V_0 + \mathrm{D}P$, and a nonlinear part that results from the closure of cracks during pressurization, $B_0 \exp(-kP)$. The variables used in this equation are the velocity of the rocks at zero pressure without the presence of microcracks or pores (V_0), the confining pressure (P), the pressure derivative of the velocity (D), the maximum velocity drop as a function of microcracks (B_0), and a decay coefficient (k) used

to describe the gradual closure of microcracks. *Walsh* [1965] has furthermore shown, through continuum elasticity theory, that the crack closure pressure (P_C) in an isotropic rock is strongly dependent on the geometrical shape of the cracks, where

$$P_C = \frac{\pi \alpha E}{4(1-\nu^2)} \tag{2}$$

In equation (2), E and ν are Young's modulus and Poisson's ratio, respectively, and α is the aspect ratio of the pores/cracks in the rock. The aspect ratio can vary from $\alpha = 1$ for spherical crack shape, to $\alpha \ll 1$ for thin (flat) cracks ($\alpha = a/b$, where a and b are the long and short semiaxes of an ellipsoid). As can be seen from equation (2), it is apparent that large aspect ratio cracks, close to spherical in shape, require much higher closure pressures than low aspect ratio cracks (thin cracks). Figure 5 schematically illustrates this by showing approximate closure pressures for cracks of different aspect ratios.

The experimental setups required to perform elastic wave velocity measurements generally restricts the number of experiments that can be performed with respect to different sample orientations. The number of measurements is therefore fewer than required to fully characterize the elastic tensor of geological materials with general triclinic sample symmetry. However, there are exceptions to this, such as the development of equipment that can measure ultrasonic wave speeds on sample spheres [e.g., *Pros et al*., 2003; *Lokajíček et al*., 2014], but such sample preparation is time consuming. The restriction on directional measurements in the laboratory is often not of critical importance because seismological data generally greatly underdetermine the directional dependence of velocities because such data are restricted to the radial and azimuthal velocity components.

Finally, although there are many studies of velocity and anisotropy for measurements under controlled pore pressure conditions for porous reservoir rocks [e.g., *Wyllie et al*., 1958], there are very few studies for crystalline rocks of middle and lower crust [e.g., *Todd and Simmons*, 1972; *Christensen*, 1984; *Darot and Reuschè*, 2000]. For crystalline low-porosity rocks the major control on the velocity is the effective pressure $P_e = P_c - n\ P_p$, where P_c is the confining pressure and P_p is pore fluid pressure and n is the effective pore pressure coefficient, which is typically less than 1 (note the difference of P_c and P_C, the latter which is defined as the crack closure pressure). As pore pressure increases at constant effective pressure, the value of n increases and approaches 1, but as effective pressure increases at constant pore pressure, the value of n decreases. These observations are consistent with Biot's theory for the propagation of elastic waves in a fluid-saturated porous solid [*Biot*, 1962]. It has been suggested that bright spot reflectors (i.e., reflective segments with anomalously high reflection amplitudes) at depth of ~15 km in regions of active tectonics are the result of free-water accumulation with volume fractions of ~10% in the midcrust under Tibet [e.g., *Makovsky and Klemperer*, 1999]. However, not all bright spots are interpreted as fluid accumulation as shown by *Pratt et al*. [1991] and *Barnes and Reston* [1992]. Their interpretation of bright spots from southeast Georgia, USA, at a depth of 15 km is more likely to be a thin layer of high-velocity ultramafic sheets. As southeast Georgia was tectonically active in late Palaeozoic times, it seems that the difference in interpretation could be explained by different thermal regimes in the active Tibet and old Palaeozoic suture in Georgia. Further background on poroelasticity and pore pressure effects on elastic wave propagation can be found in *Guéguen and Palciauskas* [1994], *Wang* [2000], and *Paterson and Wong* [2005].

1.3. Prediction of Seismic Properties From Mineral and Rock Textures

The schemes for predicting seismic properties of rocks follows a general procedure that requires quantitative knowledge of the mineral texture (CPO), single-crystal elastic stiffness tensors of the phases that are present (at suitable pressure and temperature conditions if temperature and pressure derivatives are of elastic constants available), and an appropriate mathematical averaging scheme to calculate the seismic properties. The crystallographic influence on velocity and anisotropy was already realized in the 1940s and 1950s, as research in resonance and ultrasonic frequency wave techniques were developing [*Firestone and Frederick*, 1946; *McSkimin*, 1950]. *Verma* [1960] presented early measurements of elastic constants for single-crystal olivine and garnet, using the ultrasonic pulse transmission technique [*McSkimin*, 1950; *Birch*, 1960a, 1960b]. The importance of anisotropy related to crystallographic axes was quickly realized and *Hess* [1964] argued that observed seismic anisotropy in the uppermost mantle in the central eastern Pacific Ocean was related to CPO of olivine, which developed because of simple shear deformation in the upper mantle.

In parallel with development of laboratory velocity measurement techniques, the field of microfabrics was gaining importance. The word "microfabric" is a general description of mineral fabric indicators in rocks and includes elements of shape-preferred orientation and crystallographic or lattice-preferred orientation (CPO and LPO) [*Paaschier and Trouw*, 2005]. The terms CPO and LPO can be considered synonymous, and in the present work we make no distinction between them but adopt the use of CPO. In the early studies the CPO was mainly measured using an optical microscope equipped with a universal stage (U-stage). Early works on the CPO of olivine-bearing rocks [e.g., *Phillips*, 1938; *Turner*, 1942] laid the foundation for the possibility to use microfabric elements in modeling the seismic properties. However, it was not until the end of the 1960s and beginning of 1970s that a series of studies emerged that combined mineral CPO measurements with single-crystal elastic constants [*Kumazawa*, 1964; *Klíma and Babuška*, 1968; *Crosson and Lin*, 1971; *Baker and Carter*, 1972]. One of the reasons for the delay in developing the predictive tools was the rather intensive computation needed to predict the seismic properties from a statistically valid number of measured crystal orientations [i.e., *Crosson and Lin*, 1971]. The Voigt and Reuss theoretical bounds [*Voigt*, 1928; *Reuss*, 1929], which had been commonly used to predict elastic properties in isotropic aggregates, were first applied in the anisotropic case by *Crosson and Lin* [1971]. Their computation enabled upper and lower theoretical bounds for an anisotropic medium. The arithmetic average of the upper and lower bounds, proposed by *Hill* [1952], could also be applied in the anisotropic case. Early calculations of texture-derived seismic velocities were tested by joint applications of laboratory measurements and rock texture studies [e.g., *Peselnick et al*., 1974]. Further verification came from predicted seismic velocities in peridotite made by *Christensen* [1984], based on a large collection of peridotite CPOs from different areas in the world. *Ben Ismaïl and Mainprice* [1998] presented a database with olivine fabrics, for 110 samples that strengthened the use of microfabrics to predict seismic velocity and seismic anisotropy. The application of predicted seismic properties from rock textures has in large part focused on olivine, because of the connection between large-scale flow and deformation in the mantle with observed seismic anisotropy. Because of the close relationship between CPO and seismic anisotropy, the latter parameter has been emphasized in prediction of seismic properties, and it has been referred to as an intrinsic source for seismic anisotropy in the seismological literature [e.g., *Fichtner et al*., 2013].

Mainprice and Nicolas [1989] and subsequently *Mainprice* [1990] provided the geological and geophysical communities with a computer program with which the CPO and single-crystal elastic properties could be mathematically combined, making it possible to infer seismic properties from crystal orientations and the mineral modal composition in rocks. The public availability of a software package to calculate seismic velocities [*Mainprice*, 1990], and software packages similar to this [i.e., *Cook et al*., 2013; *Walker and Wookey*, 2012], has popularized the use of seismic prediction using microfabrics.

The validity of predicted seismic velocities has been tested by comparison with laboratory measurements with the prediction of seismic velocities based on CPO and mineral composition. The purpose for using each of the methods is the possibility to test and validate modeled seismic velocities and also to better understand the mineralogical origin of laboratory-measured velocities. Combinations of laboratory measurements and modeled seismic velocities therefore strengthen the interpretation of seismic data, based on the identification of individual sources that contribute to the overall rock properties [e.g., *Barruol and Kern*, 1996].

2. Theory of Elasticity and Seismic Wave Propagation

2.1. Theory of Elasticity in Linear Elastic Solids

Theory of elasticity and wave propagation in elastic solids are presented in a number of works [e.g., *Landau and Lifschitz*, 1959]. A series of papers and books with focus on Earth sciences also introduce the elasticity and wave propagation background theory in anisotropic materials [*Babuska and Cara*, 1991; *Mainprice*, 2007, 2015].

The elastic constants and density determine the seismic wave velocities of a material. Elasticity is defined by Hooke's law, which explains the relationship between stress and strain in a material. In the isotropic, linear elastic case, Hooke's law is expressed as

$$\sigma_{ij} = \lambda\delta_{ij}\varepsilon_{xx} + 2\mu\varepsilon_{ij} \tag{3}$$

where σ_{ij} and ε_{ij} are the second rank stress and strain tensors, respectively, ε_{xx} is the volumetric strain, λ and μ are Lame's first and second constants, respectively, and δ_{ij} is the Kronecker delta. If subscripts $i = j$, then $\delta_{ij} = 1$,

and when $i \neq j$, then $\delta_{ij} = 0$. In other words, for an isotropic material, the elastic properties can be fully explained with knowledge of two independent elastic moduli. Seismic compressional (V_p) and shear (V_s) waves are the only two body waves in isotropic materials that can be defined by using the bulk (K) and shear (μ) moduli, as well as the density of the material. The shear modulus is Lamé's second constant and is used to define the shear wave velocity, $Vs = \sqrt{\frac{\mu}{\rho}}$ where ρ is the density, and the P wave velocity is expressed by $Vp = \sqrt{\frac{K+4/3\mu}{\rho}}$. The bulk modulus is related to the Lamé constants through the expression $K = \lambda + 2\mu/3$ and is defined as the ratio of the hydrostatic stress (σ_0) to volumetric strain (ε_{xx}), $K = \frac{\sigma_0}{\varepsilon_{xx}}$.

The anisotropic form of Hooke's law expresses the general case of the stress and strain relationship in a linear elastic solid, where

$$\sigma_{ij} = c_{ijkl}\varepsilon_{kl} \tag{4}$$

In equation (4) c_{ijkl} is the fourth-rank elastic stiffness tensor, which relates the second rank stress and strain tensors. There are $(3 \times 3)^2$ or 81 components in the stiffness tensor as a result of the second rank stress and strain tensors. However, the number of independent components is reduced to 36 because of symmetry in stress and strain tensors, because $c_{ijkl} = c_{jikl}$ and $c_{ijkl} = c_{ijlk}$. From this relationship it is possible to express the stiffness tensor in Voigt matrix notation, to condense the elastic tensor using the relationship $c_{IJ} = c_{ijkl}$, where $I = ij$ and $J = kl$. The ij and kl pairs can have six different configurations of $I(J) = ij(kl)$, which are 1 = (1, 1), 2 = (2, 2), 3 = (3, 3), 4 = (2, 3) = (3, 2), 5 = (1, 3) = (3, 1), and 6 = (1, 2) = (2, 1). As a result there are 6^2 (36) components from symmetry conditions, which are presented in a 6×6 matrix. Furthermore, because of thermodynamic strain energy conditions, $c_{ijkl} = c_{klij}$, which reduces the number of independent elastic constants to 21. The resulting 6×6 Voigt notation matrix has the appearance

$$\begin{bmatrix} c_{11} & c_{12} & c_{13} & c_{14} & c_{14} & c_{16} \\ c_{12} & c_{22} & c_{23} & c_{24} & c_{25} & c_{26} \\ c_{31} & c_{23} & c_{33} & c_{34} & c_{35} & c_{36} \\ c_{14} & c_{24} & c_{34} & c_{44} & c_{45} & c_{46} \\ c_{15} & c_{25} & c_{35} & c_{45} & c_{55} & c_{56} \\ c_{16} & c_{26} & c_{36} & c_{46} & c_{56} & c_{66} \end{bmatrix}.$$

The elasticity defined in equations (3) and (4), describing isotropic and anisotropic linear elasticity, can be related by the equation

$$c_{ijkl} = \lambda\delta_{ij}\delta_{kl} + \mu\left(\delta_{ij}\delta_{kl} + \delta_{il}\delta_{jk}\right) \tag{5}$$

The two independent elastic constants of an isotropic material are then related to the anisotropic elastic constants by the following expressions

$$c_{11} = c_{22} = c_{33} = \lambda + 2\mu \tag{6}$$

$$c_{12} = c_{23} = c_{13} = \lambda \tag{7}$$

$$c_{44} = c_{55} = c_{66} = \frac{1}{2}(c_{11} - c_{12}) = \mu \tag{8}$$

Twenty-one independent elastic constants are used to characterize elasticity for a material with the most general (triclinic) symmetry, which is the lowest possible symmetry for linear elastic tensors. Higher symmetry will reduce the number of independent elastic constants. Figure 6 shows the relationship between symmetry and the number of independent elastic constants needed to define the full elastic tensor, given specified crystal symmetry. The crystallographic convention used in Figure 6 follows *Nye* [1957].

2.2. Wave Propagation Using the Christoffel Equation

Seismic body waves are important in terms of mapping the interior of the Earth. Two types of body waves exist: the compressional or longitudinal P wave mode and the transverse or shear S wave mode. The mode of propagation of P and S waves through a material depends on the respective particle displacement in the medium. The mechanical disturbance produced by a propagating wave can be explained with a set of equations that take into account particle displacement, time, density, and the

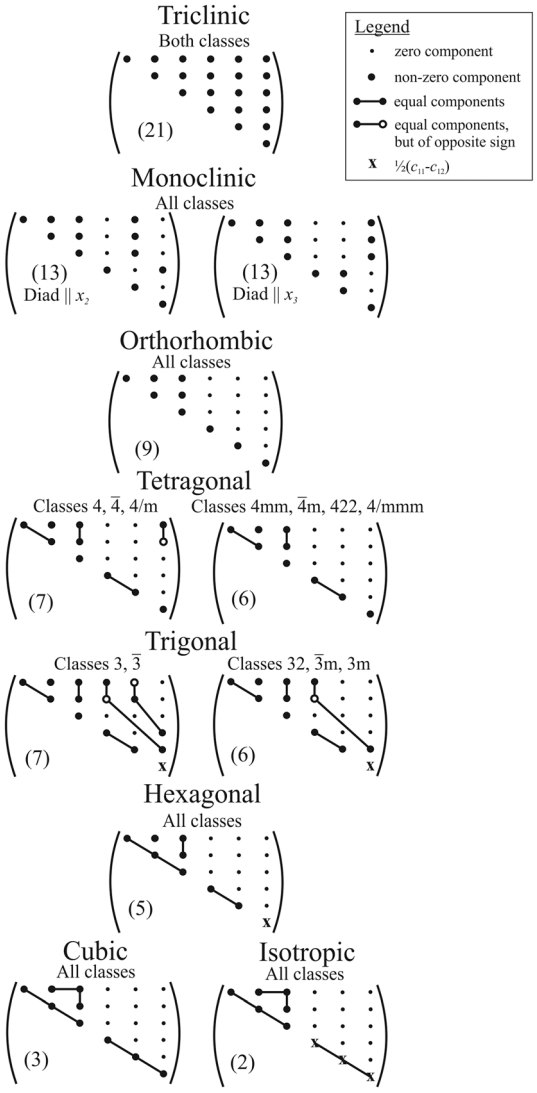

Figure 6. Elastic stiffness constants (c_{ij}) shown in the Voigt matrix form, for different crystal symmetries of the most general system (triclinic) to the highest symmetry systems (cubic and isotropic). The value in parentheses represents the number of independent elastic constants for the specific crystal symmetry. This figure is redrawn and modified from *Nye* [1957], and definition of crystal classes follows Appendix B of *Nye* [1957].

elastic properties of the medium. The theory was originally developed by *Christoffel* [1877]. The elastodynamical equation, which describes the particle displacement in an elastic medium, is written as

$$\rho\left(\frac{\partial^2 u_i}{\partial t^2}\right) = c_{ijkl}\left(\frac{\partial^2 u_l}{\partial x_j x_k}\right) \tag{9}$$

where u is the displacement, t is time, and x is position. Equation (9) can be expressed in terms of the second rank stress tensor, as defined by Hooke's law for anisotropic elasticity, such that

$$\sigma_{ij} = c_{ijkl}\left(\frac{\partial u_l}{\partial x_k}\right) \tag{10}$$

where $\partial u_l/\partial x_k$ is equivalent to the displacement or strain (ε).

Displacement for a single harmonic plane wave as a function of time (t) is given by

$$u = A \exp ik(x - ct) \tag{11}$$

where A is the amplitude vector of the wave that describes the magnitude of particle motion, $i = \sqrt{(-1)}$, k is the wave number, and c is the phase velocity. The product of the wave number (k) and the phase velocity (c) is the angular frequency (ω), $\omega = kc$; from the definition of ω, the frequency is defined as $f = \omega/2\pi$.

Combining the equation for displacement of a harmonic wave (11) with the elastodynamical equation (9) yields the *Christoffel* [1877] equation

$$C_{ijkl}s_j s_l p_k = \rho V^2 p_i \tag{12}$$

or

$$\left(C_{ijkl}n_j n_l - \rho V^2 \delta_{ik}\right)p_k = 0 \tag{13}$$

In equations (12) and (13), V is the phase velocity, ρ is the density, $p_{k,i}$ are polarization unit vectors, $s_{j,l}$ are slowness unit vectors with magnitude $1/V$, and $n_{j,l}$ are propagation directions parallel to the slowness vectors. Equation (13) can be simplified considering the Christoffel tensor $T_{ik} = C_{ijkl}n_j n_l$ and the wave moduli $M = \rho V^2$. The tensor is expressed as

$$\begin{vmatrix} T_{11} - M & T_{12} & T_{13} \\ T_{21} & T_{22} - M & T_{23} \\ T_{31} & T_{32} & T_{33} - M \end{vmatrix} = 0 \tag{14}$$

The eigenvalues of the Christoffel tensor correspond to three wave moduli (M), $\rho {V_P}^2$, $\rho {V_{S1}}^2$, and $\rho {V_{S2}}^2$, and the eigenvectors of the equation correspond to the polarization directions (or particle motions) of the three wave moduli. The polarization directions are mutually perpendicular to each other, with particle

motion parallel to the compressional wave (V_p) propagation direction and transverse particle motions for the two shear waves (V_{s1} and V_{s2}).

3. Single-Crystal Elastic Constants

The foundation for predictive modeling of seismic properties is input data of single-crystal elastic constants. A large number of experimental and modeling studies have been carried out to determine single-crystal elastic tensors. The most recent compilation of mineral elastic constants was provided in the work of *Isaak* [2001]. Other relevant databases were produced earlier by *Bass* [1995], *Hearmon* [1979, 1984], and *Sumino and Anderson* [1984]. However, many new measurements have been made since these compilations, which has expanded the database and remeasured and updated elastic constants for key minerals. Historically, most of the elastic constant measurements have been carried out at ambient (room) conditions, and much fewer data exist for pressure and temperature conditions applicable to the crust and deeper Earth conditions. Table 1 presents an overview of studies that have determined elastic constants for minerals that commonly occur in the continental crust, as well as accessory phases. Note that only minerals with the complete set of elastic constants are included in Table 1; references with only isotropic elastic constants for minerals are not included. Also indicated in Table 1 are the techniques used to determine the elastic constants and what pressures and temperatures (when applicable) were used during measurements. This table is designed to include as many studies as possible that target determination of mineral elastic constants. Table 2 gives a more condensed list of elastic constants and attempts to bring the most up-to-date database of single-crystal elastic constants for relevant minerals in the continental crust. In addition, web-accessible files with elastic constants (in Voigt matrix format) for a large number of minerals are available in the supporting information. This supporting information contains up-to-date single-crystal elastic constants that may be implemented with the seismic modeling packages that are discussed in this review. These files are compatible with the MTEX MATLAB package but can easily be adapted for use with other software.

The database of elastic constants for minerals is growing continuously. New measurement techniques enable more accurate determination of the elastic constants of minerals. Accurate elastic constants of minerals are important in order to allow their use to model seismic velocities, as well as for interpretation of seismic data. A brief outline of the techniques used to measure elastic constants is provided in the following section, but a more complete review of the methods used to measure single-crystal elastic constants is provided by *Bass and Zhang* [2015]. Determination of the complete set of single-crystal elastic constants for minerals is also of importance when considering isotropic aggregates. The reason for this is that modeling the elastic or seismic properties of an isotropic medium depends on crystal symmetry; it is most appropriate to use isotropic elastic moduli averaged based on the complete set of elastic constants from the single-crystal elastic tensor for Voigt-Reuss bounds, Hill average, and Hashin-Shtrikman bounds of the isotropic effective elastic moduli of polycrystals of any symmetry [e.g., *Brown*, 2015]. Furthermore, it is important to note that for seismic (and laboratory ultrasonic applications) one should use adiabatic elastic constants, as the time scale of elastic deformation is relatively short compared with time scale of thermal diffusion. In other words, thermal diffusion is too slow to achieve isothermal conditions.

3.1. Laboratory Techniques and First-Principle Calculations for Determination of Single-Crystal Elastic Constants

The most common laboratory techniques to quantify elastic constants of single crystals are ultrasonic and stimulated light (Brillouin scattering) techniques. Ultrasonic wave experiments have been performed in a variety of ways. The original time-of-flight ultrasonic wave measurements have the benefit that it is simple in setup and use [e.g., *Doraiswami*, 1947; *Birch*, 1960a; *McSkimin*, 1961]. Single crystals of minerals are used in experiments, which require very small wavelengths and consequently very high frequency waves (tens of megahertz). Early users of the ultrasonic techniques faced a problem to measure the complete set of elastic constants of low-symmetry crystals, and measurements were generally constrained to a pseudohexagonal or pseudocubic symmetry [i.e., *Aleksandrov and Ryzhova*, 1961; *Aleksandrov et al.*, 1974]. Current-day experiments dominantly use Brillouin scattering techniques, where one major advantage is the possibility to integrate measurements with increased pressure and temperature conditions (i.e., by using diamond anvil compression experiments and laser heating). However, some advanced ultrasonic techniques are in use to

AGU Reviews of Geophysics 10.1002/2016RG000552

Table 1. Compilation of References That Report Single-Crystal Elastic Constant Data[a]

Crystal System	Mineral Supergroup	Phase	Method to Measure Elastic Constants	Pressure (GPa)	Temperature (K)	Notes[b]	Reference to Elastic Constants
Cubic	Cristobalite	beta-cristobalite	Atomic first-principles calculations	RP	300–1800		*Kimizuka et al.* [2000]
	Chromite	Zinc-chromite	Ultrasonic pulse echo (sound velocities)	RP	RT		*Doraiswami* [1947]
		Chromite	Ultrasonic wedge method				
	Garnets	Almandine	Brillouin scattering	RP–12.0	RT	$Alm_{72}Py_{20}Sps_3$ Grs_3And_2	*Jiang et al.* [2004]
		Almandine-pyrope	Pulse superposition	RP–0.275	288–313		*Soga* [1967]
		Almandine-pyrope		RP	RT		*Babuska et al.* [1978]
		Grossular	Brillouin scattering	RP–10.7	RT	$Grs_{87}And_9Py_2Alm_2$	*Jiang et al.* [2004]
		Majorite	Brillouin scattering	RP	RT	Tetragonal crystal symmetry	*Pacalo and Weidner* [1997]
		Pyrope	Brillouin scattering	RP	RT-1073	Py_{100}	*Sinogeikin and Bass* [2002]
		Pyrope-majorite	Brillouin scattering	RP	RT-1073	$Py_{50}Mj_{50}$	*Sinogeikin and Bass* [2002]
		Pyrope-majorite	Brillouin scattering	RP	RT-1073	$Py_{20}Mj_{80}$	*Sinogeikin and Bass* [2002]
		Pyrope-majorite	Ultrasonic interferometry	RP–8	1000	$Py_{60}Mj_{40}$	*Gwanmesia et al.* [2009]
		Pyrope-majorite	Ultrasonic interferometry	RP–8	1000	$Py_{50}Mj_{50}$	*Gwanmesia et al.* [2009]
		Pyrope-grossular-almandine	Impulsive stimulated scattering	RP–20	RT	$Py_{51.6}Al_{31.7}Gr1_{5.8}Sp_{0.9}$	*Chai et al.* [1997b]
	Halite	Halite	Ultrasonic pulse transmission (sound velocities)	RP	RT	NaCl	*Haussühl* [1960]
	Magnetite	Magnetite	Ultrasonic interferometry	RP–8.7	RT		*Reichmann and Jacobsen* [2004]
		Magnetite	Ultrasonic pulse echo (sound velocities)	RP–1.2	120–280		*Isida et al.* [1996]
		Magnetite	X-ray diffraction (inelastic scattering)	RP–20	RT		*Lin et al.* [2014]
		Magnetite	Ultrasonic wedge method				*Doraiswami* [1947]
	Pyrite	Pyrite	Ultrasonic pulse transmission (sound velocities)	RP	RT		*Simmons and Birch* [1963]
		Pyrite	Ultrasonic wedge method				*Doraiswami* [1947]
Hexagonal and trigonal	Apatite	Fluorapatite	Ultrasonic pulse transmission (sound velocities)	RT	RP	$Ca_5F(PO_4)$	*Sha et al.* [1994]
		Hydroxyapatite	Atomic first-principles calculations				*Slepko and Demkov* [2011]
	Carbonates	Calcite	Ultrasonic pulse echo	RP–0.6	RT		*Dandekar* [1968]
		Calcite	Brillouin scattering	RP	RT		*Chen et al.* [2001]
		Dolomite					*Humbert and Plique* [1972]
	Chlorite	Clinochlore	Ultrasonic pulse transmission (sound velocities)	RP	RT	Pseudohexagonal stiffness tensor	*Aleksandrov and Ryzhova* [1961]
	Hematite	Hematite	Ultrasonic pulse transmission (sound velocities)	RP	RT		*Lebedev et al.* [1989]
		Hematite		RP	RT		*Voigt* [1928]
	Ilmenite	Ilmenite	Brillouin scattering	RP	RT	$MgSiO_3$	*Weidner and Ito* [1985]
	Quartz	Quartz	Resonance ultrasound spectroscopy (RUS)	RP	873	*b*-quartz	*Kammer et al.* [1948]
		Quartz	Ultrasonic pulse transmission (sound velocities)	RP	RT	*a*-quartz	*McSkimin et al.* [1965]

AGU Reviews of Geophysics

10.1002/2016RG000552

Table 1. (continued)

Crystal System	Mineral Supergroup	Phase	Method to Measure Elastic Constants	Pressure (GPa)	Temperature (K)	Notes[b]	Reference to Elastic Constants
		Quartz	Resonance ultrasound spectroscopy (RUS)	RP	RT	*a*-quartz	*Heyliger et al.* [2003]
		Quartz	Resonance ultrasound spectroscopy (RUS)	RP	RT-973	*a*- and *b*-quartz	*Ohno et al.* [2006]
		Quartz	Resonance ultrasound spectroscopy (RUS)	RP	303	*a*-quartz (17 separate crystals)	*Ogi et al.* [2006]
		Quartz	Brillouin scattering	RP	RT-1273	*a*- and *b*-quartz	*Lakshtanov et al.* [2007]
		Quartz	Brillouin scattering	RP– 10	RT		*Wang et al.* [2015]
Orthorhombic		Andalusite	Brillouin scattering	RP	RT		*Vaughan and Weidner* [1978]
		Cordierite	Brillouin scattering	RP	RT	$Na_{0.05}(Mg_{0.48}Fe_{0.16})_2(Al_{3.83}Si_{5.17})O_{18}.[_{0.25}H_2O, _{0.31}CO_2]$	*Toohill et al.* [1999]
		Lawsonite	Brillouin scattering	RP	RT-723		*Schilling et al.* [2003]
		Lawsonite	Brillouin scattering	RP	RT		*Sinogeikin et al.* [2000]
	Olivines	Fayalite	Resonance ultrasound spectroscopy (RUS)	RP	RT-673		*Sumino* [1979]
		Fayalite	Ultrasonic interferometry	RP–3.0	RT	Only c_{55} measured	*Webb et al.* [1984]
		Fayalite	Ultrasonic pulse transmission (sound velocities)	RP–1.0	273–313		*Graham et al.* [1988]
		Fayalite	Resonance ultrasound spectroscopy (RUS), Brillouin scattering, Ultrasonic pulse transmission	RP	RT and 300–500		*Isaak et al.* [1993]
		Fayalite	Brillouin scattering	0.3–12.1	RT		*Speziale et al.* [2004]
		Forsterite	Ultrasonic pulse transmission (sound velocities)	RP	RT	$(Mg_{91.7}Fe_{8.2})SiO_2$	*Verma* [1960]
		Forsterite	Ultrasonic pulse transmission (sound velocities)	RP–1.0	300-700		*Graham and Barsch* [1969]
		Forsterite	Ultrasonic pulse transmission (sound velocities)	RP–0.2	RT-573	Synthetic Fo_{100}	*Kumazawa and Anderson* [1969]
		Forsterite	Resonance ultrasound spectroscopy (RUS)	RP	300–1700		*Isaak et al.* [1989]
		Olivine (forsterite)	Impulsive stimulated scattering		298	San Carlos olivine (Fo_{89})	*Brown et al.* [1989]
		Forsterite	Resonance ultrasound spectroscopy (RUS)	RP	RT-1500	$Fo_{90\text{-}92}Fa_{10\text{-}8}$	*Isaak* [1992]
		Olivine (forsterite)	Ultrasonic pulse transmission (sound velocities)	RP–0.2	RT-573	$Fo_{93}Fa_7$	*Kumazawa and Anderson* [1969]
		Olivine (forsterite)	Impulsive stimulated scattering	RP–17.0	RT	San Carlos olivine (Fo_{90})	*Abramson et al.* [1997]
	Orthopyroxenes	Enstatite	Impulsive stimulated scattering	RP–12.5	RT	$Mg_{1.63}Fe_{0.17}Ca_{0.04}Mn_{0.01}(Al_{0.12}Cr_{0.01})(Si_{1.89}Al_{0.11})O_6$	*Chai et al.* [1997a]
		Enstatite	Brillouin scattering	RP	RT	En_{100}	*Weidner et al.* [1978]
		Enstatite	Brillouin scattering	RP	RT	$En_{94}Fs_6$	*Duffy and Vaughan* [1988]
		Enstatite	Brillouin scattering	RP	RT	Mg end-member orthoenstatite	*Jackson et al.* [1999]
		Enstatite	Brillouin scattering	RP	RT-1073	Mg end-member orthoenstatite	*Jackson et al.* [2007]
		Enstatite (Bronzite)	Ultrasonic pulse transmission (sound velocities)	RT–1.0	RT-623	En_{80}	*Frisillo and Barsch* [1972]
		Enstatite (Bronzite)	Ultrasonic interferometry	RP–3.0	RT	En_{80}	*Webb and Jackson* [1993]

AGU Reviews of Geophysics

10.1002/2016RG000552

Table 1. (continued)

Crystal System	Mineral Supergroup	Phase	Method to Measure Elastic Constants	Pressure (GPa)	Temperature (K)	Notes[b]	Reference to Elastic Constants
		Enstatite (Bronzite)	Ultrasonic pulse transmission (sound velocities)	RP	RT		*Kumazawa* [1969]
		Enstatite	Brillouin scattering	RP–12.0	RT	$(Mg_{1.74}Fe_{0.16}Al_{0.05}Ca_{0.04}Cr_{0.02})(Si_{1.94}Al_{0.06})O_6$	*Zhang and Bass* [2016a]
		Orthoferrosilite	Brillouin scattering	RP	RT	Fs_{100} ($FeSiO_3$)	*Bass and Weidner* [1984]
		Protoenstatite	Brillouin scattering	RP	RT	Li, Sc-bearing protoenstatite	*Vaughan and Bass* [1983]
	Sillimanite	Sillimanite	Brillouin scattering	RP	RT		*Vaughan and Weidner* [1978]
	Zoisite	Zoisite	Brillouin scattering	RP	RT	$Ca_2Al_3Si_3O_{12}(OH)$	*Mao et al.* [2007]
Tetragonal		Zircon	Ultrasonic pulse transmission (sound velocities)	RP–1.2	RT-573		*Özkan et al.* [1974]; *Özkan and Jamieson* [1978]
Monoclinic	Amphiboles	Hornblende	Ultrasonic pulse transmission (sound velocities)	RP	RT	Two hornblende crystals	*Aleksandrov and Ryzhova* [1961]; *Aleksandrov et al.* [1974]
		Glaucophane	Brillouin scattering	RT	RP		*Bezacier et al.* [2010]
		Kataphorite	Impulsive stimulated scattering	RT	RP		*Brown and Abramson* [2016]
		Pargasite	Impulsive stimulated scattering	RT	RP		*Brown and Abramson* [2016]
		Richterite	Impulsive stimulated scattering	RT	RP		*Brown and Abramson* [2016]
		Tremolite	Impulsive stimulated scattering	RT	RP		*Brown and Abramson* [2016]
	Clinopyroxenes	Diopside	Brillouin scattering	RP	RT	Elastic stiffness constants at room pressure	*Levien et al.* [1979]
		Diopside	Impulsive stimulated scattering	RP	RT	$Di_{72}Hd_9Jd_3Cr_3Ts_{12}$	*Collins and Brown* [1998]
		Diopside	Resonance ultrasound spectroscopy (RUS)	RP	RT	$Di_{93}Hd_3Ur_2X_2$	*Isaak and Ohno* [2003]
		Diopside	Resonance ultrasound spectroscopy (RUS)	RP	1300	$Di_{93}Hd_3Ur_2X_2$	*Isaak et al.* [2006]
		Diopside	Atomic first-principles calculations	0–20.0	RT		*Walker* [2012]
		Diopside	Brillouin scattering	0–14.0	RT		*Sang and Bass* [2014]
		Omphacite	Brillouin scattering	RP	RT	$Di_{34.1}Jd_{65.9}$	*Bhagat et al.* [1992]
		Jadeite	Brillouin scattering	RP	RT	$Jd_{99}X_1$	*Kandelin and Weidner* [1988a]
		Jadeite	Atomic first-principles calculations	0–20.0	RT		*Walker* [2012]
		Hedenbergite	Brillouin scattering	RP	RT		*Kandelin and Weidner* [1988b]
	Clay minerals	Illite-smectite	Atomic first-principles calculations	RP			*Militzer et al.* [2011]
		Dickite	Atomic first-principles calculations	RP			*Militzer et al.* [2011]
	Coesite	Coesite	Brillouin scattering	RP	RT		*Weidner and Carleton* [1977]
	Epidote	Epidote	Ultrasonic pulse transmission (sound velocities)	RP	RT		*Ryzhova et al.* [1966]
		Epidote	Ultrasonic pulse transmission (sound velocities)	RP	RT		*Aleksandrov et al.* [1974]
	Gypsum	Gypsum	Ultrasonic methods				*Haussühl* [1965]
	Phyllosilicates	Biotite	Ultrasonic pulse transmission (sound velocities)	RP	RT	Pseudohexagonal symmetry	*Aleksandrov and Ryzhova* [1961]
		Muscovite	Brillouin scattering	RP	RT		*Vaughan and Guggenheim* [1986]
		Muscovite	Atomic first-principles calculations	RP	RT		*Militzer et al.* [2011]

AGU Reviews of Geophysics 10.1002/2016RG000552

Table 1. (continued)

Crystal System	Mineral Supergroup	Phase	Method to Measure Elastic Constants	Pressure (GPa)	Temperature (K)	Notes[b]	Reference to Elastic Constants
		Phlogopite	Atomic first-principles calculations	RP–10.6	RT		*Chheda et al.* [2014]
		Phlogopite	Ultrasonic pulse transmission (sound velocities)	RP	RT	Two crystals, pseudohexagonal symmetry	*Aleksandrov and Ryzhova* [1961]
	Rutile	Rutile	Resonance ultrasound spectroscopy (RUS)	RP	RT-1800		*Isaak et al.* [1998]
		Rutile	Resonance frequency method	RP	RT		*Wachtman et al.* [1962]
		Rutile	Ultrasonic pulse transmission (sound velocities)	RP	RT		*Verma* [1960]; *Birch* [1960b]
		Stishovite					*Weidner et al.* [1982]
		alpha-cristobalite	Brillouin scattering			Low *T* form of cristobalite (<523 K)	*Kimizuka et al.* [2000]
		alpha-cristobalite	Brillouin scattering				*Yeganeh-Haeri et al.* [1992]
	Titanite	Titanite	Ultrasonic pulse transmission (sound velocities)	RP	108–300	$SrTiO_3$; pseudocubic symmetry	*Bell and Rupprecht* [1963]
Triclinic	Clay minerals	Ideal kaolinite	Atomic first-principles calculations	RP	RT		*Militzer et al.* [2011]
		Kaolinite 2 M	Atomic first-principles calculations	RP	RT		*Militzer et al.* [2011]
		Nacrite	Atomic first-principles calculations	RP	RT		*Militzer et al.* [2011]
	Feldspars	Microcline	Ultrasonic pulse transmission (sound velocities)	RP	RT	$Or_{64.9}\ Ab_{26.6}\ An_{3.6}$	*Aleksandrov et al.* [1974]
		Albite	Impulsive stimulated scattering	RP	RT	$Ab_{100}Or_0$	*Brown et al.* [2006]
		Albite	Atomic first-principles calculations	RP–12	RT	Ab_{100}	*Mookherjee et al.* [2016]
		Sanidine	Impulsive stimulated scattering	RP	RT	$Or_{89}Ab_{11}$	*Haussühl* [1993]
		Sanidine	Impulsive stimulated scattering	RP	RT	$Or_{83}Ab_{15}$	*Waeselmann et al.* [2016]
		Orthoclase	Impulsive stimulated scattering	RP	RT	$Or_{93}Ab_7$	*Waeselmann et al.* [2016]
		Plagioclase (Anorthite)	Ultrasonic pulse transmission	RP	RT		*Ryzhova* [1964]
		Plagioclase (Anorthite)	Impulsive stimulated scattering	RP	RT	$Ab_{0\text{-}100}An_{100\text{-}0}$	*Brown et al.* [2016]
		Kyanite	Atomic first-principles			Al_2O_5	*Winkler et al.* [2001]

[a]RT—room temperature; RP—room pressure.
[b]Mineral abbreviations: Albite (Ab); Anorthite (An); Almandine (Alm); Andradite (And); Cosmochlor (Cr); Diopside (Di); Enstatite (En); Fayalite (Fa); Forsterite (Fo); Grossular (Grs); Hedenbergite (Hd); Jadeite (Jd); Majorite (Mj); Orthoclase (Or); Pyrope (Py); Spessartite (Sps); Mg-Tschermak (Ts); and Ureyite (Ur).

Table 2. Elastic Constants for the Most Commonly Occurring Rock-Forming Minerals and Accessory Minerals[a]

			C_{ij} (GPa)																							
Crystal System	Phase	Density (g/cm^3)	11	22	33	44	55	66	12	13	23	15	25	35	46	14	16	24	26	34	36	45	56	Crystal Reference Frame	Reference
Cubic	Garnet																								
	Almandine-pyrope	4.131	306.7	306.7	306.7	94.9	94.9	94.9	106.7	111.9	111.9													*X*||*a* *Y*||*b* *Z*||*c*	*Babuska et al.* [1978]
	Grossular	3.605	314.5	314.5	314.5	99.7	99.7	99.7	95.6	95.6	95.6													*X*||*a* *Y*||*b* *Z*||*c*	*Jiang et al.* [2004]
	Majorite	3.522	286.4	286.4	280.1	85.0	85.0	93.2	83.0	104.9	104.9						1.4		−1.4					*X*||*a* *Y*||*b* *Z*||*c*	*Pacalo and Weidner* [1997]
	Pyrope	3.565	299.1	299.1	299.1	93.7	93.7	93.7	106.7	106.7	106.7													*X*||*a* *Y*||*b* *Z*||*c*	*Chai et al.* [1997b]
Hexagonal/ Trigonal	Quartz																								
	α-quartz	2.650	86.6	86.6	105.8	58.2	58.2	39.9	70.4	11.9	11.9					−18.0		18.0					−18.0	*X*||*a* *Y*|| [*Z* × *X*] *Z*||*c*	*McSkimin et al.* [1965]
	α-quartzz	2.645	86.7	86.7	105.5	58.1	58.1	39.9	6.9	11.9	11.9					−18.0		18.0					−18.0	*X*||*a* *Y*|| [*Z* × *X*] *Z*||*c*	*Ogi et al.* [2006]
	α-Quartz	2.650	88.2	88.2	107.2	58.5	58.5	40.9	6.5	12.4	12.4					18.8		−18.8					18.8	*X*||*a* *Y*|| [*Z* × *X*] *Z*||*c*	*Ohno et al.* [2006]
	α-quartz	2.649	86.9	86.9	106.4	59.5	59.5	39.6	7.6	12.0	12.0					17.8		−17.8					17.8	*X*||*a* *Y*|| [*Z* × *X*] *Z*||*c*	*Lakshtanov et al.* [2007]
	β-quartz (696°C)	2.523	131.1	131.1	120.5	37.4	37.4	51.7	27.8	44.0	44.0													*X*||*a* *Y*|| [*Z* × *X*] *Z*||*c*	*Ohno et al.* [2006]
	β-quartz (700°C)	2.534	128.9	128.9	119.7	37	37	50.6	27.8	44.3	44.3													*X*||*a* *Y*|| [*Z* × *X*] *Z*||*c*	*Lakshtanov et al.* [2007]
	Calcite																								
	Calcite	2.710	146.3	146.3	85.3	34.1	34.1	43.3	59.7	50.8	50.8					−20.8		20.8					−20.8	*X*||*a* *Y*|| [*Z* × *X*] *Z*||*c*	*Dandekar* [1968]
	Calcite	2.712	149.4	149.4	85.2	34.1	34.1	46.0	57.9	53.5	53.5					−20.0		20.0					−20.0	*X*||*a* *Y*|| [*Z* × *X*] *Z*||*c*	*Chen et al.* [2001]
Orthorhombic	Olivine																								
	Forsterite (San Carlos)	3.355	320.5	196.5	233.5	64.0	77.0	78.7	68.1	71.6	76.8													*X*||*a* *Y*||*b* *Z*||*c*	*Abramson et al.* [1997]
	Fayalite (0.3 GPa)	4.399	273.0	174.0	236.0	34.4	48.0	60.0	104.0	97.0	97.0													*X*||*a* *Y*||*b* *Z*||*c*	*Speziale et al.* [2004]
	Lawsonite	3.090	226.0	216.0	262.0	64.0	59.0	18.0	66.0	64.0	83.0													*X*||*a* *Y*||*b* *Z*||*c*	*Schilling et al.* [2003]

AGU Reviews of Geophysics

10.1002/2016RG000552

AGU Reviews of Geophysics

10.1002/2016RG000552

Table 2. (continued)

			C_{ij} (GPa)																							
Crystal System	Phase	Density (g/cm^3)	11	22	33	44	55	66	12	13	23	15	25	35	46	14	16	24	26	34	36	45	56	Crystal Reference Frame	Reference
	Orthopyroxenes																								
	Orthoenstatite ($MgSiO_3$)	3.204	224.7	177.9	213.6	77.6	75.9	81.6	72.4	54.1	52.7													*X*||*a Y*||*b Z*||*c*	*Weidner et al.* [1978]
	Orthoenstatite ($MgSiO_3$)	3.194	233.0	171.0	216.0	83.0	79.0	77.0	73.0	56.0	50.0													*X*||*a Y*||*b Z*||*c*	*Jackson et al.* [1999]
	Enstatite	3.306	236.9	180.5	230.4	84.3	79.4	80.1	79.6	63.2	56.8													*X*||*a Y*||*b Z*||*c*	*Chai et al.* [1997a]
	Bronzite ($Mg_{0.8}Fe_{0.2}SiO_3$)	3.354	228.6	160.5	210.4	81.8	75.5	77.7	71.0	54.8	46.0													*X*||*a Y*||*b Z*||*c*	*Frisillo and Barsch* [1972]
	Ferrosilite ($FeSiO_3$)	4.002	198.0	136.0	175.0	59.0	58.0	49.0	84.0	72.0	55.0													*X*||*a Y*||*b Z*||*c*	*Bass and Weidner* [1984]
Monoclinic	Phyllosilicates and clay minerals																								
	Biotite	3.215	186.0	186.0	54.0	58.0	58.0	76.8	32.4	11.6	11.6													*X*||*a Y*|| $[Z \times X]$ *Z*||*c**	*Aleksandrov and Ryzhova* [1961]
	Muscovite	2.830	181.0	178.4	58.6	16.5	19.5	72.0	48.8	25.6	21.2	−14.2	1.1	1.0	−5.2									*X*||$[Y \times Z]$ *Y*|| *b** *Z*||*c*	*Vaughan and Guggenheim* [1986]
	Phlogopite	2.872	181.0	185.0	62.0	14.0	20.0	68.0	48.0	12.0	12.0	−16.0	−5.0	−1.0	−6.0									*X*||*a** *Y*|| *b Z*||*c*	*Chheda et al.* [2014]
	Illite-smectite	2.825	153.9	188.5	27.2	10.4	24.8	55.4	25.1	13.2	5.2	−30.3	−8.2	−5.4	−15.9									*X*||*a Y*|| $[Z \times X]$ *Z*|| $[a \times b]$	*Militzer et al.* [2011]
	Dickite	2.583	184.2	178.8	67.5	15.8	17.1	60.4	69.1	6.0	2.5	−17.8	−6.3	5.8	−4.8									*X*||*a Y*|| $[Z \times X]$ *Z*|| $[a \times b]$	*Militzer et al.* [2011]
	Clinopyroxenes																								
	Augite	3.320	180.2	153.5	216.4	70.0	51.4	58.8	65.4	72.6	35.5	−24.7	−29.9	−21.1	−2.2									*X*||*a Y*|| *b Z*||*c**	*Aleksandrov et al.* [1974]
	Diopside ($Di_{72}He_9Jd_3Cr_3Ts_{12}$)	3.327	237.8	183.6	229.5	76.5	73.0	81.6	83.5	80.0	59.9	9.0	9.5	48.1	8.4									*X*||*a** *Y*|| *b Z*||*c*	*Collins and Brown* [1998]
	Chrome-diopside	3.286	228.1	181.1	245.4	78.9	68.2	78.1	78.8	70.2	61.1	7.9	5.9	39.7	6.4									*X*||*a** *Y*|| *b Z*||*c*	*Isaak et al.* [2006]
	Jadeite	3.330	274.0	253.0	282.0	88.0	65.0	94.0	94.0	71.0	82.0	4.0	14.0	28.0	13.0									*X*||*a** *Y*|| *b Z*||*c*	*Kandelin and Weidner* [1988a]
	Omphacite	3.327	257.3	216.2	260.2	80.2	70.6	85.8	85.9	76.2	71.8	7.1	13.3	33.7	10.2									*X*||*a** *Y*|| *b Z*||*c*	*Bhagat et al.* [1992]

AGU Reviews of Geophysics 10.1002/2016RG000552

Table 2. (continued)

Crystal System	Phase	Density (g/cm^3)	C_{ij} (GPa) 11	22	33	44	55	66	12	13	23	15	25	35	46	14	16	24	26	34	36	45	56	Crystal Reference Frame	Reference
	Coesite	2.911	160.8	230.4	231.6	67.8	73.3	58.8	82.1	102.9	35.6	−36.2	2.6	−39.3	9.9									*X*||*a Y*|| *b Z*||*c**	*Weidner and Carleton* [1977]
	Amphibole																								
	Amphobole #1 Richterite1	3.027	119.2	182.2	228.0	75.6	45.9	49.2	47.5	41.2	58.2	−1.7	−5.6	−30.6	4.7									*X*||*a** *Y*|| *b Z*||*c*	*Brown and Abramson* [2016]
	Amphobole #2 Kataphorite1	3.255	122.7	184.6	223.7	70.5	42.5	45.9	50.0	44.3	59.5	−1.4	−7.1	−29.4	5.3									*X*||*a** *Y*|| *b Z*||*c*	*Brown and Abramson* [2016]
	Amphobole #3 Taramite-Tschermakite1	3.162	133.6	193.4	225.8	75.5	47.5	50.4	50.9	43.1	58.3	−0.8	−10.8	−30.3	3.8									*X*||*a** *Y*|| *b Z*||*c*	*Brown and Abramson* [2016]
	Amphobole #4 Hornblende-Tschermakite1	3.293	122.8	189.3	222.9	71.5	46.8	46.2	51.8	45.9	62.3	−0.7	−7.0	−30.0	5.4									*X*||*a** *Y*|| *b Z*||*c*	*Brown and Abramson* [2016]
	Amphobole #5 Tremolite1	3.038	108.6	191.6	230.8	77.0	50.0	48.6	48.4	37.7	59.2	1.0	−5.6	−29.6	7.9									*X*||*a** *Y*|| *b Z*||*c*	*Brown and Abramson* [2016]
	Amphobole #6 Edenite1	3.213	131.1	186.6	224.3	72.5	46.5	48.0	53.2	47.2	60.3	−1.0	−8.5	−30.3	4.4									*X*||*a** *Y*|| *b Z*||*c*	*Brown and Abramson* [2016]
	Amphobole #7 Edenite1	3.418	122.7	178.6	216.6	67.5	39.7	40.8	52.6	47.5	60.8	−2.0	−9.5	−31.0	6.3									*X*||*a** *Y*|| *b Z*||*c*	*Brown and Abramson* [2016]
	Amphobole #8 Pargasite1	3.163	141.6	197.8	225.4	75.8	49.9	51.7	57.1	49.6	60.9	−0.2	−10.9	−31.4	3.3									*X*||*a** *Y*|| *b Z*||*c*	*Brown and Abramson* [2016]
	Amphobole #9 Pargasite1	3.190	148.7	204.6	232.1	76.7	54.1	52.9	56.5	48.8	61.9	0.3	−6.9	−28.8	1.9									*X*||*a** *Y*|| *b Z*||*c*	*Brown and Abramson* [2016]
	Hornblende (#1)	3.124	115.8	159.0	191.3	58.8	31.7	38.5	49.3	63.0	65.3	−5.5	−18.7	−8.7	−6.6									*X*||*a Y*|| *b Z*||*c**	*Aleksandrov et al.* [1974]
	Hornblende (#2)	3.153	129.3	179.6	205.9	61.7	39.4	44.5	61.7	62.8	59.7	−12.4	−13.7	−24.5	−1.9									*X*||*a Y*|| *b Z*||*c**	*Aleksandrov et al.* [1974]
	Glaucophane	3.070	121.5	229.7	256.2	79.3	52.9	51.3	44.4	37.4	75.8	2.7	−4.9	−23.9	9.3									*X*||*a Y*|| *b Z*||*c**	*Bezacier et al.* [2010]
	Alkali feldspars																								
	Sanidine ($Or_{83}Ab_{15}$)	2.567	69.3	176.2	160.8	19.2	19.4	33.4	41.6	24.0	14.3	0.3	−9.4	7.1	−11.5									*X*||*a** *Y*|| *b Z*||*c*	*Waeselmann et al.* [2016]
	Sanidine ($Or_{89}Ab_{11}$)	2.560	68.6	176.8	159.9	19.3	18.0	33.5	43.6	26.0	21.0	−0.7	−12.6	6.9	−10.8									*X*||*a** *Y*|| *b Z*||*c*	*Haussühl* [1993] rotated by Waeselmann *et al.*

Reviews of Geophysics

10.1002/2016RG000552

Table 2. (continued)

Crystal System	Phase	Density (g/cm^3)	C_{ij} (GPa)																						Crystal Reference Frame	Reference
			11	22	33	44	55	66	12	13	23	15	25	35	46	14	16	24	26	34	36	45	56			
Triclinic	Orthoclase ($Or_{93}Ab_7$) Plagioclase feldspar	2.555	67.8	181.2	158.4	21.1	19.4	33.1	40.4	25.0	20.6	−1.1	−12.9	10.6	−11.6										*X*||*a** *Y*|| *b Z*||*c*	*Waeselmann et al.* [2016]
	Albite (Or_0Ab_{100})	2.623	69.9	183.5	179.5	24.9	26.8	33.5	34.0	30.8	5.5	−2.4	−7.7	7.1	−7.2	5.1	−0.9	−3.9	−5.8	−8.7	−9.8	−2.4	0.5	*X*||*a** *Y*|| *b Z*|| [*X* × *Y*]	*Brown et al.* [2006]
	An_0 (Albite)	2.623	68.3	184.3	180.0	25.0	26.9	33.6	32.2	30.4	5.0	−2.3	−7.8	7.5	−7.2	4.9	−0.9	−4.4	−6.4	−9.2	−9.4	−2.4	0.6	*X*||*a** *Y*|| *b Z*|| [*X* × *Y*]	*Brown et al.* [2016]
	An_{25} (Oligoclase)	2.650	87.1	174.9	166.1	22.9	29.0	35.0	43.9	35.4	18.0	−0.4	−2.9	4.6	−5.2	6.1	−0.6	−5.9	−6.5	−2.9	−10.7	−1.3	0.8	*X*||*a** *Y*|| *b Z*|| [*X* × *Y*]	*Brown et al.* [2016]
	An_{37} (Andesine)	2.670	96.2	189.4	171.9	23.6	33.1	35.5	46.1	38.4	15.4	−0.2	−5.1	7.2	−4.8	5.9	−0.4	−7.0	−6.8	2.2	−9.8	−1.1	1.4	*X*||*a** *Y*|| *b Z*|| [*X* × *Y*]	*Brown et al.* [2016]
	An_{48} (Andesine)	2.670	104.6	201.4	172.8	22.9	33.0	35.6	51.5	43.9	14.5	0.1	−4.8	6.9	−3.8	6.5	−0.8	−2.4	−9.9	−0.4	−5.7	−1.0	2.1	*X*||*a** *Y*|| *b Z*|| [*X* × *Y*]	*Brown et al.* [2016]
	An_{60} (Labradorite)	2.690	109.3	185.5	164.1	22.2	33.1	36.8	53.1	42.1	21.9	1.2	0.7	2.5	1.4	7.6	−7.7	−2.9	−6.8	0.2	0.7	0.2	2.8	*X*||*a** *Y*|| *b Z*|| [*X* × *Y*]	*Brown et al.* [2016]
	An_{67} (Labradorite)	2.690	120.3	193.5	171.9	24.0	35.5	37.3	54.4	40.8	16.1	2.3	3.1	2.2	0.3	9.2	−10.1	0.9	−2.9	−0.9	−0.3	0.7	3.2	*X*||*a** *Y*|| *b Z*|| [*X* × *Y*]	*Brown et al.* [2016]
	An_{78} (Bytownite)	2.710	120.4	191.6	163.7	23.3	32.8	35.0	56.6	49.9	26.3	3.2	5.4	1.7	0.9	9.0	−3.0	2.1	−9.9	1.7	−8.1	0.8	4.5	*X*||*a** *Y*|| *b Z*|| [*X* × *Y*]	*Brown et al.* [2016]
	An_{96} (Anorthite)	2.730	132.2	200.2	163.9	24.6	36.6	36.0	64.0	55.3	31.9	5.1	3.5	0.5	−2.2	9.5	−10.8	7.5	−7.2	6.6	1.6	3.0	5.2	*X*||*a** *Y*|| *b Z*|| [*X* × *Y*]	*Brown et al.* [2016]
	Clay minerals Kaolinite	2.599	169.1	179.7	81.1	17.0	26.6	57.6	66.1	15.4	10.2	−34.0	−16.1	6.7	−12.4	−0.4	−7.8	−3.4	−0.1	−2.9	−0.1	−0.7	1.1	*X*||*a Y*|| [*Z* × *X*] *Z*|| [*a* × *b*]	*Militzer et al.* [2011]
	Nacrite	2.607	131.8	157.9	75.0	13.2	17.7	62.2	41.5	10.2	14.0	−16.0	−3.8	9.3	−9.4	0.6	0.1	0.4	0.1	0.5	0.1	−0.5	−0.1	*X*||*a Y*|| [*Z* × *X*] *Z*|| [*a* × *b*]	*Militzer et al.* [2011]

[a]The numbers of amphibole single crystal refer to *Brown and Abramson*'s [2016] experimental study. || means parallel to.

measure elastic constants, including ultrasonic interferometry [e.g., *Reichmann and Jacobsen*, 2004] and resonance ultrasound spectroscopy (RUS) [e.g., *Heyliger et al*., 2003; *Ogi et al*., 2006; *Ohno et al*., 2006; *Isaak et al*., 2006].

In addition to laboratory measurements, it is possible to theoretically calculate elastic constants of single crystals through theoretical and numerical ab initio first-principle methods. Such calculations provide a very powerful and independent way to determine elastic constants, which is of particular use at pressure and temperature conditions that are challenging to achieve experimentally and in the case of minerals that have complex (low) symmetry [e.g., *Mainprice et al*., 2008; *Militzer et al*., 2011]. Such calculations may also be used to fill gaps of missing experimental elastic constant data for some minerals [e.g., *Militzer et al*., 2011; *Walker*, 2012]. Because some minerals occur in greater abundance in the crust (Figure 2), we proceed to discuss their elastic constants as determined by different laboratory setups and computer modeling.

3.2. Plagioclase and Alkali Feldspar

Measurements of elastic constants of feldspars (plagioclase and alkali feldspar) are of particular importance to the prediction of seismic properties of the crust, for the reason that the feldspar family of minerals makes up ~50% by volume of the crust (Figure 2). Elastic constants of plagioclase feldspar, spanning the compositional range from albite ($NaSi_3AlO_3$) to anorthite ($CaSi_2Al_2O_8$), have been thoroughly investigated in a recent study by *Brown et al*. [2016]. Brown et al. used the state-of-the-art surface acoustic wave velocities measured using impulsive stimulated light scattering and compliance sums from high-pressure X-ray compression studies to accurately determine all 21 components of the triclinic plagioclases. These authors indicate that previous quantification of plagioclase elastic constants by *Ryzhova* [1964] is ~10% too low, and the newly reported plagioclase elastic constants better fit existing laboratory measurements [e.g., *Seront et al*., 1993; *Brown et al*., 2016]. Similarly, for the alkali feldspar solid solution series (albite to K-feldspar) in the compositional range $Or_{83\text{-}93}Ab_{15\text{-}7}$, *Waeselmann et al*. [2016] indicate that velocities calculated using previously determined elastic constant values [*Ryzhova and Aleksandrov*, 1965] for alkali feldspars are systematically at least 10% too slow. The difference in results likely arises because of the presence of microcracks in crystals investigated in the earlier studies by *Ryzhova* [1964] and *Ryzhova and Aleksandrov* [1965]. One of the main conclusions of recent studies of feldspars [*Brown et al*., 2016; *Waeselmann et al*., 2016] is that composition seems to be only of secondary importance. Elastic (and seismic) anisotropy in all single-crystal feldspar is considerable and can reach AV_p of nearly 50% in the case of albite and a maximum shear wave anisotropy of around 60% (Figure 7). However, because of the generally weak CPOs that develop for feldspars, it is often considered that their contribution to seismic anisotropy is of secondary importance when compared to the contribution of mica and amphibole. Nevertheless, the recent work of *Brown et al*. [2016] and *Waeselmann et al*. [2016] provides accurate determination of elastic constants for the feldspar family of minerals, which is of importance when relating the bulk *P* and *S* wave velocity in the crust with mineral composition. Seismic anisotropy arising from feldspars furthermore needs to be taken into account because of their large-volume contribution to crustal rocks. Although the work of Brown and collaborators represents a major advance in our knowledge of feldspar elasticity, at the present time we do not have measurements of the pressure or temperature derivatives of the stiffness tensors of feldspars.

Mookherjee et al. [2016] have investigated the pressure dependence of elastic constants for albite up to ~12 GPa using density functional theory. Interestingly, they found that the c_{66} elastic constant in albite decreases as a function of pressure with a minimum around 6 GPa. In contrast, c_{44} and c_{55} increase during pressurization. The body-diagonal constants c_{11} and c_{33} also showed a minimum around 6 GPa, although not as pronounced as for c_{66}; c_{22} showed increasing elasticity as a function of pressure. The elastic softening has been attributed to restructuring of tetrahedral coordinated units, TO_4 (T = Al, Si), in the framework silicate structure of albite. *Mookherjee et al*. [2016] theoretically determined values provide the only pressure derivatives available for albite (An0).

3.3. Quartz

Quartz elastic constants have been studied in detail since the 1940s [e.g., *Kammer et al*., 1948; *McSkimin et al*., 1965; *Ogi et al*., 2006]. There are several polymorphs of SiO_2 that are of relevance to crustal conditions (Figure 8). In terms of isotropic elastic constants, α-quartz and the high-temperature phase

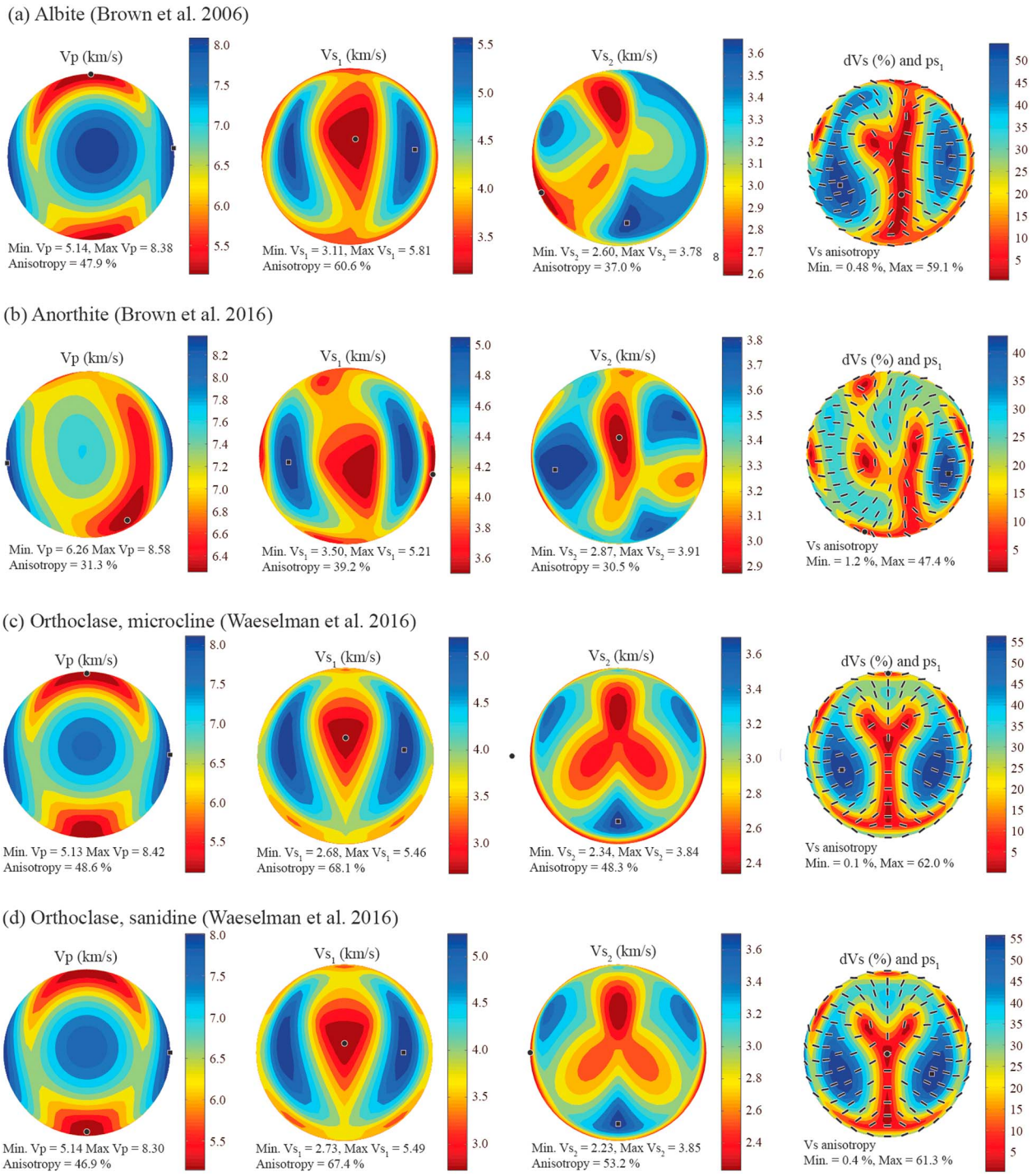

Figure 7. Feldspar single-crystal seismic properties (V_p, V_{s1}, V_{s2}, and AV_s) presented in equal-area projections at ambient conditions for (a) albite, (b) anorthite, (c) orthoclase (microcline), and (d) orthoclase (sanidine). Abbreviations are *P* wave velocity (V_p), fast polarized shear wave velocity (V_{s1}), polarized slow shear wave velocity (V_{s2}), shear wave anisotropy (dV_s), and polarization direction of V_{s1} (ps_1).

cristobalite are remarkable in the sense of having a larger shear modulus than bulk modulus (cristobalite is an auxetic material with negative Poisson ratio). The high-pressure polymorphs of coesite and stishovite are likely not of large relevance in the continental crust, although their presence in deeply subducted continental crust is important. Presence, or evidence, of coesite generally indicates an ultrahigh-pressure

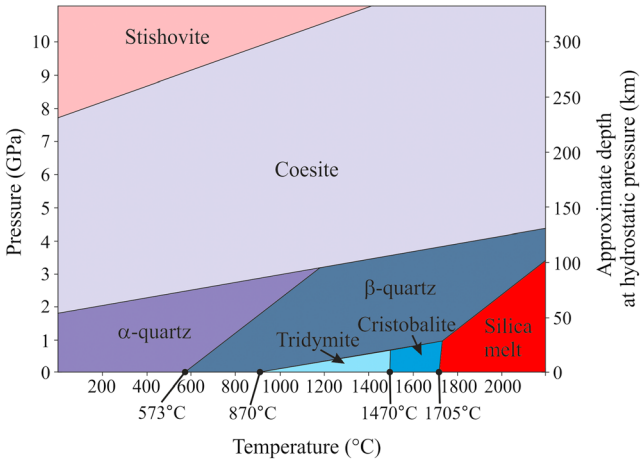

Figure 8. Phase stability diagram for SiO_2 polymorphs, modified from *Wenk and Bulakh* [2004].

metamorphic origin of the rock that is bearing the mineral. Figure 9 shows seismic properties for the different polymorphs of SiO_2, with the exception of cristobalite.

Alpha-quartz is furthermore interesting because it has $c_{33} > c_{11}$ and $c_{44} > c_{66}$, which is uncommon in other hexagonal, trigonal, and pseudohexagonal crystals. At ambient conditions quartz has the highest elastic stiffness parallel to the crystallographic *c* axis (optic axis). A particular problem concerning quartz is the α-β crystallographic transition that occurs at temperatures from 573.0 to 574.3°C [*Ohno et al*., 2006], at ambient pressure conditions. Recent studies have focused on how elasticity changes across this transition [*Ohno et al*., 2006; *Lakshtanov et al*., 2007; *Klumbach and Schilling*, 2014] (Figure 10). At higher hydrostatic pressures, the crystallographic transition is elevated, and the transition temperature increases at a rate of 25.8 ± 0.3°C/kbar in the pressure range from 1 to 5 kbar, as shown experimentally by *Coe and Paterson* [1969]. The α-β transition is of importance when considering the seismic properties of the crust, because of the considerably different elastic properties of the two polymorphs, illustrated both in laboratory measurements [*Kern*, 1979; *Zappone and Benson*, 2013] and from predictive calculations [*Mainprice and Casey*, 1990]. Seismological experiments in hot crustal settings (with high geothermal gradient) have led to the suggestion that the α-β transition is visible through changes in seismic velocities [i.e., *Mechie et al*., 2004; *Marini and Manzella*, 2005]. *Wang et al*. [2015] have measured the elastic constants to 10 GPa at room temperature.

The calculation of the elastic constants for quartz at temperature and pressure is complicated by the α-β transition. α-quartz has an unusual Poisson's ratio, thermal expansion, and stiffness constants that vary rapidly near transition in the α-quartz phase and is more or less constant in the β-phase. In the context of isotropic elasticity, *Abers and Hacker* [2016] have discussed how to model isotropic seismic velocities near the α-β transition. The transition varies with temperature and pressure and applied stress making the parameterization rather complex for case of anisotropic elasticity. The α-β transition is close to the amphibolite to granulite metamorphic division in temperature-pressure space as shown by *Mainprice and Casey* [1990], which may help determine if the quartz was in the α- or β-phase and how close to the transition.

3.4. Pyroxenes

Pyroxenes occur with orthorhombic (orthopyroxene) and monoclinic (clinopyroxene) symmetry, with 9 and 13 independent elastic constants, respectively. A number of studies have focused on measurements of the elastic constants of orthopyroxene and clinopyroxene single crystals. Most of these studies are concerned with elastic and seismic properties of pyroxene in the upper mantle, but the results are naturally applicable to the crust. The pyroxene group represents a large proportion of the crustal mineral inventory (Figure 2). However, given the broad compositional range of pyroxenes, there is a considerable gap in terms of mapping the effect of pyroxene chemistry on elastic constants. A summary of details of the different measurements made on pyroxenes and their composition is provided in Table 1, and Figure 11 shows calculated seismic velocities and anisotropy for commonly occurring orthopyroxene and clinopyroxene.

Orthopyroxene elastic constants for the solid solution series of orthoenstatite ($MgSiO_3$) to ferrosilite ($FeSiO_3$) have been presented in a number of studies. Elastic constants for the pure, or nearly pure, enstatite endmember have been presented at room conditions, and elevated pressure and temperature conditions, by *Kumazawa* [1969], *Weidner et al*. [1978], *Webb and Jackson* [1993] (room temperature to 3 GPa), *Chai et al*. [1997a] (room temperature to 12.5 GPa), *Jackson et al*. [1999, 2007] (room pressure to 1073 K), and most recently by *Zhang and Bass* [2016a] (room temperature to 12 GPa). The bronzite ($Mg_{0.8}Fe_{0.2}SiO_3$) elastic constants were measured using the transit time of ultrasonic waves (20 MHz) by *Frisillo and Barsch* [1972]

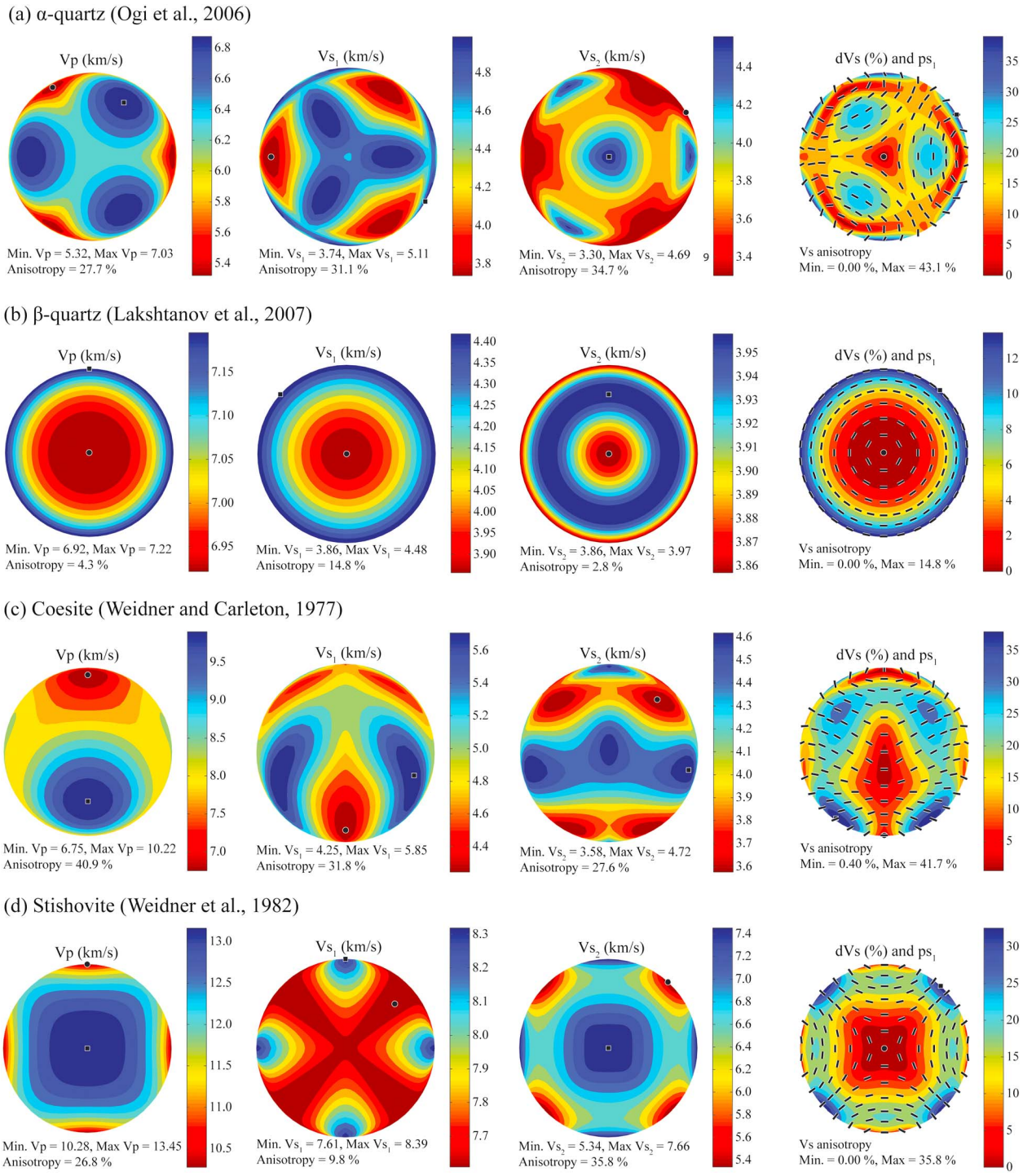

Figure 9. SiO_2 polymorph single-crystal seismic properties (V_p, V_{s1}, V_{s2}, and AV_s) presented in equal-area projections for (a) α-quartz, (b) β-quartz, (c) coesite, and (d) stishovite. Note that the different polymorphs are stable at different pressure and temperature conditions (Figure 8). Abbreviations are *P* wave velocity (V_p), fast polarized shear wave velocity (V_{s1}), polarized slow shear wave velocity (V_{s2}), shear wave anisotropy (dV_s), and polarization direction of V_{s1} (ps_1).

in the pressure range of room pressure to 1 GPa. The longitudinal elastic constants (c_{11}, c_{22}, and c_{33}) were found to increase linearly with pressure, whereas the shear constants (c_{44}, c_{55}, and c_{66}) exhibited a nonlinear increase as a function of pressure. *Zhang and Bass* [2016a] measured elastic constants up 12 GPa, for a Fe-bearing orthoenstatite. They found a pronounced increase in anisotropy in the single crystal at 12.06 GPa arising from a phase transition to high-pressure clinoenstatite (HPCEN2). Most of

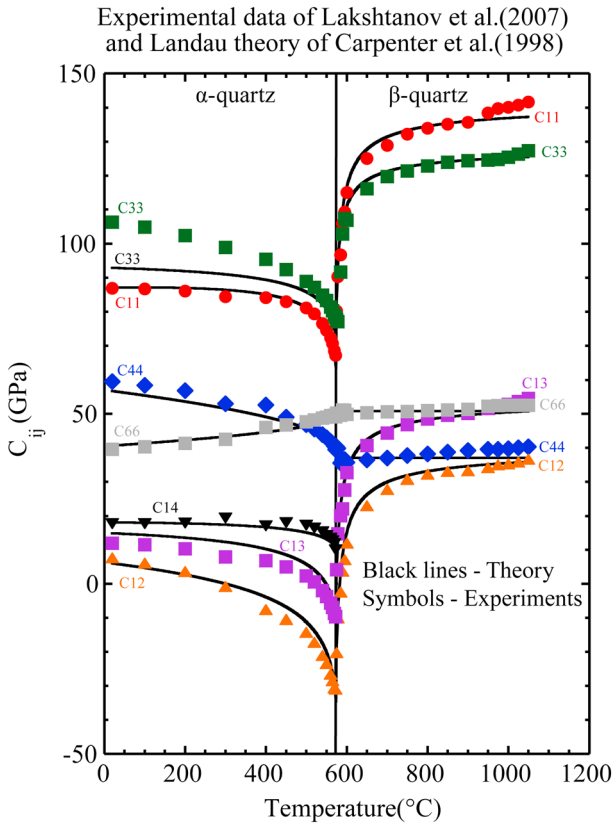

Figure 10. Phase stability diagram for α-quartz and β-quartz at room pressure. The elastic stiffness constants modeled by Landau theory [*Carpenter et al.*, 1998] are indicated by black lines. More recent experimental data of *Lakshtanov et al.* [2007] are shown by color symbols. Note that c_{14} is only present in the trigonal symmetry α-quartz field. The theory and experiment are generally in good agreement, with the exception of c_{33} in α-quartz.

these studies have focused on elastic constants at room temperature or the pressure effect on the elastic constants. Comparatively, fewer studies have investigated the temperature dependence of orthopyroxenes. There are two exceptions, the study of *Frisillo and Barsh* [1972], who found a linear dependency on temperature of the elastic constants, from a small range in temperature of 20°C up to 350°C and more recently by *Jackson et al.* [2007] from 24°C to 800°C.

The elastic stiffness tensor has been measured for orthopyroxene in at least seven publications, with composition of pure or close to pure enstatite. All the studies of the orthoenstatite at room conditions agree very closely, with increasing Fe content leading to decreasing stiffness and Al content increasing stiffness. The most recent publications probably give the most reliable data. *Jackson et al.* [2007] provide temperature derivatives in the form of polynomial fits for orthoenstatite from Zabargad, Egypt. *Zhang and Bass* [2016a] used orthoenstatite from a peridotite xenolith from San Carlos, Arizona. The crystal stays in the orthoenstatite (space group Pbca) stability field up to 11 GPa; above this pressure the crystal transforms to a high-pressure monoclinic form called HPCEN2 (space group P21/c, distinct from the low-pressure LPCEN with the same space group). All the elastic constants are given in the form of a table in the supporting material by *Zhang and Bass* [2016a].

The clinopyroxene minerals considered in this review are diopside ($MgCaSi_2O_6$), hedenbergite [$FeCaSi_2O_6$], omphacite [(Ca, Na)(Mg, Fe^{2+}, Al)Si_2O_6], jadeite [$NaAlSi_2O_6$], aegirine [$NaFeSi_2O_6$], augite [(Ca,Na)(Mg,Fe,Al, Ti)$(Si,Al)_2O_6$], and ureyite [$NaCrSi_2O_6$]; when describing chemical composition, these end-members are abbreviated by Di, Hd, Om, Jd, Aeg, Aug, and Ur, respectively. Generally, the chemical composition of clinopyroxenes in different studies has an intermediate composition between these end-members; diopside and hedenbergite form a solid series. Early measurements for different clinopyroxenes (diopside, augite, aegerine, and aegirine-augite) were made by *Aleksandrov et al.* [1964], using the ultrasonic pulse transmission technique at ambient conditions. *Isaak et al.* [2006] presented the first measurements of elastic constants as a function of temperature for chrome-diopside, for a crystal with composition $Di_{0.93}Hd_{0.03}Ur_{0.02}X_{0.02}$, where X represents minor element components. *Kandelin and Weidner* [1988b] measured elastic constants of hedenbergite and jadeite at room conditions (1 bar, 20° C). *Bhagat et al.* [1992] measured the elastic constants for omphacite at ambient conditions.

The elastic stiffness tensors of seven different compositions of clinopyroxene have been measured at room conditions. However, only for diopside have the pressure derivatives been measured, up to 14 GPa by *Zhang and Bass* [2016a] and the temperature derivatives to 1300 K by *Isaak et al.* [2006]. The pressure dependence of elastic constants of diopside was investigated in a Brillouin scattering study by *Sang and Bass* [2014], using a diamond anvil setup up to 14 GPa. *Walker* [2012] used ab initio methods to calculate the elastic

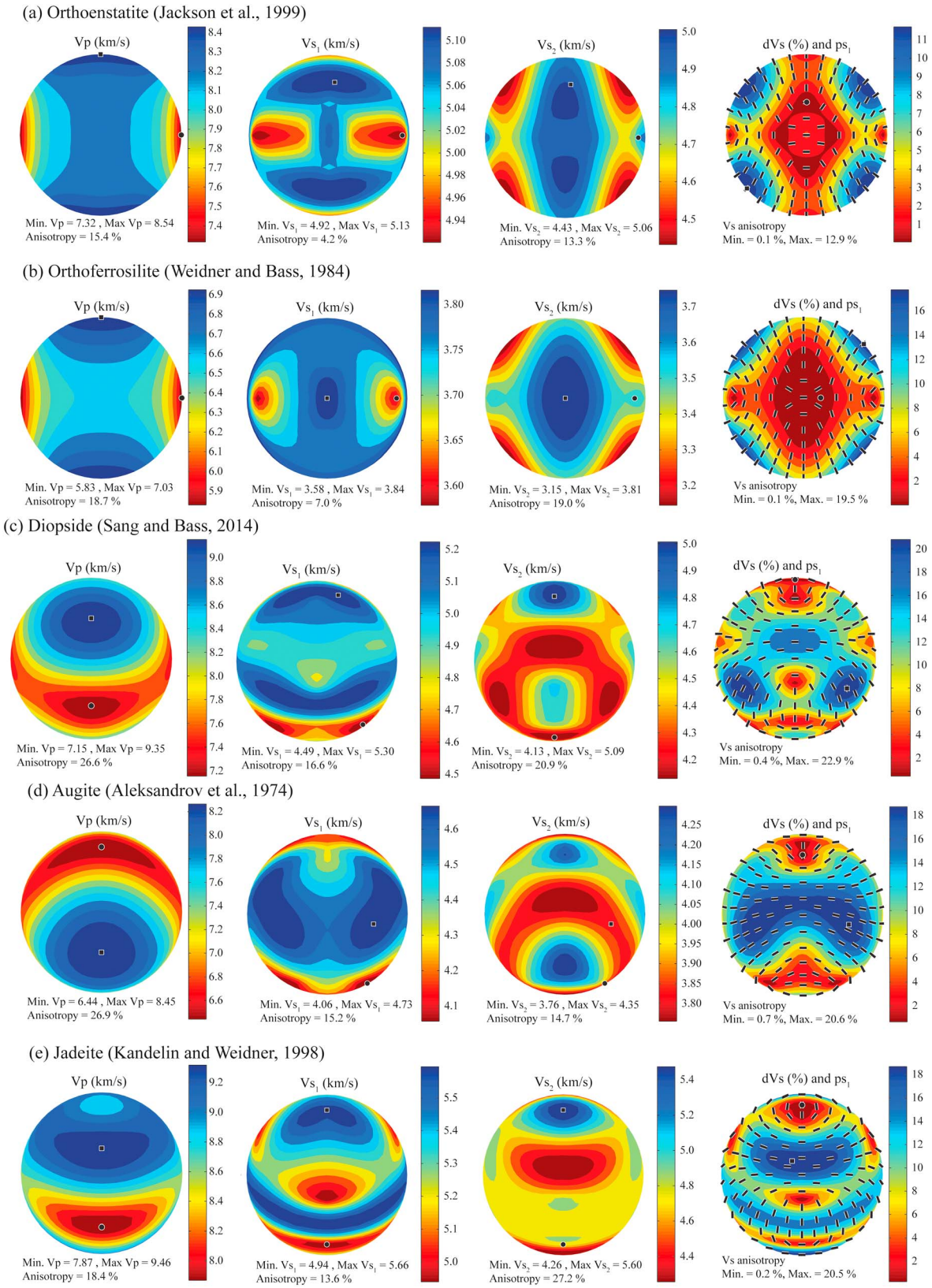

Figure 11. Pyroxene single-crystal seismic properties (V_P, V_{S1}, V_{S2}, and AV_S) presented in equal-area projections at ambient conditions for (a) orthoenstatite, (b) ferrosilite, (c) diopside, (d) augite, and (e) jadeite. Abbreviations are *P* wave velocity (V_P), fast polarized shear wave velocity (V_{S1}), polarized slow shear wave velocity (V_{S2}), shear wave anisotropy (dV_S), and polarization direction of V_{S1} (ps_1).

constants as a function of pressure to 20 GPa, for jadeite and diopside. However, *Sang and Bass* [2014] make the comment that ab initio values are not always in agreement with the experimental measurements. Most of diagonal moduli are in reasonable agreement. The off-diagonal terms that Walker report are systematically larger than measured values for C_{11}, C_{12}, C_{13}, C_{23}, C_{25}, and C_{35}, with difference up to 24%, but lower values for C_{44}, C_{15}, and C_{46}. It would be reasonable to use the experimental values when there is choice between experiments and ab initio calculations as the off-diagonal stiffness constants tend to be less well determined by theoretical estimates.

3.5. Sheet Silicates: Mica and Clay Minerals

Sheet silicates (mica) and clay minerals are the most anisotropic phases in regards to their elastic constants and single-crystal seismic properties (Figure 12). Most sheet silicate minerals have monoclinic symmetry and therefore characterized by 13 independent elastic constants. *Aleksandrov and Ryzhova* [1961] reported the currently only available elastic constants for biotite, using ultrasonic wave velocities. However, the elastic symmetry of monoclinic biotite was simplified to pseudohexagonal with a symmetry axis parallel to the crystallographic *c* axis and plane of isotropy containing the crystallographic *a* and *b* axes. *Vaughan and Guggenheim* [1986] used Brillouin scattering to measure the complete set of elastic constants for monoclinic muscovite. Extreme single-crystal anisotropy, coupled with generally strong CPOs in rocks, makes biotite and muscovite important candidates as a primary source for seismic anisotropy in the crust [e.g., *Lloyd et al*., 2009]. The extreme anisotropy of biotite moduli c_{44} and c_{66} is noteworthy, because of the more than 10 times higher elastic modulus in the latter constant. Biotite can thus generate a maximum AV_s >100% (Figure 12). Clay minerals are also important when considering seismic anisotropy in shale and mudstone [*Valcke et al*., 2006]. Elastic constants for illite, kaolinite, and chlorite were reported by *Katahara* [1996], although the values in the matrix were simplified to pseudohexagonal crystal symmetry. Recently, the complete set of elastic constants for several sheet silicate minerals, including muscovite, kaolinite, illite-smectite, dickite, and nacrite, was determined using first-principle calculations by *Militzer et al*. [2011]. The first-principle calculations provide a valuable addition to the elastic constants of the sheet silicate family of minerals, especially because of the challenge to measure elastic constants of clay minerals in the laboratory. *Aleksandrov and Ryzhova* [1961] and *Aleksandrov et al.* [1974] reported the first elastic constants for phlogopite, acquiring five independent elastic constants by ultrasonic wave speeds in laboratory experiments; these experiments considered phlogopite with pseudohexagonal symmetry. *Chheda et al*. [2014] performed first-principle calculations to obtain the complete 13 independent elastic constants of monoclinic phlogopite, thereby providing a better constraint on its elastic properties (Table 2). The different studies reported elastic constants for phlogopite that generally agreed well in terms of magnitude.

3.6. Amphiboles

Amphiboles are among the most poorly described mineral systems in terms of their range of elastic constants as a function of chemical composition. They are, however, abundant in middle and lower crustal settings. Along with mica, amphiboles are thought to represent the main mineral-related sources for anisotropy in crustal rocks [e.g., *Barberini et al*., 2007; *Tatham et al*., 2008; *Erdman et al.*, 2013; *Ji et al*., 2013, 2015; *Wenning et al*., 2016] (Figure 13). Amphibole-rich rocks tend to develop strong CPO and SPO in deformed rocks and therefore have significant potential to generate strong seismic anisotropy [*Tatham et al*., 2008]. However, few data on elastic constants exist for amphibole, and until recently, only the data of two hornblende crystals with unknown composition, published by *Aleksandrov and Ryzhova* [1961] (subsequently updated by *Aleksandrov et al.* [1974]), have been used in calculation of seismic properties. *Brown and Abramson* [2016] provide new data obtained from nine amphibole crystals with different Ca-Na composition. Their results indicate significantly higher elastic constants (and seismic velocities) for single-crystal amphibole than those of earlier works, as well as higher anisotropy (Table 2). The uncertainties in their measurements are generally ≤1% of the total elastic stiffness constant. They furthermore point out that all previous calculated seismic velocities, using the older set of amphibole elastic constants, need to be considered with caution and may even have to be reconsidered in light of the up-to-date elastic constants. In addition, *Bezacier et al*. [2010] conducted Brillouin scattering measurements to determine the elastic constants of glaucophane at ambient conditions (Table 2). Glaucophane has high *P* and *S* wave single-crystal anisotropy (AV_p = 38.1% and maximum AV_s = 27.3%) and tends to develop strong CPO when deformed, particularly in blueschist grade metamorphic rocks (Figure 13e).

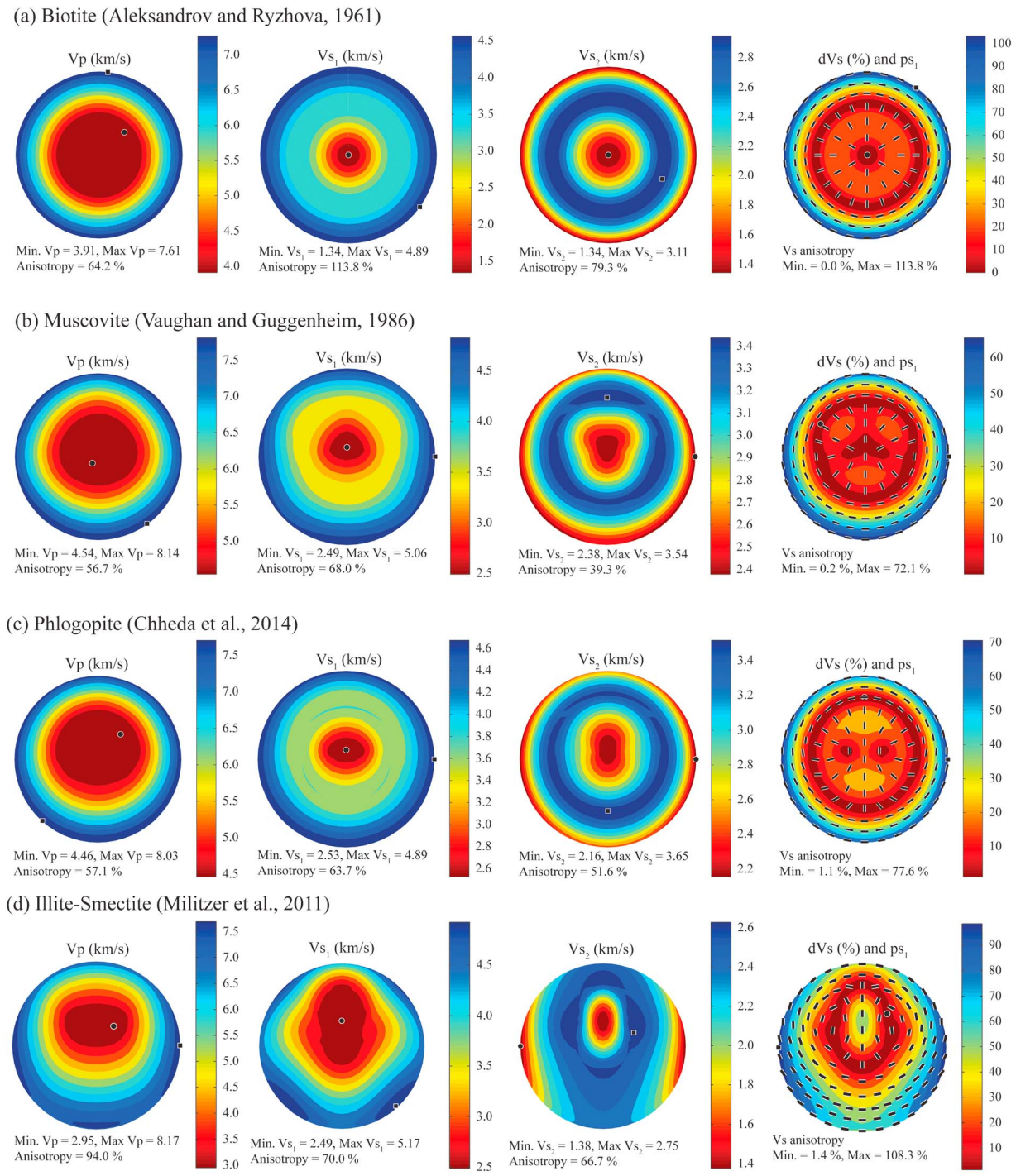

Figure 12. Sheet silicate single-crystal seismic properties (V_p, V_{s1}, V_{s2}, and AV_s) presented in equal-area projections at ambient conditions for (a) biotite, (b) muscovite, and (c) phlogopite. Abbreviations are *P* wave velocity (V_p), fast polarized shear wave velocity (V_{s1}), polarized slow shear wave velocity (V_{s2}), shear wave anisotropy (dV_s), and polarization direction of V_{s1} (ps_1).

3.7. Olivine

Olivine is the most studied mineral in terms of its elastic constants [*Verma*, 1960; *Kumazawa and Anderson*, 1969; *Brown et al.*, 1989; *Isaak et al.*, 1989, 1993; *Isaak*, 1992; *Abramson et al.*, 1997; *Speziale et al.*, 2004; *Mao et al.*, 2015; *Zhang and Bass*, 2016b]. This is no surprise given that olivine is the most voluminous phase in the upper mantle, and it has a rich history in being used to reconstruct flow patterns in the mantle

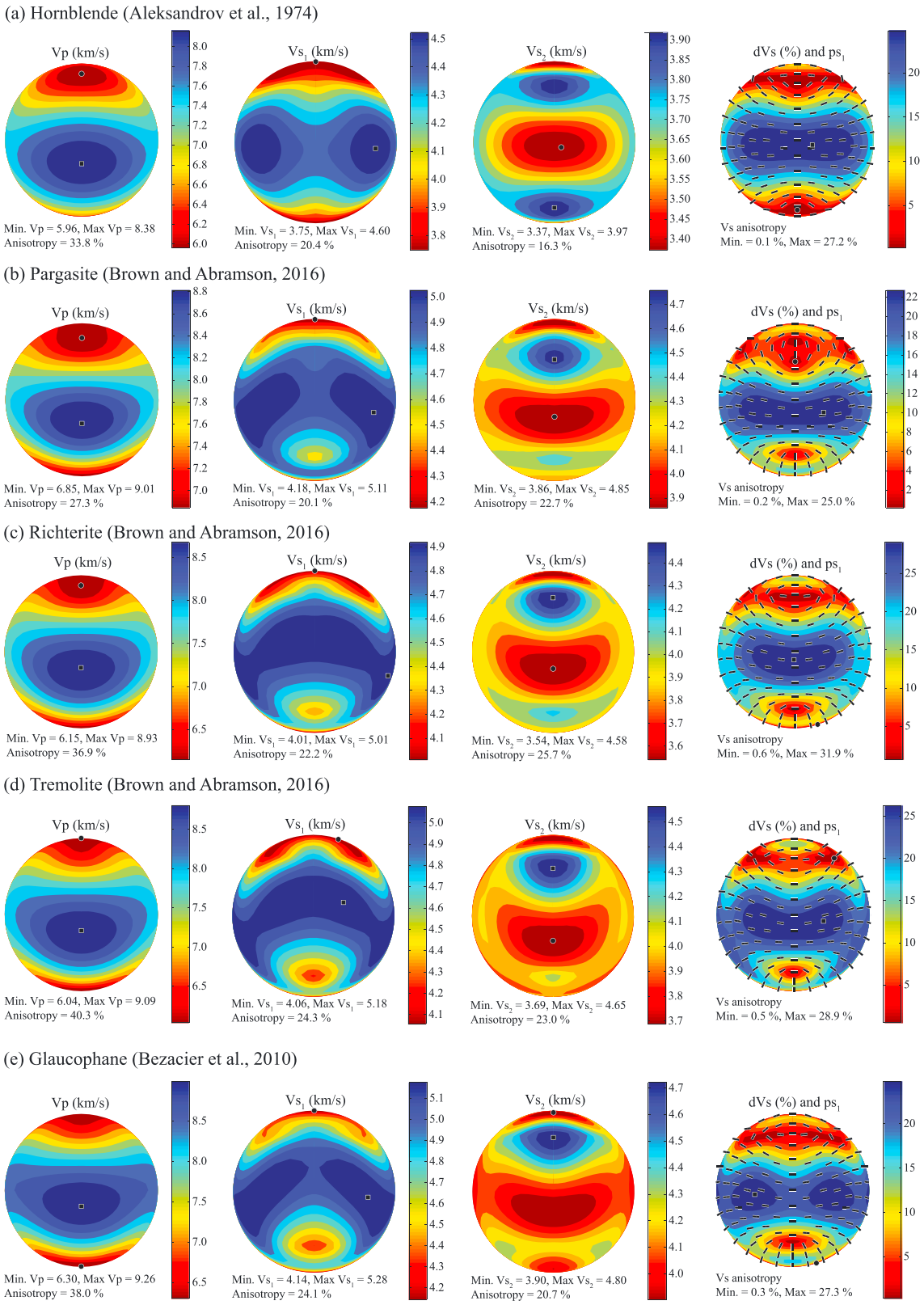

Figure 13. Amphibole single-crystal seismic properties (V_P, V_{S1}, V_{S2}, and AV_S) presented in equal-area projections at ambient conditions for (a) hornblende, (b) pargasite, (c) richterite, (d) tremolite, and (e) glaucophane. Abbreviations are *P* wave velocity (V_P), fast polarized shear wave velocity (V_{S1}), polarized slow shear wave velocity (V_{S2}), shear wave anisotropy (dV_S), and polarization direction of V_{S1} (ps_1).

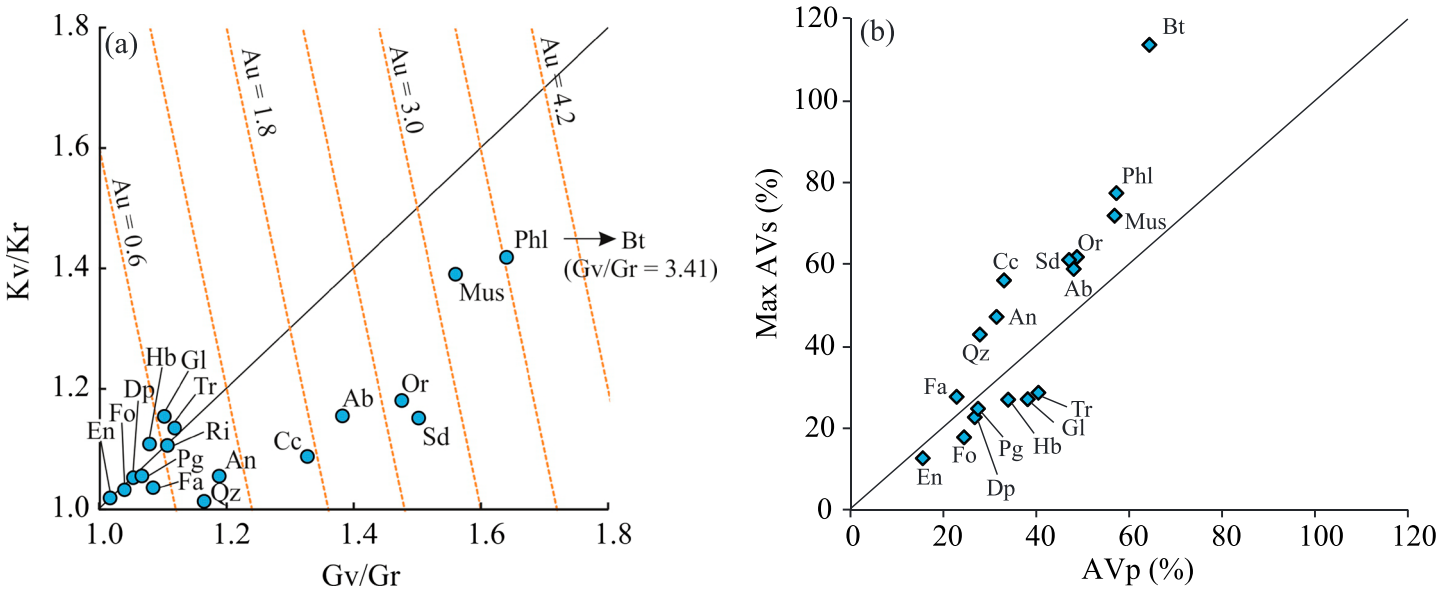

Figure 14. Elastic and seismic anisotropy of minerals. (a) The universal elastic anisotropy index (Au) for common rock-forming minerals in the continental crust, using the definition of *Ranganathan and Ostoja-Starzewski* [2008]. Axes show the ratio of the Voigt and Reuss bounds of bulk and shear moduli (K_v/K_r, G_v/G_r) calculated from the elastic stiffness constants. (b) Plot of AV_p and maximum AV_s for the same set of minerals as in Figure 14a. The Voigt-Reuss-Hill (VRH) was used to calculate the anisotropy. Mineral abbreviations are albite (Ab), Anorthite (An), biotite (Bt), calcite (Cc), diopside (Dp), enstatite (En), fayalite (Fa), forsterite (Fo), hornblende (Hb), glaucophane (Gl), muscovite (Mus), orthoclase (Or), quartz (Qz), pargasite (Pg), phlogopite (Phl), richterite (Ri), sanidine (Sd), and tremolite (Tr).

[*Hess*, 1964; *Silver*, 1996; *Savage*, 1999; *Faccenda and Capitanio*, 2012; *Long*, 2013; *Skemer and Hansen*, 2016; *Hansen et al*., 2016]. Its presence in the continental crust is, however, much lower (Figure 2), and therefore, it likely plays only a secondary role in seismic properties and anisotropy in continental crust. The exception for this is in settings where olivine-rich rocks may be incorporated into the continental crust, such as in ophiolite and (ultra)mafic intrusions, including gabbro. Different compositions of olivine spanning from the Fe end-member fayalite to the Mg end-member have been investigated, and elastic constant measurements have been made over a considerable pressure and temperature range (Table 1). More recent studies, by *Mao et al*. [2015] and *Zhang and Bass* [2016b], have investigated the effects of pressure and temperature on elastic constants of olivine. *Mao et al*. [2015] used San Carlos olivine [(Mg0.9Fe.0.1SiO4)] for experiments to 20 GPa and 900 K and found that temperature dependence of the elastic constants changed significantly as a function of pressure, whereas *Zhang and Bass* [2016b] conducted Brillouin scattering experiments on a set of three San Carlos olivine crystals set up in diamond anvil cells, at conditions that ranged up to 12.8 GPa and 1300 K. At high confining pressure (<10 GPa), the elastic constants c_{11}, c_{12}, and c_{13} displayed stronger temperature dependence relative to low confining pressures. Elastic shear (c_{44}, c_{55}, and c_{66}) moduli showed a strong concave dependency at higher confining pressures and decreased more rapidly than other elastic constants as a function of pressure.

3.8. Elastic and Seismic Anisotropy of Single-Crystal Minerals

Anisotropy of the single-crystal elastic constants is an important factor when considering seismic anisotropy in rocks. The universal elastic anisotropy index (Au) of *Ranganathan and Ostoja-Starzewski* [2008] is used to express the ratio of upper Voigt and lower Reuss estimates for the bulk (K_v, K_r) and shear (G_v, G_s) moduli. The difference between the Voigt and Reuss bounds arises from all the c_{ij} constants in the stiffness tensor, and therefore, the Au provides indication for the degree (or magnitude) of anisotropy of the single crystal. The magnitude of the G_v/G_r ratio reflects the V_s anisotropy, whereas K_v/K_r together with the G_v/G_r ratio provides an indication for V_p anisotropy. Figure 14a shows Au for the common rock-forming crustal minerals in the continental crust. All minerals have higher G_v/G_r and therefore fall below the line of unity. Mafic minerals such as olivine and pyroxene generally have values of Au < 0.6, whereas amphiboles, in general, plot around Au ~0.6 (with the exception of pargasite, which has lower Au). Feldspars show a range of anisotropy, from Au ~1.0 to Au > 2.4. Phyllosilicates are the most anisotropic minerals, with Au > 3.0; biotite stands out significantly because of its extreme G_v/G_r, which is at least twice that of any other mineral. Figure 14b

shows AV_p and maximum AV_s plotted against each other, for the same set of minerals as in Figure 14a (the Voigt-Reuss-Hill average was used in the calculation of the anisotropy). Expressions of seismic anisotropy for the different minerals follow closely the trends seen for minerals in Figure 14a, with AV_p, in general, matching the K_v/K_r ratio and maximum AV_s matching the G_v/G_r ratio.

3.9. Effects of Pressure and Temperature on Single-Crystal Elastic Constants

Uncertainty in calculated seismic properties arises in part because of the lacking data for single-crystal elastic constants at elevated pressure and temperature. However, some data do exist for single-crystal elastic constants as a function of pressure and temperature. For many minerals the pressure and temperature data are currently missing (Table 1). These data are of fundamental importance, because of phase changes at different pressure and temperature conditions for many minerals, which leads to changes in the elastic properties. Measurements of elastic constants at high pressure are often made utilizing diamond anvil cells, with a possibility to illuminate the single crystal using Brillouin scattering measurements. Higher temperatures can be made with laser heating, providing heating to well above 1000 K.

Methods to circumvent lacking pressure and temperature data exists. Considering the isotropic case, one approach to the problem is to extrapolate elastic properties from standard temperature and pressure (STP) at ambient conditions (298 K and one atmosphere pressure) to the target elevated temperature and pressure conditions at depth in the Earth [*Bina and Helffrich*, 1992; *Hacker and Abers*, 2004; *Abers and Hacker*, 2016]. In this approach the temperature and pressure dependence of bulk and shear moduli, as well as density, is calculated based on thermodynamic relationships. Although this approach has been developed and successfully used in the isotropic case, it is uncertain how this relationship applies to the complete set of constants in the elastic stiffness tensor. Further experimental measurements and ab initio modeling are therefore needed at elevated pressure and temperature conditions, and future studies should aim to develop thermodynamic modeling to incorporate the complete elastic stiffness tensor. Thermodynamic relationships, using major element chemistry data, are another way of predicting isotropic seismic properties at in situ conditions, such as the Perple_X thermodynamic software [e.g., *Connolly and Petrini*, 2002; *Connolly and Khan*, 2016].

To calculate the elastic constants at elevated pressures and temperatures, the single-crystal elastic constants are given at the pressure and temperature of their measurement using the following relationship:

$$C_{ij}(P,T) = C_{ij}(P_oT_o) + \left(\frac{\mathrm{d}C_{ij}}{\mathrm{d}P}\right) \cdot \Delta P + \frac{1}{2}\left(\frac{\mathrm{d}^2C_{ij}}{\mathrm{d}P^2}\right) \cdot \Delta P^2 + \left(\frac{\mathrm{d}C_{ij}}{\mathrm{d}T}\right) \cdot \Delta T + \left(\frac{\mathrm{d}^2C_{ij}}{\mathrm{d}P\mathrm{d}T}\right) \cdot \Delta P \cdot \Delta T \qquad (15)$$

where $C_{ij}(P, T)$ are the elastic constants at pressure P and temperature T, $C_{ij}(P_oT_o)$ the elastic constants at a reference pressure P_o (e.g., 0.1 MPa) and temperature T_o (e.g., 25°C), $\mathrm{d}C_{ij}/\mathrm{d}P$ is the first-order pressure derivative, $\mathrm{d}C_{ij}/\mathrm{d}T$ is the first-order temperature derivative, $\Delta P = P - P_o$, and $\Delta T = T - T_o$. The Taylor expansion series is developed about the elastic constants at the reference condition $C_{ij}(P_oT_o)$. The series only represents the variation of the C_{ij} in their intervals of pressure and temperature of convergence, in other words the pressure and temperature range of the experiments or atomic modeling calculations used to determine the derivatives. The second-order pressure derivatives $\mathrm{d}^2C_{ij}/\mathrm{d}P^2$ are available for an increasing number of minerals (e.g., olivine, orthopyroxene, and garnet). First-order temperature derivatives seem to adequately describe the temperature dependence of most minerals, although second-order derivatives are also available in a few cases (e.g., garnet, fayalite, forsterite, and rutile) (see *Isaak* [2001] for references). Experimental measurements of the cross pressure-temperature derivatives $\mathrm{d}^2C_{ij}/\mathrm{d}P\mathrm{d}T$ (that is the temperature derivative of the $C_{ij}/\mathrm{d}P$ at constant temperature) are still very rare. Note that when a phase transitions occurs, then the specific changes in elastic constants at pressures near the phase transition will have to be taken into account, for example, the SiO_2 polymorphs [*Karki et al*., 1997; *Cordier et al*., 2004; *Carpenter*, 2006]. The seismic velocities also depend on the density of the minerals at pressure and temperature, which can be calculated using an appropriate equation of state [*Knittle*, 1995]. The Murnaghan equation of state derived from finite strain is sufficiently accurate at moderate compressions [*Knittle*, 1995] of the upper mantle and crust and leads to the following expression for density as a function of pressure:

$$\rho(P) = \rho_o\left(1 + \left(\frac{K'}{K}\right) \cdot (P - P_o)\right)^{1/K'} \qquad (16)$$

where K is bulk modulus, $K' = dK/dP$ is the pressure derivative of K, and ρ_o is the density at reference pressure P_o and temperature T_o. For temperature the density varies as

$$\rho(T) = \rho_o\left[1 - \int \alpha_V(T)dT\right] \approx \rho_o 1 - \alpha_{\mathrm{av}}(T - T_o)] \tag{17}$$

where $\alpha_v(T) = 1/V(\partial V/\partial T)$ is the volume thermal expansion coefficient as a function of temperature and α_{av} is an average value of thermal expansion which is constant over the temperature range [*Fei*, 1995]. For temperatures and pressures of the mantle, the density is described by *Mainprice* [2015],

$$\rho(P,T) = \rho_o\left\{(1 + \left(\frac{K'}{K}\right).(P - P_o)\right)^{\frac{1}{K'}}[1 - \alpha_{\mathrm{av}}(T - T_o)]\} \tag{18}$$

The same expression is applicable to crustal conditions, considering pressure and temperature effects on single-crystal elasticity of crustal minerals. We have used equations (15) and (18) to calculate the pressure and temperature dependence of seismic velocities, as well as AV_p and AV_s, for diopside (Figure 15). Both the pressure and temperature derivatives of C_{ij} have been experimentally determined, by *Sang and Bass* [2014], and *Isaak et al.* [2006], respectively; derivatives exists for pressures up to 14 GPa and temperature up to 1300 K. Figure 15 shows that there is a subtle but important influence of diopside elastic constants as function of both pressure and temperature. Temperatures of 25°C (298 K), 700°C (973 K), and 1050°C (1323 K) were used in the example, representing ambient temperature conditions, and the rough temperature expected at 35 km depth (deep crust), with normal and high geothermal gradients (20°C/km and 30°C/km, respectively). At a fixed pressure of 1 GPa and increasing temperature from 25°C to 1050°C, the overall V_p decreases ~2.5%, whereas the overall decrease in V_{s1} and V_{s2} is ~4 to 5% (Figures 15a–15c). Figure 15d shows that AV_p generally decreases as a function of increasing pressure, whereas increasing temperature generally increases AV_p. Increasing pressure from 0.1 GPa to 3 GPa results in ~5% drop in the single-crystal diopside AV_p, whereas increasing the temperature from 25°C to 1050°C has a much smaller influence on AV_p (~1% increase). In contrast to AV_p, the maximum AV_s show little dependence on pressure in the 0.1 GPa to 3 GPa pressure range. Temperature is, however, considerably more important, increasing single-crystal maximum AV_s nearly 3% from 25°C to 1050°C. The diopside example shown in Figure 15 illustrates the importance of pressure and temperature on inferred seismic velocities. It also illustrates that changes in the elastic constants may not be applicable in a purely isotropic fashion but can affect the C_{ij} to different extent, meaning that pressure and temperature derivatives of C_{ij} are anisotropic.

4. Microfabric: Crystallographic Preferred Orientation (CPO) and Microstructure

4.1. Microfabric Definition

Microfabric is defined as "fabrics on microscopic scale" and includes elements of grain shape, grain boundaries, deformation lamellae, and crystallographic preferred orientation [*Paaschier and Trouw*, 2005] (also see the glossary). Crystallographic preferred orientation (CPO) is the measure for how uniformly crystallographic axes for specific minerals are oriented. CPOs can develop in different ways but commonly occur through crystal-plastic deformation. Crystal-scale deformation mechanisms operate to produce CPO and include mechanisms of dislocation creep and diffusion creep. The CPO is an important aspect of seismic properties and can often be the primary factor in exerting a directional control on seismic velocities in rocks. Because of its importance in seismic velocity modeling, we have separated out the CPO term from the umbrella term microfabric and refer specifically to CPO in the text. The remaining aspects are referred to as the microstructure and thus describe grain shape, grain boundaries, and deformation lamellae. Whenever a specific aspect of the microstructure is to be considered, it is noted (i.e., the shape-preferred orientation of mineral grains).

The microfabric elements generally need to be coordinated with respect to the macroscopic structural rock fabric, as seen in outcrop. This is done by considering the mineral foliation plane and axis of lineation (typically mineral stretching lineation), where the X axis is parallel to the lineation, Z axis normal to the foliation plane, and the Y axis in the foliation plane but perpendicular to the lineation axis. In deformed and anisotropic rocks it is generally possible to determine the foliation and lineation, although in more "isotropic" rocks such as granite it may not be possible to identify a foliation plane or lineation. However, whenever

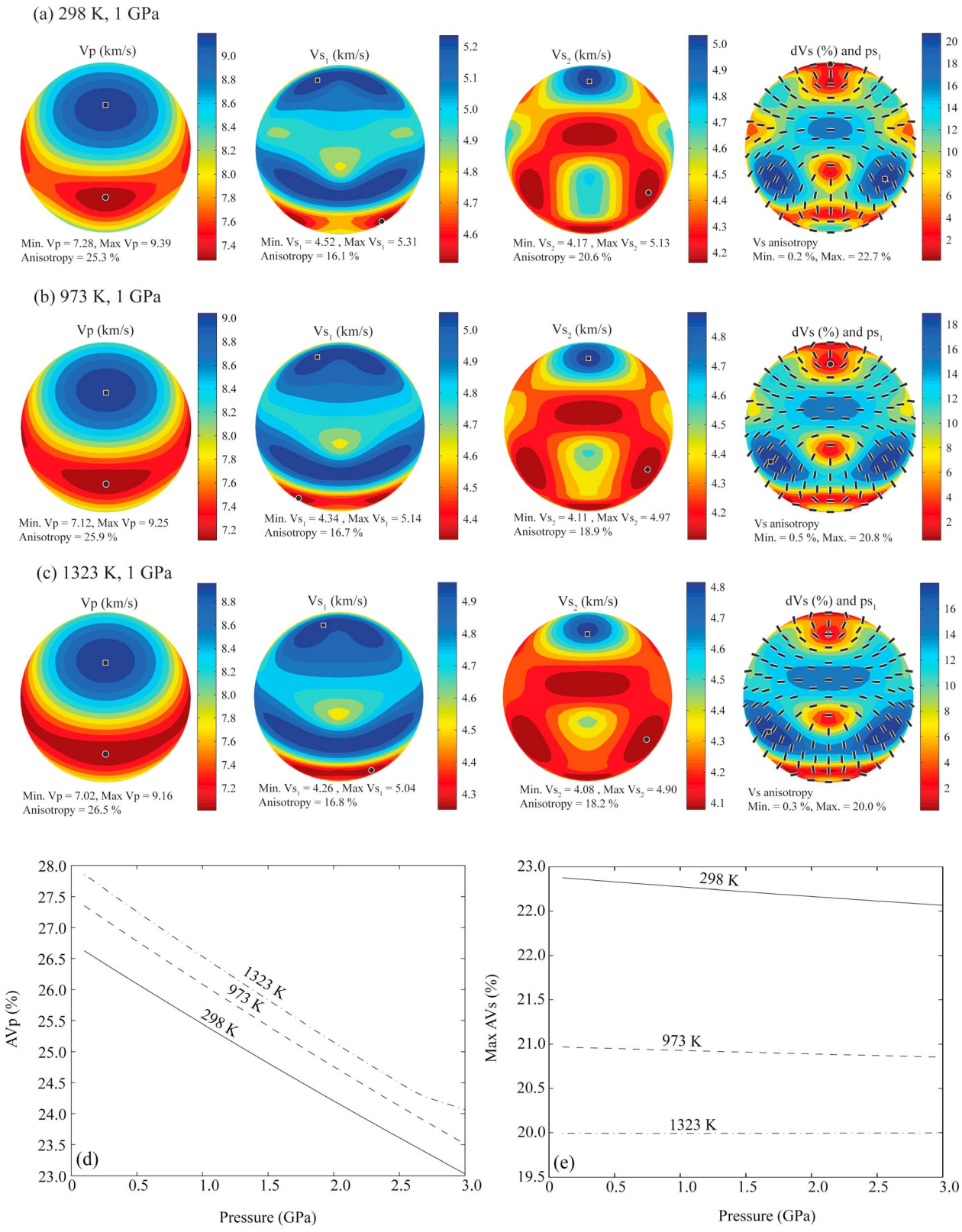

Figure 15. Pressure- and temperature-dependent seismic properties of single-crystal diopside. (a–c) Equal area stereographic projections showing V_p, V_{s1}, V_{s2}, AV_s, and polarization of the fast shear wave (ps_1), for temperatures of 298 K, 973 K, and 1323 K, at a fixed pressure of 1 GPa. (d) Anisotropy of the *P* wave (AV_p) shown as a function of pressure, for 298 K, 973 K, and 1323 K. (e) Maximum shear wave anisotropy (maximum AV_s) shown as a function of pressure, for 298 K, 973 K, and 1323 K.

possible, it is important to determine the macroscopic fabric since this forms the basis for relating the seismic anisotropy to the tectonic regime.

Advances in the understanding of how CPO contributes to the seismic properties of the crust arise in part from the possibility to measure crystallographic orientation of low-symmetry minerals, such as minerals with monoclinic and triclinic symmetry (e.g., feldspars and phyllosilicates), which has been challenging in the past. Different techniques exist to measure the CPO, and each technique has advantages and disadvantages, which will be discussed briefly as follows.

4.2. Texture and Microstructure Measurements

There are essentially four techniques available to measure the mineral texture. These are (1) universal stage (U-stage) measurements with a petrographic microscope, (2) X-ray diffraction (XRD) goniometry, (3) neutron diffraction goniometry, and (4) electron backscatter diffraction with a scanning electron microscope (SEM-EBSD). Each of these techniques is briefly described in this section.

Texture measurements with the U-stage have a long history of use in geology dating back to the late 1800s [*Fedorov*, 1892, 1894]. It uses the optical properties of minerals, whereby it is possible to provide orientation of several parameters, including crystal twin planes, cleavage, and principal optical directions (e.g., the *c* axis in quartz and calcite). The U-stage hence offers a powerful method to obtain crystallographic data, but it is somewhat limited because of the challenge to measure crystallographic orientations of lower symmetry minerals and the relatively time consuming measurements in comparison to diffraction techniques.

Standard XRD goniometry utilizes monochromatic X-rays, with a constant wavelength (λ). The technique can be used with slabs of polished rock samples in *reflection* mode or with thin sections where X-rays are diffracted by *transmission* through the sample. In its standard application the X-rays target a surface area of the sample covering ~1 mm^2, with a penetration depth of $\leq$100 μm. The depth of penetration is governed by the absorption of the X-rays, which in turn depends on atomic density of the material and the energy of the X-rays. Diffraction of X-rays is governed by Bragg's law, where the angle of the diffracted ray (θ) is a function of the lattice plane spacing (d) in the crystalline solid. Hence, in order to measure diffraction from a specific crystallographic plane (*hkl*), the detector has to be set at an angle θ. In practice, the X-ray detector is moved to a specific position, with angle 2θ, in order to map the crystallographic plane that is of interest. The goniometer stage allows mapping of the preferred orientation of crystallographic planes (*hkl*) for different positions of the samples, and plotting the resulting 3-D orientation data is made in pole figures. One pole figure is produced for each crystallographic plane that is investigated. The angle of incidence of X-rays with respect to the planar surface of the sample will yield incomplete pole figures because not all positions in the goniometer cradle can yield a measurable diffraction.

Neutron measurements function similarly to XRD, in the sense that the sample is measured while placed in a goniometer stage. However, neutrons interact weakly with matter, which enables deep penetration into materials in comparisons with X-rays (centimeter size samples). As a consequence neutrons provide the largest sample volume investigation of any method, which makes it ideally suited for comparison with laboratory measurements of seismic rock properties (made on rock plugs and cores). X-rays and neutrons are of particular value to measure CPO in fine-grained aggregates, such as mud rocks and shale, where clay particles are too small to map with other techniques.

Electron backscatter diffraction (EBSD) is the most recently developed method [e.g., *Prior et al*., 1999] that is discussed in this work, and many recent studies on prediction of seismic properties have used electron backscatter diffraction data as input for models. A key advantage of the EBSD method is the added information on the microstructural arrangement of minerals, which is generally unavailable to the goniometer methods. The main drawback is the small depth of penetration of electrons of less than 0.5 μm considered in the EBSD application, whereas sample areas of 2 cm^2 can be measured. The area of investigation is generally an order of more magnitudes smaller than for X-rays and neutrons. Electrons generated by the filament in a scanning electron microscope (SEM) penetrate shallowly into a crystalline solid and interact with the crystalline structure of minerals and diffract according to Bragg's condition. Because of the shallow penetration depth, the EBSD method requires ultrapolished sample surfaces, with very small surface roughness. Techniques such as ion milling can be combined with EBSD, in order to observe the microfabric at different depths in the sample and thus construct an effective 3-D image of the microstructure and CPO in a sample. Polished

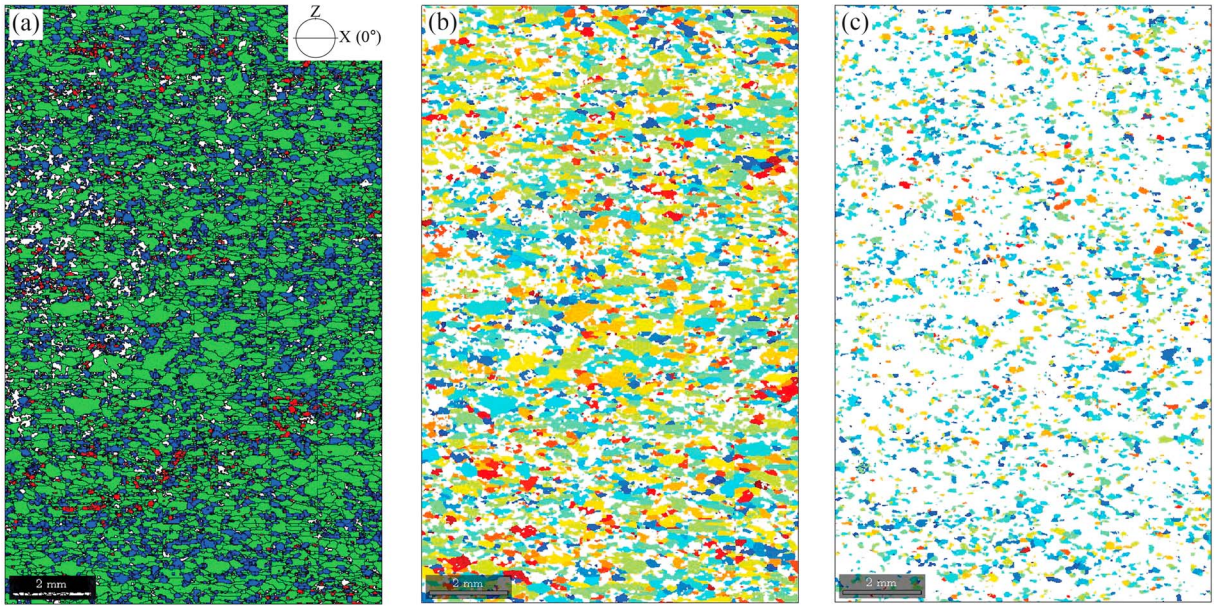

Figure 16. Microstructural EBSD maps from an amphibolite sample (COSC-193) that shows (a) the minerals and grain boundaries, (b) crystallographic orientation data from hornblende, and (c) crystallographic orientation data from anorthite.

thin sections or rock slabs of 2 to 3 cm size are common samples used for EBSD analysis. Large EBSD mapping is becoming more common and easier, using stitching techniques and partially overlapping EBSD maps (millimeter to centimeter size maps).

Figure 16 shows the microstructural map and CPO for an amphibolite sample, COSC193 (IGSN: ICDP5054EX65601), collected from Jämtland in central Sweden. EBSD measurements coupled with chemical analysis using energy dispersive X-rays were made with a Zeiss EVI MA15 scanning electron microscope. Data collection and map stitching were performed with the Oxford Instruments Aztec software, and the data were further processed with the Channel 5 software (© Oxford Instruments); the area of analysis is ~9.5 × 15.2 mm. Plotting of the EBSD map is made with the MTEX open source MATLAB scripts. The modal composition of the sample is 67.0% amphibole (hornblende), 23.0% plagioclase (anorthite), and 2.3% quartz, as determined by the area occupied by the different phases in the EBSD map. Accessory minerals (<1%) consist of apatite, titanite, and pyrrhotite. As is seen in the microstructural map of Figures 16a and 16b, there is strong SPO of the amphibole. Figure 17 shows the CPO plotted in pole figures for amphibole, plagioclase, and quartz in the COSC193 sample. This EBSD map and CPO data will be further used in calculations of seismic velocity and anisotropy in the following sections, thus providing a comparison between different methods used to compute seismic properties.

5. Predictions of Seismic Velocities: Averaging Schemes and Dynamic Wave Propagation

In order to calculate seismic velocities from a sample of rock, it is necessary to take into account the aggregate of minerals it is composed by, in terms of both their amount and their orientation. This can be done in two ways, by (1) considering the CPO of different minerals in the rock, and their respective volumetric contribution (modal composition), and (2) considering the arrangement and microstructural details of minerals in the rock (in addition to the CPO and modal composition). The first approach is most generally applied through the use of the CPO of a mineral phase and evaluating its volume contribution in the composite aggregate. In this approach the aggregate is considered to be spatially disordered and does not take into consideration the effects of the distribution of grains and their shape. The second approach additionally considers aspects of the microfabric, such as SPO and the spatial distribution of minerals in the rock. In the broad sense this approach can be divided into categories of (1) theory of mixtures (effective medium modeling) that generally use the assumption of spatial disorder and (2) finite element (and finite difference) modeling using spatial position of all the microstructural elements, such as grains.

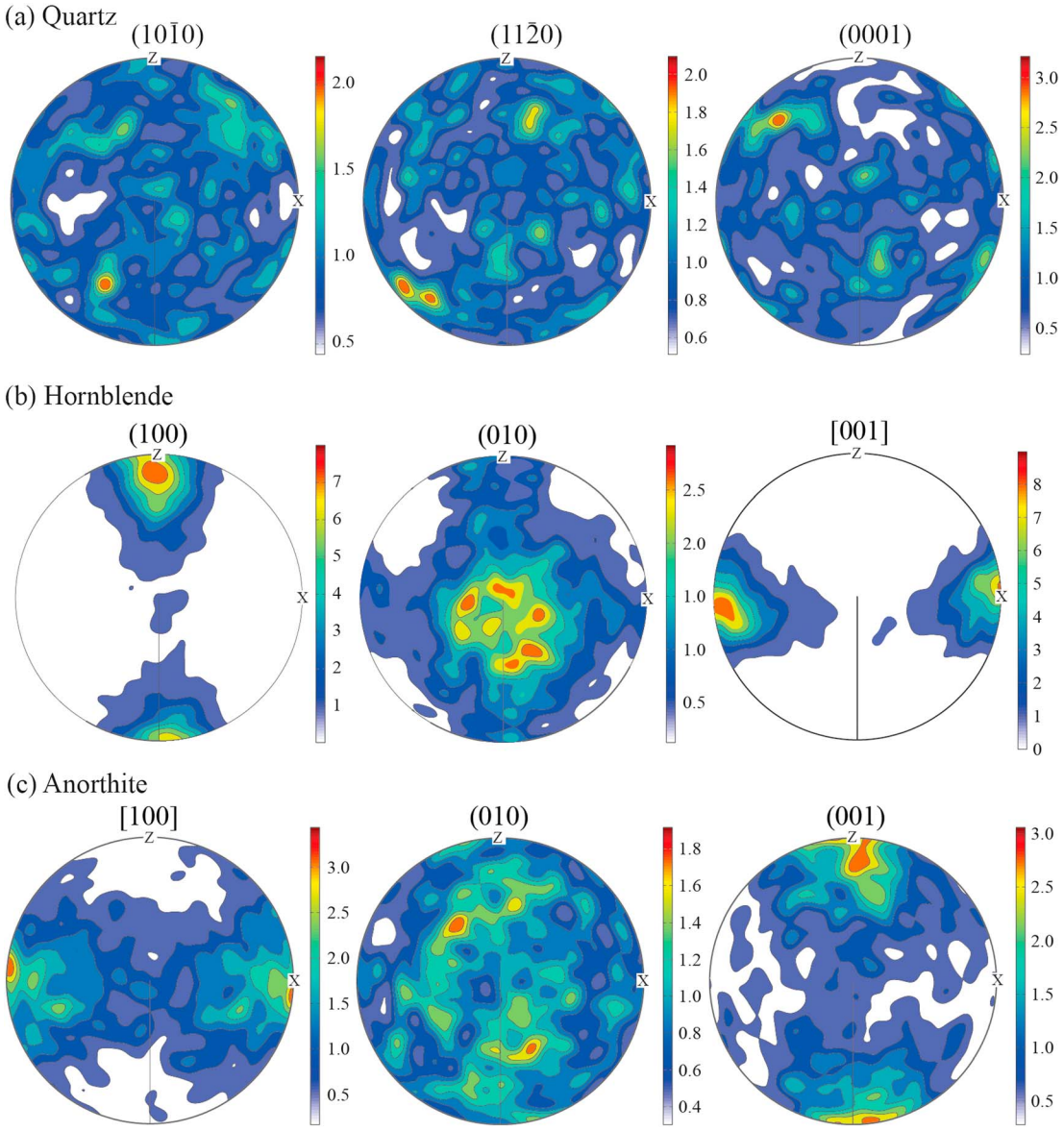

Figure 17. Pole figures for (a) quartz, (b) hornblende, and (c) anorthite, which make up the three main minerals in the microstructural map of the COSC193 sample (Figure 16). Contours indicate multiples of uniform distribution (MUD).

The most general constraints on elastic properties are Voigt and Reuss bounds (section 5.1). These bounds represent theoretical end-members, where either strain or stress is kept constant in the aggregate. However, in reality both stress and strain will vary throughout real material. The geometric mean (section 5.2) and Hill arithmetic average represent methods to average the theoretical end-members, where the former has a strong physical basis and the latter lacks such physical basis but usually performs well in prediction of elastic properties of an aggregate. Besides the CPO, none of these methods take into account other aspects of the microstructure, such the SPO and distribution of grains throughout the aggregate. Two methods that do take into account aspects of the microstructure are the self-consistent method and the asymptotic expansion homogenization method. The first of these is discussed in section 5.3, whereas the second method is discussed in section 5.4. Prediction of seismic velocity and anisotropy using dynamic, or active, wave propagation through a model aggregate is discussed in section 5.5, and effective medium properties of cracked and fractured rocks are covered in section 5.6. In the last part of this section (section 5.7), we briefly discuss the different software that are available to calculate seismic properties using the microfabric.

5.1. Voigt, Reuss, and Voigt-Reuss-Hill Averages

The most fundamental calculation of seismic properties takes into account the modal mineral composition and the respective elastic properties and density of the minerals that make up the rock. The widest theoretical bounds used for prediction of elastic properties of a mixture of phases, used to model seismic velocities, are the upper Voigt and lower Reuss bounds [*Voigt*, 1928; *Reuss*, 1929]. These bounds consider the relationship between stress and strain in a material. By definition, the Voigt bound is the upper elastic bound and known as the isostrain bound because the strain is considered constant in a material, whereas the stress is varying. The Voigt elastic constant for an aggregate is calculated as

$$C^V = \left[\sum_i V_i C(g_i)\right] \tag{19}$$

where V_i is the volume of a specified phase i and $C(g_i)$ is the elastic stiffness of phase i with orientation g_i.

In contrast, the Reuss bound is the theoretical lower bound or the isostress bound where strain can vary in the material. It is expressed as

$$C^R = \left[\sum_i V_i S(g_i)\right]^{-1} \tag{20}$$

where $S(g_i)$ is the elastic compliance of phase i and the remaining parameters are the same as in equation (19). When considering an anisotropic single crystal or polymineral aggregate consisting on one phase, then $C^V \neq C^R$ (the condition of $C^V = C^R$ is only fulfilled for an isotropic solid with two independent elastic constants). Subsequent to the introduction of theoretical Voigt and Reuss bounds, *Hill* [1952] suggested to use the arithmetic mean of the two end-member bounds. This has become known as the *Voigt-Reuss-Hill* (VRH) average. The VRH average does not have an explicit physical meaning but usually provides a good prediction of the elastic constants (or seismic velocities) of a rock based on the modal mineral composition.

Estimation of the modal composition is critical to any averaging technique. Usually, the modal mineral composition is determined from point counting of different phases or by determining the area (volume) occupied by different phases in a sample under investigation. The latter technique can most easily be made with EBSD. The amplitude of the diffraction peaks studied using X-ray and neutron diffraction goniometry may also provide some insight into the modal composition, but care needs to be taken in this respect, because the amplitude of a diffraction peak also depends on the CPO and crystal lattice plane that is measured.

For sample COSC-193 (introduced in Figure 16), the results of Voigt, Reuss, and VRH bounds are shown in Figure 18. The MTEX MATLAB suite of programs were used to predict V_p, AV_s, V_{s1}, and V_{s2}. Seismological convention in coloring is used, with red indicating seismic slow velocity that grades to blue, which indicates fast seismic velocity.

5.2. Geometric Mean

Morawiec [1989], *Matthies and Humbert* [1993, 1995], and *Mainprice and Humbert* [1994] developed the mathematical expression for the geometric mean. The physical basis of the geometric mean is that it fulfills the important reciprocal criteria $\langle C\rangle = \langle S\rangle^{-1}$ [*Aleksandrov and Aizenberg*, 1967], where $\langle C\rangle$ and $\langle S\rangle$ are the average stiffness and compliance tensors, respectively, for a polycrystalline aggregate. Computation of the geometric mean (C^G) is made with the expression

$$C^G = e^{\left[\frac{1}{|V|}\int_V \ln(C)\mathrm{d}V\right]} \tag{21}$$

where $|V|$ is the total volume of the sample or aggregate, for a number of elastic elements (C) integrated over the volume elements dV. Using the fact that a stable linear elastic solid must have positive elastic strain energy, *Matthies and Humbert* [1993] derived an expression for calculating the geometric mean for a distribution of grain orientations. Despite its theoretical advantage, the geometric mean is still not often implemented or provided in the broad literature of predicting elastic and seismic properties of rocks, and the VRH is more commonly used.

5.3. Self-Consistent Approximation and Layered Media

In order to take into account the effects of grain shapes and heterogeneities in the microstructure, other approaches are needed to model the elastic properties of an aggregate. These methods are more complex

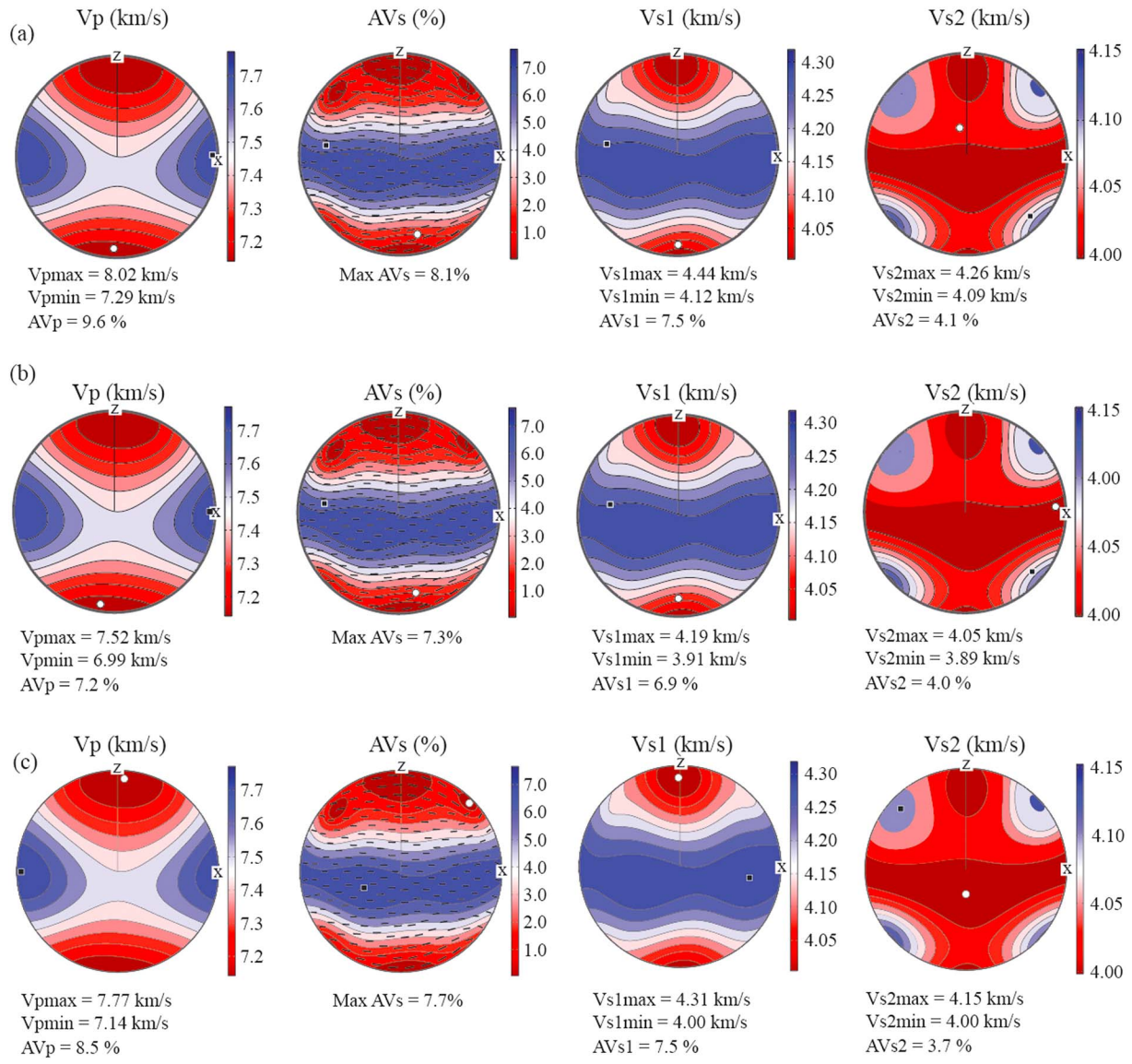

Figure 18. Example of calculation of (a) Voigt, (b) Reuss, and (c) Voigt-Reuss-Hill (VRH) averaging with MTEX [*Mainprice et al.*, 2014], for sample COSC193.

than the averaging schemes discussed previously, but generally provide a single solution for the elastic properties, based on the microstructural arrangement. There are several different effective medium models that have been developed to consider the influence of inclusions that are inserted in a background material (or matrix), and here we focus on one of the popular approaches, known as the self-consistent (SC) approximation and the layered media (which is commonly inferred from seismic imaging of the lower continental crust). Another useful effective medium model is the differential effective medium (DEM), which is described in detail by *Mainprice* [1997, 2015].

Eshelby [1957] originally presented a solution for incorporation of ellipsoidal elastic inclusions into an isotropic background medium, considering stress and strain to be uniform inside the inclusion. Based on the analytical solution derived by *Eshelby* [1957], it became possible to address the influence of the inclusion on elastic constants of the overall material. Introduction of ellipsoidal inclusions of idealized shapes and different elastic properties than a background medium could be made. The SC approximation for an isotropic material with inclusions of a specified shape (e.g., spheres and needles) was popularized by *O'Connell and Budiansky* [1974], based on earlier papers of *Budiansky* [1965] and

Hill [1965]. A SC two-phase composite that solves for the bulk (K) and shear (μ) moduli was introduced by *Wu* [1966],

$$K^*_{SC} = K_m + x_i(K_i - K_m)P^{*_i} \tag{22}$$

and

$$\mu^*_{SC} = \mu_m + x_i(\mu_i - \mu_m)Q^{*_i} \tag{23}$$

where x_i represents the volume of added inclusion and the subscripts m and i are the matrix and inclusion phases and P^{*i} and Q^{*i} are geometrical factors dictated by the shape of the inclusion (see *Mavko et al*. [2009] for details on the geometrical factors). *Berryman* [1995] provides a generalized solution for the SC approximation of a multiphase composite, which considers the arithmetic sum of N number of inclusion phases.

Kinoshita and Mura [1971] subsequently expanded Eshelby's solution to an anisotropic background medium. In case of evaluating the uniform strain inside an inclusion, in an anisotropic background it has been shown that [*Kinoshita and Mura*, 1971]

$$\epsilon_{ij} = \frac{1}{2}\left(G_{ijkl} + G_{jkil}\right)C_{klmn}\epsilon^*_{mn} \tag{24}$$

where ε_{ij} represents the strain inside the inclusion, G_{ijkl} is the tensor Green's function related to displacement due to a unit of force applied in a specified direction, C_{klmn} are the elastic stiffness constants of the anisotropic background medium, and ϵ^*_{mn} is the stress-free strain tensor resulting from removing the inclusion from the surrounding background. To evaluate Green's tensor, the solution of *Mura* [1987] can be used

$$G_{ijkl} = \frac{1}{4\pi}\int_0^{\pi}\sin\theta \mathrm{d}\theta\int_0^{2\pi}\left(K^{-1}_{ij}(x)x_k x_l\right)\mathrm{d}\phi \tag{25}$$

where θ and ϕ are spherical coordinate angles for the vector x in respect to the principal axes of the inclusion. The Christoffel stiffness tensor $K_{ip}(x) = C_{ijpl}x_j x_l$ for a given direction (x) is defined specifically as $x_1 = \sin\theta\cos/a_1$, $x_2 = \sin\theta\sin\phi/a_2$, and $x_3 = \cos\theta/a_3$, where a_1, a_2, and a_3 are the semiaxes of the ellipsoidal inclusion. The tensor Green's function is evaluated numerically because no analytical solution exists in the lowest triclinic symmetry case (for further details see *Mainprice* [1997, 2015]).

The SC approximation for an anisotropic medium uses *Willis* [1977] scheme, which evaluates the ratio of strain inside the inclusion to the strain in the background medium. This ratio, A_i,

$$A_i = \left[I + G\left(C_i - C^{SCA}\right)\right]^{-1} \tag{26}$$

and

$$\left\langle\varepsilon^{SCA}\right\rangle = \sum_{i=1}^{i=n} V_i A_i \left\langle\sigma^{SCA}\right\rangle = \sum_{i=1}^{i=n} V_i C_i A_i \tag{27}$$

$$C^{SCA} = \left\langle\sigma^{SCA}\right\rangle\left\langle\varepsilon^{SCA}\right\rangle^{-1} \tag{28}$$

where I is the symmetrical fourth-rank unit tensor, $I_{ijkl} = 1/2(\delta_{ik}\delta_{jl} + \delta_{il}\delta_{jk})$, and δ_{ik} is the Kronecker delta, V_i is the volume fraction of inclusion i, and C_i is the elastic stiffness constants for the inclusion. This solution for anisotropic media can hence be used generally for anisotropic background media as well as inclusions that are intrinsically anisotropic and have a specified shape. A more recent development of the SC method by *Matthies* [2010, 2012] presents a combination of the geometric mean averaging and possibility to include inclusions in the matrix (GEO-MIX-SELF). The GEO-MIX-SELF method combines the geometric mean and self-consistent approximation.

Another type of effective media has been developed for layered media by using the specific mechanical boundary conditions implied by the fixed contact at the interface between elastic layers. The original idea was first published by *Riznichenko* [1949] and *Postma* [1955] and was further developed by *Backus* [1962] for isotropic layers, which may have different densities with vertical transverse isotropic (VTI) sample symmetry axis, and this method has attracted much interest in seismology and reservoir rock physics [e.g., *Mavko et al*., 2009; *Walker and Wookey*, 2012]. The formulation of the Backus average for finely layered media is given in detail by *Mavko et al*. [2009], who also provide a MATLAB script to calculate the

average either from isotropic Lamé's constants λ and μ (or equivalently by $C_{12}=\lambda$ and $C_{44}=\mu$, where $C_{11}=\lambda+2\mu$) or in terms of density, V_p, and V_s. *Backus* [1962] also proposed a long wavelength (λ_{lim}) limit where his average could be considered as an effective homogenous media with $\lambda_{\mathrm{lim}} >$ average layer thickness (h_{ave}). More recent work [e.g., *Melia and Carlson*, 1984; *Marion et al*., 1994; *Carcione et al*., 1991; *Lui and Schmitt*, 2006] introduce a wide range of parameters, including layer thickness, anisotropy of layers, wavelength, and incidence angle to layering. Both numerical modeling and experimental measurements found that ratio $R=\lambda_{\mathrm{lim}}/h_{\mathrm{ave}}$ should be at least 10, to be well described by an effective media. However, *Arntsen* [2007] found that the difference in seismic response between a periodic layer stack and an equivalent effective medium depends not only on wavelength but also significantly on reflection coefficients between layers and the ratio between layer thicknesses. For a 1% relative error in the phase velocity, and if all layers have the same thickness measured in vertical travel time, he found that the wavelength must be larger than approximately 3 times ($R=3$) the layer period for a weak reflection coefficient of 0.1, but if this increases to 13 times ($R=13$), the layer period for a very strong reflection coefficient of 0.9, which would be highly unrealistic in a geological setting. Previous studies have shown that in lower crust reflection coefficients were typically being between 0.1 and 0.2 [e.g., *Hurich and Smithson*, 1987; *Warner*, 1990], and hence, the errors will be quite modest.

A more general method for layers with arbitrary elastic symmetry was first proposed by *Helbig and Schoenberg* [1987] and refined by *Schoenberg and Muir* [1989]. In our notation we will follow *Schoenberg and Muir* [1989] where further details can be found. The elastic layers are defined as by stiffness tensors with up to 21 independent values for a medium with triclinic symmetry but can be applied to a higher symmetry, such as isotropic layers with two independent elastic constants. Each layer is associated with a density and thickness perpendicular to the layering, typically chosen to be vertical and parallel to the x_3 (or Z) elastic tensor axis. The method like that of Backus is based on the specific boundary conditions of a layered medium where there are displacements at the interfaces. The individual layer thickness must be small compared to the wavelength; the number of layers is not restricted to meet the requirements of equivalent effective medium. In this model the layers are considered to be horizontally continuous; not all geological situations meet this condition. The procedure is as follows: three submatrices of the layer stiffness tensor $\boldsymbol{c}_{ij}$ in Voigt notation are defined from boundary conditions of stress and strain for an elastic layer with fixed (or welded) interfaces.

There will be two or more layers numbered by the subscript (i), and in each layer the three submatrices $C_{NN(i)}$, $C_{TN(i)}$, and $C_{TT(i)}$ are constructed from the layer stiffness tensor $\boldsymbol{c}_{ij}$. The subscripts NN, TN, and TT are related to the N and T for normal and transverse components respectively of stress and strain of the boundary conditions.

$$C_{NN(i)}=\begin{bmatrix} C_{33(i)} & C_{34(i)} & C_{35(i)} \\ C_{34(i)} & C_{44(i)} & C_{45(i)} \\ C_{35(i)} & C_{45(i)} & C_{55(i)} \end{bmatrix},\ C_{TN(i)}=\begin{bmatrix} C_{13(i)} & C_{14(i)} & C_{15(i)} \\ C_{23(i)} & C_{24(i)} & C_{25(i)} \\ C_{36(i)} & C_{46(i)} & C_{56(i)} \end{bmatrix},\ C_{TT(i)}=\begin{bmatrix} C_{11(i)} & C_{12(i)} & C_{16(i)} \\ C_{12(i)} & C_{22(i)} & C_{26(i)} \\ C_{16(i)} & C_{26(i)} & C_{66(i)} \end{bmatrix}$$

The next step is to define the two scalar properties of model and their summation $g1=\sum_i^n H_i$ and $g2=\sum_i^n H_i\rho_i$, where H_i is the thickness and ρ_i is the density of the i^{th} layer.

The following operation is the calculation of 3×3 matrix properties of the model defined as $\underset{\sim}{g}3$, $\underset{\sim}{g}4$, and $\underset{\sim}{g}5$ as follows:

$$\underset{\sim}{g}3=\sum_i^n H_i C_{NN(i)}^{-1},\ \underset{\sim}{g}4=\sum_i^n H_i C_{TN(i)} C_{NN(i)}^{-1},\ \underset{\sim}{g}5=\sum_i^n H_i\left[C_{TT(i)}-C_{TN(i)}C_{NN(i)}^{-1}C_{TN(i)}^{t}\right]$$

where the superscript -1 is the inverse and t is the transpose of the matrix, respectively. The layer thickness weighted average are given in terms of g and $\underset{\sim}{g}$

$$\underset{\sim}{C}_{NN}=g1\underset{\sim}{g}3^{-1},\ \underset{\sim}{C}_{TN}=\underset{\sim}{g}4\underset{\sim}{g}3^{-1},\ \underset{\sim}{C}_{TT}=\left[\underset{\sim}{g}5+\underset{\sim}{g}4\underset{\sim}{g}3^{-1}\underset{\sim}{g}4^{t}\right]/g1$$

The resulting three thickness weighted matrices $\underset{\sim}{C}_{NN}$, $\underset{\sim}{C}_{TN}$, and $\underset{\sim}{C}_{TT}$ are used to construct the effective elastic layered model (M_{ij}), with triclinic symmetry. The analytical solution, which we present here for the first time of the Voigt 6×6 matrix, is as follows:

$$M_{IJ} = \begin{bmatrix} \underset{\sim}{C}_{TT(11)} & \underset{\sim}{C}_{TT(12)} & \underset{\sim}{C}_{TN(11)} & \underset{\sim}{C}_{TN(12)} & \underset{\sim}{C}_{TN(13)} & \underset{\sim}{C}_{TT(13)} \\ \underset{\sim}{C}_{TT(12)} & \underset{\sim}{C}_{TT(22)} & \underset{\sim}{C}_{TN(21)} & \underset{\sim}{C}_{TN(22)} & \underset{\sim}{C}_{TN(23)} & \underset{\sim}{C}_{TT(23)} \\ \underset{\sim}{C}_{TN(11)} & \underset{\sim}{C}_{TN(21)} & \underset{\sim}{C}_{NN(11)} & \underset{\sim}{C}_{NN(12)} & \underset{\sim}{C}_{NN(13)} & \underset{\sim}{C}_{TN(31)} \\ \underset{\sim}{C}_{TN(12)} & \underset{\sim}{C}_{TN(22)} & \underset{\sim}{C}_{NN(23)} & \underset{\sim}{C}_{NN(22)} & \underset{\sim}{C}_{NN(23)} & \underset{\sim}{C}_{TN(32)} \\ \underset{\sim}{C}_{TN(13)} & \underset{\sim}{C}_{TN(23)} & \underset{\sim}{C}_{NN(13)} & \underset{\sim}{C}_{NN(23)} & \underset{\sim}{C}_{NN(33)} & \underset{\sim}{C}_{TN(33)} \\ \underset{\sim}{C}_{TT(13)} & \underset{\sim}{C}_{TT(23)} & \underset{\sim}{C}_{TN(31)} & \underset{\sim}{C}_{TN(32)} & \underset{\sim}{C}_{TN(33)} & \underset{\sim}{C}_{TT(33)} \end{bmatrix} \tag{29}$$

Until now this method has been little used, but given the frequency of layered structures in the continental and oceanic crust, this method should find many applications. This method has been implemented in the MTEX software.

5.4. Asymptotic Expansion Homogenization-Finite Element Method

The asymptotic expansion homogenization-finite element (AEH-FE) method takes into account microfabric characteristics of CPO and elastic grain interactions [*Vel et al*., 2016]. The latter aspect makes it possible to estimate grain-scale geometrical effects, such as layering and SPO, on the overall elastic properties of the medium. The basic setup for calculations consists in producing a finite element mesh using a microstructural image as input (e.g., EBSD map). The finite element mesh can be adjusted to conform to the boundaries of grains, thereby better reflecting the interface between individual grains. The term $X_i^{kl}(\boldsymbol{y})$, which represents 18 location-dependent proportionality constants, is introduced with the AEH method and relates microscale displacements to average microscopic strains, at any point $\boldsymbol{y}$ in the finite element mesh. These constants are also known as characteristic functions, and they are used to describe the microscopic strains on grain scale to the average macroscopic strains. The aggregate elastic stiffness tensor takes into account both the averaging scheme related to mineral modal composition and their single-crystal elastic constants, as well as the elastic interaction among grains based on the finite element mesh, such that

$$C_{ijkl}^{\mathrm{AEH}} = \frac{1}{|V|}\int V\left(C_{ijkl} + C_{ijpq}\frac{\partial X_p^{kl}}{\partial y_q}\right)\mathrm{d}V \tag{30}$$

In equation (30), $|V|$ is the total volume of the sample or aggregate (area of microstructural map), integrated over small volumes (dV). In the integrand of the equation, both the Voigt bound and a second term are evaluated, the latter term which modifies the Voigt bound (c_{ijkl}) by consideration of elastic grain-scale interactions. Seismic wave speeds are solved using Christoffel's equation, similar to the velocities predicted with other averaging techniques. One of the drawbacks of this method is that the microstructural image cannot contain nonindexed areas (i.e., blank spaces), and sometimes this requires significant postprocessing of the EBSD data that can lead to introduction of artifacts into the microstructural data set. Artifacts resulting from processing "grain growth" therefore have to be considered during data processing. Another important constraint on the AEH-FE method is the assumption of periodically occurring microstructural arrangement, which should exceed the scale of the microstructural image (0.001 to 0.01 m) by more than 3 orders of magnitude (>1 m). However, such a periodic constraint is in any case required in order for a wave of seismic wavelength (tens of meters to thousands of meters) propagating through the Earth to be affected by the microstructural arrangement of crystals in a rock. Finally, the microstructures are considered infinite in the third dimension that is perpendicular to the microstructural image, because although the CPO data provide a 3-D analysis, the microstructural image is constrained to 2-D (thus affecting the layering and shape-preferred orientation of grains). *Naus-Thijssen et al*. [2011a, 2011b] have applied the AEH to hypothetical geological scenarios, considering deformed

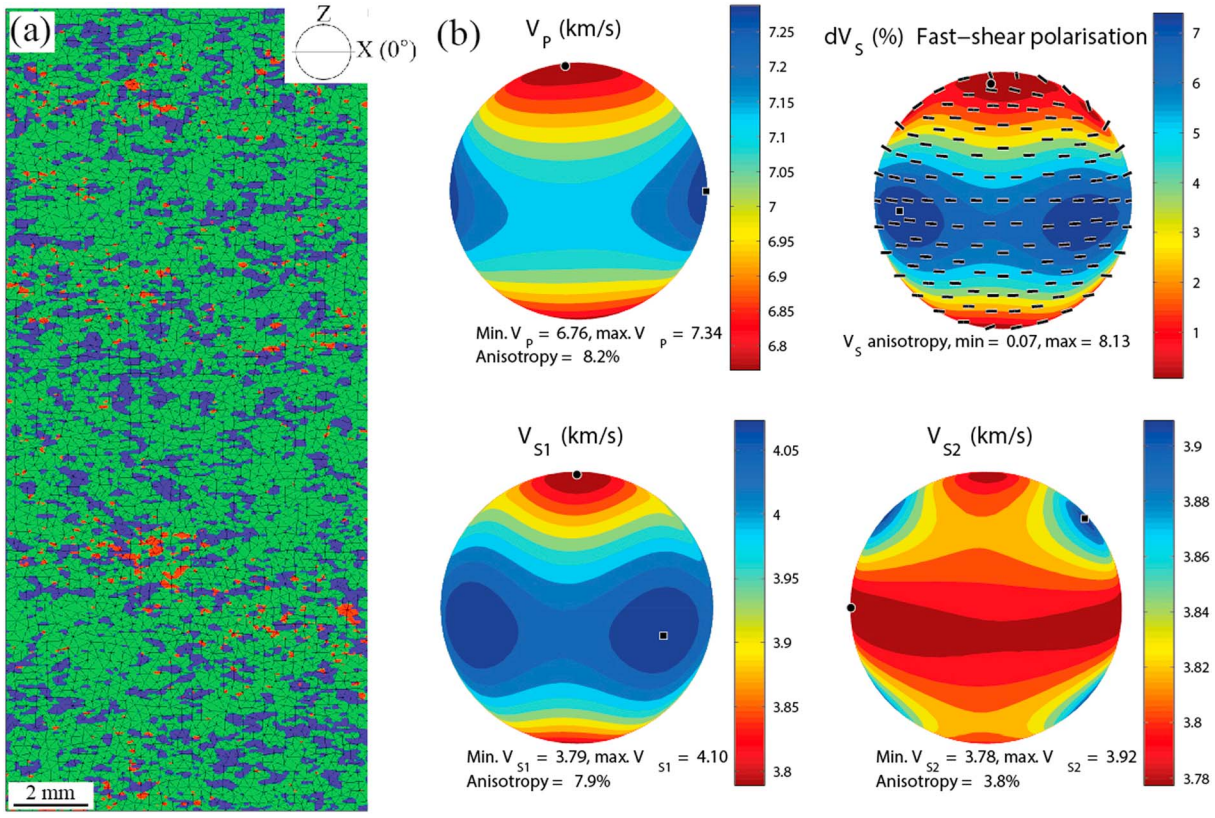

Figure 19. (a) EBSD map with overlain finite element mesh used for calculation of the seismic properties with the AEH. (b) Seismic velocity and anisotropy (V_P, AV_s, V_{s1}, and V_s2) resulting from the AEH. The results from the AEH are most suitably compared to the VRH results in Figure 14. Plotting the results uses the MSAT routine of *Walker and Wookey* [2012].

phyllosilicate-rich rocks, showing that microstructure can have a significant influence on elastic and seismic properties.

We have applied the AEH method to the microstructural data of the COSC193 sample. A finite element mesh was created based on the EBSD map, using the highest number of elements possible, with the elastic and seismic properties (ESPs) toolbox of *Cook et al.* [2013]. The EBSD map and FE mesh is shown in Figure 19a, together with the AEH calculation in Figure 19b, which show V_P, AV_s, V_{s1}, and V_{s2}. All points within the EBSD map belong to a mineral phase, with a specified crystallographic orientation.

5.5. Dynamic Wave Propagation

Zhong et al. [2014, 2015] adopted a different approach to predict and quantify seismic wave velocity and anisotropy, using a finite-element "dynamic" wave propagation model. They illustrated the technique with a peridotite sample from Ivrea-Verbano (northern Italy). The elastic wave propagation method uses a set of benchmarked finite element (and finite difference) numerical codes that solve for the propagation of a 2-D plane strain wave in a linear elastic medium [*Frehner et al.*, 2008]. The medium can consist of an SEM-EBSD image, or map, with both textural (CPO) and microstructural information. The finite element model is set up so that each pixel of the EBSD map contains information on the mineral phase and its crystallographic orientation (as measured with EBSD). Elastic waves can then be propagated across the map in any orientation, taking into account both the microstructure and CPO. This approach to model elastic wave velocity in different orientations is distinctly different than the averaging schemes discussed previously in this section, as the method can be considered "active" because waves actively propagate through the medium. The prediction of seismic properties of averaging schemes can be considered "static" because a wave does not propagate as an active elastic wave through the sample but is rather solved for using Christoffel's equation. The finite element method will furthermore yield an exact result, which is different from the theoretical

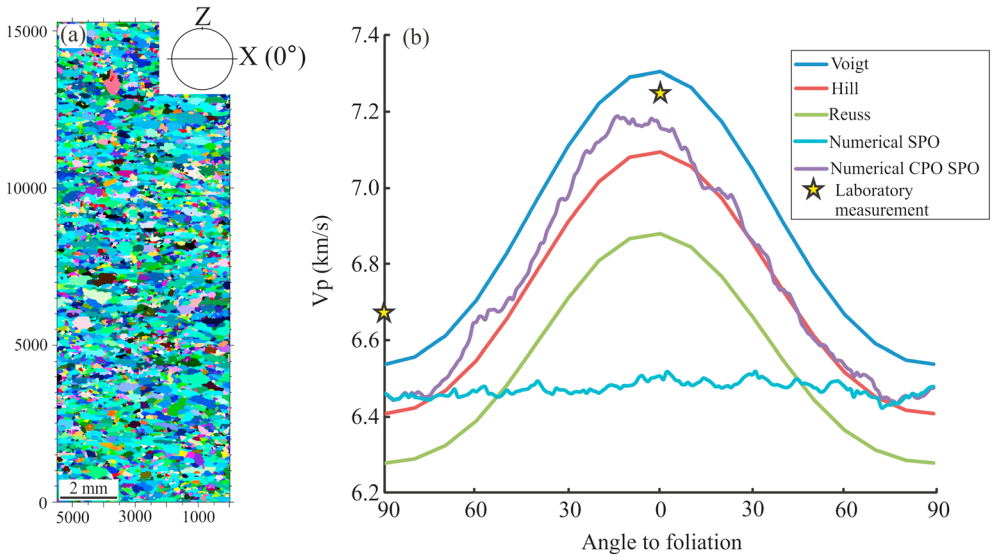

Figure 20. Directional V_p dependence using the dynamic wave propagation of *Zhong et al.* [2014, 2015] based on the microstructural map and CPO of sample COSC-193 (see Figures 16 and 17 for more information on the EBSD map and pole figure plots of the phases present in COSC-193). (a) Setup of microstructural map used for the dynamic wave propagation through the sample, foliation is horizontal in the image. (b) Directional dependence of V_p, shown by different modeling approaches. The numerical SPO and CPO + SPO refer to the effects of the respective effects of SPO and CPO on directional wave velocities. Even though the sample has clear SPO, the SPO does not contribute to directional differences in V_p. In contrast, the CPO has a large influence on directional dependence of the V_p. Stars indicate laboratory-measured V_p on sister samples of the COSC-193 sample, which show generally a good agreement with numerical CPO + SPO (laboratory data from *Wenning et al.* [2016]). This result indicates that SPO in the COSC-193 sample has little or no influence on the anisotropy of V_p.

bounds produced by averaging schemes. Another benefit of this method is the possibility to vary the wavelength of the propagated wave and in such a way enabling comparison with the short wavelengths used for laboratory ultrasonic measurements. Similar to laboratory measurements, scattering of elastic waves may need to be considered, when the wavelengths are close to the grain size of minerals in the aggregate.

Results from the dynamic wave propagation method are illustrated in Figure 20, showing the microstructural map of the COSC-193 sample (Figure 20a) and the directional dependence of the *P* wave for numerically solved V_p, as well as the Voigt, Reuss, and Hill bounds. The microstructural image illustrates that the sample has strong SPO (particularly of amphibole), where the long axis of grains tend to be parallel to the foliation plane. Although the SPO is strong, it apparently has negligible effect on the directional dependence of seismic velocity. This method could be compared with numerical modeling experiments published by *Birch* [1972]. His method was based on determining a velocity in random olivine aggregates calculated as total path length/total travel time. Birch's method was tested using aggregates with CPO by *Mainprice and Humbert* [1994] who found that the method gave result close to the Voigt bounds for grains with axial ratio of 1:1 but outside Voigt-Reuss bounds when the grains had axial ratio of 100:1.

5.6. Effective Elastic Properties of Cracked Elastic Media

The Voigt and Reuss bounds presented previously represent the earliest effective elastic media for crystalline aggregates with CPO. These simple averages involving the volume fractions of each element of the microstructure, such as the grain and its mean orientation and the elastic tensor in its appropriate grain orientation, provide a means of estimating the overall elastic properties of crystalline aggregates. But the Voigt and Reuss averages only use volume fractions and single-grain (or crystal) tensors with no consideration of the grain shape, no inclusions within grains or information on position in the aggregate. Hence, these averages are not suitable for describing the effects of cracks on elastic media. It is obvious that the presence of cracks will reduce the elastic stiffness and probably introduce anisotropy

depending on their orientation and thus reduce the elastic wave speeds. *Anderson et al*. [1974] convincingly demonstrated these aspects of the introduction of cracks using a simple *Eshelby* [1957]-*Walsh* [1969] inclusion model with one crack-like ellipsoidal inclusion into an isotropic matrix with the elastic constants of granite, and they used very low crack porosities of 0.01 to 0.005 to make the calculations as realistic as possible.

A more advanced form of effective medium will combine elastic tensor, volume fraction, and the spatial arrangement in two or three dimensions (microstructure) of the rock. The elastic contrast between the solid matrix and the pores, cracks, and their fillings, gas, liquid, fluid, or solids will have a major impact on the elastic heterogeneity or elastic contrast within the composite medium. The *Eshelby* [1957] inclusion model is the fundamental element of the self-consistent scheme (SCS) [e.g., *Willis*, 1977] and the differential effective medium (DEM) [e.g., *McLaughlin*, 1977], the two classical effective media methods. If like in the work of *Anderson et al*. [1974] there is a clear definition of roles of host matrix and crack-like inclusion, then a specific modeling scheme can be defined. If the microstructure is very complex, then combining several methods may be required as suggested by *Hornby et al*. [1994] for shales, *Le Ravalec and Gueguen* [1996] for saturated rocks with pore and crack porosity, and *Mainprice* [1997] for rocks with CPO and melt using a combination of SCS, DEM, and the poroelastic relationships of *Gassmann* [1951] at low frequency. *Matthies* [2012] combined Voigt, Reuss, geometric mean, and SCS in a single code for rocks with CPO, grain shape, and cracks. It is also interesting to note that in simple synthetic porous glass systems with a *P* wave velocity of 6 km/s for fully dense glass that SCS predicts the *P* wave velocity as a function of porosity of sintered glass beads where velocity drops to 2 km/s at porosity of 45%. However, for glass foam DEM predicts the change in velocity with increasing porosity with V_p of 3 km/s at porosity of 70% [*Berge et al*., 1993]. The authors suggested that a granular microstructure, such as sandstones, was better modeled by SCS, whereas rocks with isolated cracks and pores in a solid background would be best modeled by DEM, because of how each model takes into account the interaction of inclusions. The effective elastic properties of cracked material were first described by *Bristow* [1960] studying heavily cold-worked metals with microcracks. Bristow's paper was to have profound influence on the subject as shown by the fact that J. D. Eshelby brought Bristow's work to the attention of Budiansky and O'Connell. Bristow had developed a method that neglected interactions between cracks and had identified the importance of the scalar crack density. *Budiansky and O'Connell* [1976] used the SCS to calculate the elastic moduli of isotropic solids with a random population of cracks, but their study was limited to small crack densities and results in zero stiffness at low crack density of $9/16 \approx 0.56$ in the 3-D case; this has sometimes been interpreted as brittle failure, but it is more likely an artifact of the method as discussed below in terms of crack interaction [see *Kachanov*, 1994]. In their paper *Budiansky and O'Connell* [1976] defined an important concept, inspired by the work of Bristow, of the crack density parameter $\varepsilon = (2N/\pi)\langle A^2/P\rangle$ where N is the number of cracks, A = area of the crack surface, and P is perimeter of the crack outline. Indeed, in some papers this is called Budiansky-O'Connell-Bristow crack density parameter. For flat circular crack shapes, also known as penny-shaped cracks this reduces $\varepsilon = \langle \mathrm{Na}^3 \rangle$ where $a = ((2/\pi)(A^2/P))^{(1/3)}$ is the crack radius. The crack density parameter has become an important metric in studies of effective media of cracked material. *Bruner* [1976] and *Henyey and Pomphrey* [1982] have shown that SCS overestimates the crack interactions, whereas the DEM reduces the interaction as the crack density is increased incrementally in very small steps and the effective properties are recalculated at each interval.

Kachanov [1992, 1994] in his seminal review papers posed the question if cracked media are better described by a solid matrix with inclusions like the SCS and DEM methods or by a solid with cracks? Based on his previous work [*Kachanov*, 1980, 1987; *Vakulenko and Kachanov*, 1971] that introduced the second-order crack density tensor (α_{ij}), a new method was developed by *Sayers and Kachanov* [1991, 1995], which is a simple scheme based on estimating elastic stiffness tensor for an arbitrary orientation distribution of circular cracks at finite crack density. The scheme is based on the tensor transformation of the effective elastic constants for uniform orientation statistics via the second-order crack density tensor. The major results of the noninteracting scheme are that the results are linearly scaled using the crack density parameter, the elastic stiffness is positive at crack densities up to one for uniform, perfectly parallel and other arbitrary crack distributions that have been tested. In particular, the method gives for an isotropic matrix exact results for any orientation distribution in 2-D and 3-D. The noninteracting approximation (NIA) for cracks has a wider than expected range of applicability due to the canceling effects of stress shielding of arrays of interacting cracks. The

exact results have been published [*Kachanov*, 1992, 1994] for a uniform distribution of cracks with the crack density tensor $\alpha_{ij} = (\varepsilon/3)I$, where I is the unit tensor and hence

$$E = E_o\left[1 + \frac{16\left(1 - v_o^2\right)\left(1 - \frac{3v_o^2}{10}\right)}{9\left(1 - \frac{v_o}{2}\right)}\varepsilon\right]^{-1} \tag{31}$$

$$G = G_o\left[1 + \frac{16(1 - v_o)(1 - v_o/5)}{9\left(1 - \frac{v_0}{2}\right)}\varepsilon\right]^{-1} \tag{32}$$

$$v = \frac{E}{(2G)} - 1 \tag{33}$$

where E, G, and v are Young's modulus, shear modulus, and Possion's ratio of the cracked media. E_0, G_0, and v_0 are Young's modulus, shear modulus, and Poisson's ratio of the matrix material, and ε is the crack density. Using the elastic moduli, it is easy to compute the V_p and V_s for uncracked material as $V_{p0} = \sqrt{((G_0(4G_0 - E_0)/(3G_0 - E_0))/\rho)}$ and $V_{s0} = \sqrt{(G_0/\rho)}$ and cracked material by substituting G and E for G_0 and E_0, respectively. Extension of the NIA continues for various specific applications, like stress-dependent seismic anisotropy of shale [*Sayers*, 1999] and fluid-saturated cracked rock and elastic wave velocities as a function of frequency [e.g., *Schubnel and Guéguen*, 2003], where the mechanical failure threshold is close to a crack density of one for Oshima granite [*Schubnel et al*., 2003]. Two of the important parameters in the NIA are the ratio of normal to tangential compliance of fractures, which has been the subject of calibration [e.g., *Sayers*, 2009]. Some communities in Earth Sciences have been slow to apply these developments for modeling crack densities even though they were published in the 1990s.

Another development in cracked media, which is not unrelated to NIA and uses Hooke's law per unit volume as one of its fundamental equations, is

$$\varepsilon = S_{\text{matrix}}\,\sigma + \Delta S\,\sigma = S_{\text{matrix}}\,\sigma + \Delta\varepsilon \tag{34}$$

where ε and σ are the strain and stress, S_{matrix} is elastic compliance tensor of the matrix and the additional ΔS compliance introduced by cracks, and hence the effective compliance can be written as $S_{\text{effective}} = (S_{\text{matrix}} + \Delta S)$. Alternatively, one could write this in terms of stiffness tensors as $C_{\text{effective}} = (C_{\text{matrix}} + \Delta C)$ as done in first-order formulation of *Hudson* [1980] as both representations are equivalent, but summation in terms of compliance is recommended. The reason for this is that the NIA where extra compliance (ΔS) is summed has a linear relation to crack density and remains accurate to higher densities than (ΔC) [*Grechka and Kachanov*, 2006]. The physical reason behind this result is that ΔS is directly related to the extra strain ($\Delta\varepsilon$) introduced by the cracks as $\varepsilon = S_{\text{matrix}}\,\sigma + \Delta\varepsilon$.

A different logic was introduced for modeling fractures [*Schoenberg*, 1980; *Schoenberg and Douma*, 1988], which is called the Schoenberg's linear slip theory. A fracture can be modeled as an imperfectly bonded interface, across which the traction is continuous but the displacement may be discontinuous. *Schoenberg* [1980] uses B_N as the displacement discontinuity normal to the fracture for unit normal traction, and B_T gives the displacement discontinuity parallel to the fracture for unit shear to characterize fracture compliance matrix. Although crack and fracture are often used as synonyms, following *Kachanov et al*. [2010], we will use crack for a traction-free surface and fracture for two contacting rough surfaces. Schoenberg's method shares some of the features of Kachanov's noninteracting crack (NIC) approximation. In particular, it has the same concept as using compliance tensors $S_{\text{effective}} = S_{\text{matrix}} + S_{\text{fracture}}$, which means it is linear with crack density. However, there is no microstructural model associated with this method, for example, surface roughness if they are fractures in the sense of *Kachanov et al*. [2010]. We should point out that Schoenberg and coworkers use the word fracture in their publications. If we are discussing fractures, then crack density is no longer the correct metric; this is replaced by appropriate statistics of contacts for rough fractures. The simplest case is circular contacts with metric given by $\xi = N\langle\sqrt{A}\rangle$ where N is number of contacts per unit area and A is the contact area, and $\langle\ldots\rangle$ stands for average over contact areas [*Kachanov et al*., 2010]. However, to have accurate

values of ξ, the quantities that define N and $\sqrt{A}$ need to be known as a function of stress. We can make simple illustration of this method by taking the S_{matrix} that represents an elastic body with transverse isotropic medium and vertical (x_3) symmetry axis, where the nonnegative parameters B_T and B_N are the excess tangential and normal fracture compliances, respectively. In this case,

$$S_{\text{matrix}} = \begin{bmatrix} S_{\text{matrix11}} & S_{\text{matrix12}} & S_{\text{matrix113}} & & & \\ S_{\text{matrix12}} & S_{\text{matrix11}} & S_{\text{matrix3}} & & & \\ S_{\text{matrix13}} & S_{\text{matrix13}} & S_{\text{matrix33}} & & & \\ & & & S_{\text{matrix55}} & & \\ & & & & S_{\text{matrix55}} & \\ & & & & & S_{\text{matrix66}} \end{bmatrix} \tag{35}$$

$$S_{\text{effective}} = S_{\text{matrix}} + S_{\text{fracture}} = \begin{bmatrix} S_{\text{matrix11}} + B_N & S_{\text{matrix12}} & S_{\text{matrix113}} & & & \\ S_{\text{matrix12}} & S_{\text{matrix11}} & S_{\text{matrix3}} & & & \\ S_{\text{matrix13}} & S_{\text{matrix13}} & S_{\text{matrix33}} & & & \\ & & & S_{\text{matrix55}} & & \\ & & & & S_{\text{matrix55}} + B_T & \\ & & & & & S_{\text{matrix66}} + B_T \end{bmatrix} \tag{36}$$

where $S_{\text{matrix12}} + S_{\text{matrix66}}/2 - S_{\text{matrix66}} = 0$, which is analogue to $C_{\text{matrix12}} + 2C_{\text{matrix66}} - C_{\text{matrix11}} = 0$.

In this section we used the notation "fracture" to emphasize that no surface roughness is defined. *Schoenberg and Sayers* [1995] give other examples of several effective compliance tensors for "fractured" rock with different symmetries and "fractures" sets. This method is used under the assumption of long wavelength limit as effective homogeneous medium, where the wavelength is much larger than the fracture spacing. The fracture compliance tensor is constructed and the stiffness tensor obtained by inversion for the calculation of seismic properties. A comparison of the theory with ultrasonic experiments of *Hsu and Schoenberg* [1993] on a physical model fractured medium of parallel lucite plates with surfaces roughened by sand blasting shows that of $B_T \approx B_N$ for the case of air-filled fractures. Unfortunately, the contact area between the plates was not characterized, but as the measurements were done as function of applied stress, then it is probable that the contact area varied with stress. The effect of mineralization on the ratio B_N/B_T for fractures, studied by *Sayers* [2009], provides new values B_N and B_T that may be useful for geophysical applications to naturally occurring fractures. Fractures often exhibit mineralization in the form of mineral bridges or pillars between opposing faces of the fracture; if present, these would affect B_N/B_T ratios; these are fractures in the sense of *Kachanov et al.* [2010]. Finally, *Hood* [1991] showed that it is possible to decompose the fracture-induced anisotropy using matrix methods.

5.7. Software Packages

Since its initial introduction in the late 1960s and early 1970s, several methodological developments and modifications to predict seismic properties from rock microstructure have been made [*Mainprice*, 1990; *Mainprice et al.*, 2011; *Matthies*, 2012; *Walker and Wookey*, 2012; *Cook et al.*, 2013; *Zhong et al.*, 2014]. There are a number of publically accessible software packages available presently with the possibility to predict elastic properties and seismic velocities using the different approaches that have been presented. Common to all of the approaches is the consideration of the mineral CPO, whereas more specific techniques take into consideration the effect of the microstructure. Currently available packages include MTEX [*Hielscher and Schaeben*, 2008; *Mainprice et al.*, 2011, 2014; http://mtex-toolbox.github.io/:], the MATLAB Seismic Anisotropy Toolkit MSAT [*Walker and Wookey*, 2012; http://www1.gly.bris.ac.uk/MSAT/], the Elastic and Seismic Properties (ESP) toolbox [*Cook et al.*, 2013; *Vel et al.*, 2016; http://umaine.edu/mecheng/faculty-and-staff/senthil-vel/software/esp_toolbox/], and the Unicef Careware package [*Mainprice*, 1990; http://www.gm.univ-montp2.fr/PERSO/mainprice/W_data/CareWare_Unicef_Programs/]. In addition, the MTEX MATLAB scripts have recently been updated to take into account the consideration of the effect of layered media (i.e., as discussed in section 5.3).

6. Seismic Properties of the Continental Crust From the Mineral and Microfabric Perspective

The number of studies that have addressed seismic properties of crustal rocks using a modeling approach based on the textural (CPO) properties has grown rapidly in the last 25 years. The continental crust hosts a diverse set of minerals, where silicates comprise the vast majority (Figure 2). Through their volumetric contribution, these minerals are considered most important in terms of influencing seismic properties of the crust [*Christensen and Mooney*, 1995; *Rudnick and Fountain*, 1995; *Rudnick and Gao*, 2003, 2014]. In this section we discuss seismic attributes of the continental crust, considering the major continental rock-forming minerals, as well as their texture and microstructure. The discussion is centered mainly on studies that have used calculated or predicted seismic velocities, which are based on texture (CPO) and microstructure. Laboratory measurements provide very important quantitative data on the seismic velocity of the continental crust, but they are referred to only in specific cases in the following discussion.

6.1. Seismic Properties of Sedimentary Rocks

There is a large literature on seismic properties of sedimentary rocks, because of their value as reservoir rocks for oil and gas. Relevant references that broadly cover this subject are the "Rock Physics Handbook" by *Mavko et al*. [2009] and "Introduction to the Physics of Rocks" by *Guéguen and Palciauskas* [1994]. Seismic anisotropy of shale in particular has been an important topic of research, with emphasis of qualitative comparison of laboratory-measured ultrasonic wave velocities and preferred orientation of clay minerals [e.g., *Hornby*, 1998; *Johnston and Christensen*, 1995; *Wang*, 2002; *Sayers*, 2005; *Delle Piane et al*., 2015]. However, few studies have explored the predicted seismic properties and anisotropy of sedimentary rocks from the standpoint of calculating (and quantifying) seismic properties based on CPO and microstructural aspects. Notable exceptions are the works of *Valcke et al*. [2006], *Cholach and Schmitt* [2006], *Kendall et al*. [2007], *Lonardelli et al*. [2007], and *Wenk et al*. [2007], in which the role of microfabric was investigated for several different sedimentary rock types. Using a combination of XRD goniometry and EBSD, *Valcke et al*. [2006] quantified the seismic properties for a set of shales, siltstones, and sandstones. Sandstone samples consisted mainly of quartz, with minor amounts of feldspar (K-feldspar and albite) and clay minerals. Seismic *P* wave anisotropy $\leq$2.6% and maximum shear wave anisotropy $\leq$3.1% resulted from calculations. In contrast, mud-rich siltstone and shale gave rise to moderate to high *P* wave anisotropy, ranging from 4.5% to 11.1% and maximum *S* wave anisotropy from 3.7% to 9.8%. The source for the anisotropy can be related to clay minerals (illite and kaolinite) and mica content in the samples, which amounts to $>$27% by volume in the mud-rich siltstone and shale. In a similar study, *Cholach and Schmitt* [2006] quantified the role of mica and clay minerals on seismic anisotropy in shale and schist lithologies. The phyllosilicate-rich lithologies yielded high anisotropy, and different effective medium averaging schemes were investigated in terms of expressing seismic anisotropy. They concluded that in highly anisotropic sedimentary rocks, where phyllosilicates give rise to seismic anisotropy, the theoretical Voigt and Reuss bounds yield wide bounds on the predicted seismic anisotropy. The geometric mean was found as a more appropriate averaging scheme to define seismic anisotropy and provided a good comparison with ultrasonic laboratory measurements.

Kendall et al. [2007] investigated seismic anisotropy in Carboniferous-Devonian age sandstones from the Clair field, obtained offshore of Scotland. The study incorporated seismic property data from the microscopic scale to reservoir scale. The integration of different scale-dependent data is challenging, but the study of *Kendall et al*. [2007] provides a unique approach to study scaling of seismic anisotropy in reservoir rocks. Intrinsic rock anisotropy was found to depend mainly on the CPO of mica and secondarily on the crystallographic orientation of feldspar and quartz. One of the main findings of the study was that intrinsic anisotropy on microscopic scale could be applied generally to the entire reservoir, because the sandstones throughout the reservoir had similar mineral composition and CPO attributes. Integration of data from different scales presents a promising venue for future research, as the geological information obtained from seismic data may be interpreted in a more rigorous way when it is constrained by predictions at microscopic scale.

Shale has received some particular attention in regard to elastic and seismic properties, because of their economic importance in tight oil and gas reservoirs and due to the significantly anisotropic seismic velocities. *Lonardelli et al*. [2007] and *Wenk et al*. [2007] used synchrotron X-ray diffraction to measure CPO in illite/smectite- and kaolinite-bearing shale and illite-rich shale, respectively. The two studies could clearly link texture of clay minerals with strong elastic (and seismic) anisotropy. *Vasin et al*. [2013] modeled seismic properties of

Kimmeridge shale, based on microstructural and CPO information. A differential effective medium model was applied, taking into account grain shape, CPO, and pore-space properties, in order to explain measured acoustic velocities in the shale. *Kanitpanyacharoen et al.* [2015] have provided further insight into elastic anisotropy of shale, from a microstructural and CPO point of view. They studied the Muderong Shale from Australia, using two different effective medium models, (1) a combined self-consistent modeling scheme (GeoMIXself) [*Matthies*, 2010] that takes into consideration both CPO, as well as grain and pore aspect ratios, and (2) a differential effective medium model. The studies of *Vasin et al.* [2013] and *Kanitpanyacharoen et al.* [2015] indicate that purely CPO-based models are not appropriate for modeling the seismic properties of shale, and microstructural and porosity factors need to be considered.

6.2. Seismic Properties of Middle and Lower Continental Crust

In middle and lower crust settings the seismic properties and anisotropy tend to be controlled by the mineral composition and the tectonic setting. Among the most promising candidate minerals to generate texture-related anisotropy are mica (muscovite and biotite) and amphibole. These two groups of minerals generally produce both strong CPO and SPO. CPO-derived amphibole seismic properties and anisotropy have been investigated by several groups [*Siegesmund et al.*, 1989; *Kitamura*, 2006; *Barberini et al.*, 2007; *Tatham et al.*, 2008; *Ji et al.*, 2013]. It is also acknowledged that micas (in particular biotite and muscovite) are the most anisotropic phases in the middle and lower crustal rocks, and they may contribute significantly to seismic anisotropy [*Weiss et al.*, 1999; *Lloyd et al.*, 2009; *Erdman et al.*, 2013; *Shao et al.*, 2016]. *Tatham et al.* [2008], *Lloyd et al.* [2009], and *Lloyd et al.* [2011a, 2011b] introduced a rock recipe configuration to address interpretation of seismic anisotropy in the ductile middle and lower crust. The premise of this methodology is to measure mineral CPO for common rock-forming minerals present in middle and lower crust and vary their modal mineral composition, in order to explore the relative contribution to seismic anisotropy from individual minerals and the resulting strength and geometry of seismic anisotropy. Feldspars and quartz are also fundamentally important in consideration of seismic properties and anisotropy of the middle and lower crust because of their volume contribution and relatively strong single-crystal anisotropy.

Mica- and amphibole-rich rocks have considerably different single-crystal elastic properties related to their crystal symmetry, and the CPOs that develop in each of the rock types tend to give rise to different seismic velocity symmetry [*Ji et al.*, 1993; 2013, 2015; *Ko and Jung*, 2015]. Mica-rich rocks tend to show transverse isotropic symmetry, where the pole to the foliation plane coincides with the slowest velocity (*c* axis), with $V_p\ (X) \sim V_p\ (Y) > V_p\ (Z)$. In contrast, amphibolites tend to develop orthorhombic symmetry, with $V_p(X) > V_p\ (Y) > V_p(Z)$, because of the tensor diagonal single-crystal elastic constants $c_{33} > c_{22} > c_{11}$. However, it should be noted that for amphibolites, the appearance of the anisotropy depends on the deformation conditions and how the CPO develops in relation to the macroscopic rock fabric. *Ko and Jung* [2015] have experimentally determined three types of amphibole fabrics (types I, II, and III) that develop depending on the differential stress applied and temperature. They made two key observations, which were based on the experimental results. First, there are clear differences in the position of the pole to (010) and the orientation of the *c* axis [001] between their type I and type II CPOs of amphibole. Second, the difference in inferred seismic properties becomes minor when amphibole is deformed at high dipping angle with respect to a horizontal shear plane.

The Ivrea zone in northwestern Italy has served as an important locality for studying both laboratory and texture-derived seismic properties of continental lower crust [e.g., *Fountain*, 1976; *Burlini and Fountain*, 1993; *Barruol and Mainprice*, 1993; *Barruol and Kern*, 1996]. *Siegesmund et al.* [1989] provided some of the early joint laboratory measurements and texture-derived seismic properties for an amphibolite sample from Ivrea-Verbano. The strong CPO and high amount of hornblende were the main sources for inferring significant seismic anisotropy in the amphibolite. Measured AV_p, at 600 MPa confining pressure, reached 9.5%, whereas shear wave anisotropy was slightly lower at 7.0%. The texture-derived anisotropy were slightly lower, with $AV_p = 6.4\%$ and maximum $AV_s = 5.0\%$. *Barruol and Mainprice* [1993] investigated the texture-derived seismic properties for a set of eight lower crust rock types from Val Sesia in the Ivrea zone, including mafic and ultramafic lithology (dunite, pyroxenite, and gabbro), as well as more felsic rocks (diorite, stronalite, and kinzigite). The seismic anisotropy of the more felsic lithologies is dominated by mica and can reach ≥7% for maximum AV_s and AV_p [*Barruol and Mainprice*, 1993]. The mafic lithologies showed weaker and more complex anisotropy, generally <5% AV_p, with the exception of the ultramafic dunite, which showed nearly 10% AV_p. *Barruol and Kern* [1996] reported additional results of texture-predicted and laboratory-measured seismic velocities from the

Ivrea zone (Val Strona, Valle d'Ossola, Val Mastallone, and Val Sesia). The laboratory-measured V_p and V_s range from 6.0 to 7.5 km/s and 3.6 to 4.2 km/s, respectively, which are indicative of lower (and middle) crust seismic wave speeds. Biotite-gneisses and mafic amphibolites showed the highest anisotropy, with AV_p up to 10% and shear wave splitting (dV_s) up to 0.6 km/s. *Barruol and Kern* [1996] made a detailed comparison between measured (at conditions of 600 MPa) and calculated seismic velocities. Seismic velocities determined by the two methods deviated within a range of ±5%. In some cases the measured velocities were lower than calculations, but in other cases the opposite occurred. The comparison of V_p measured normal to foliation (V_{pz}) showed a relatively lower deviation (~ ±2%) than V_p in the foliation plane (V_{px} and V_{py}).

Erdman et al. [2013] investigated the calculated seismic properties for a range of different metamorphic lithologies and leucogranites from the Basin and Range area in western United States (Funeral Mountains, Ruby Mountains, and East Humboldt Range). Samples included paragneisses, calc-silicates, quartzofeldspathic gneisses, marbles, leucogranite, and granodiorite. Detailed mineral composition and CPO were determined for the different lithologies and used to calculate seismic velocities and anisotropy. Predicted bulk V_p and V_s range from 5.8 to 7.3 km/s, and 3.4 to 4.0 km/s, respectively, and thus the span in velocity for samples from the Basin and Range region span velocities expected throughout the entire middle to lower crust. The overall highest V_p and V_s were found in calc-silicate-rich samples from the Ruby Mountains, where the high velocities can be attributed to the presence of calcite and pyroxene. It was noted that all lithologies investigated showed a seismically transverse isotropic symmetry, with a unique slow velocity axis normal to the foliation. The largest seismic anisotropies are found in biotite- and muscovite-rich gneisses. However, the lithology matters as well, as near-isotropic leucogranites also can carry substantial amounts of biotite. In this case, however, the overall CPO of minerals is weak, leading to weak anisotropy. A few of the quartz-rich gneisses (>90% by volume quartz) display AV_p and AV_{smax} of nearly 10% or higher, which implies highly deformed quartzitic gneisses with strong quartz CPOs.

Llana-Fúnez et al. [2009] and *Llana-Fúnez and Brown* [2012] conducted a detailed study of calculated and measured seismic velocities across the continental crust to Moho transition in the Cabo Ortegal nappe complex in northwestern Spain. They investigated a suite of different lower crustal rocks, including felsic gneisses, eclogites, intermediate to mafic granulites, and olivine websterites. The crustal felsic gneisses show the highest AV_p (8.0% to 11.3%) and AV_s (7.9% to 10.5%), followed by a significantly weaker anisotropy in high-pressure granulites (AV_p = 1.6% to 6.1% and AV_s = 0.8% to 3.7%) and eclogite (AV_p = 0.6% to 5.0% and AV_s = 0.6% to 4.3%), and the weakest anisotropy in the ultramafics (AV_p = 2.2% to 3.3% and AV_s = 0.8% to 1.5%). Mainly mica (muscovite and biotite) is contributing to strong seismic anisotropy in felsic gneisses, whereas pyroxenes (omphacite and diopside) and amphibole contribute to the anisotropy in eclogite and high-pressure granulites. The mantle ultramafics show weak anisotropy as a consequence of weak olivine and pyroxene CPOs. As argued by *Llana-Fúnez and Brown* [2012], knowledge about possible seismic anisotropy is important for interpretation of lower crust composition, as well as deformation state at the crust-mantle transition. An interesting point made by the authors was the role of plagioclase-in and plagioclase-out reaction fronts, which could potentially create strong contrast in seismic reflectivity at the Moho.

Deformed rocks and mylonites related to shear zones have been investigated in some detail from a seismic textural and microstructural perspective. There are two lines of investigation with questions related to the study of seismic properties of mylonites: (1) Do mylonites develop intrinsic seismic anisotropy because of ductile deformation? (2) Can mylonites (and ductile shear zones) act as crustal seismic reflectors when juxtaposed to their protoliths, because of their intrinsic seismic properties? There are rather antithetic views in the literature on this subject, but a number of studies exist that deal with the topic of seismic properties of mylonites [e.g., *Burlini et al*., 1998; *Lloyd and Kendall*, 2005; *Ward et al*., 2012; *Almqvist et al*., 2013; *Lamarque et al*., 2016]. In order for reflections to occur at the interface of protolith and mylonite, there needs to be a substantial difference in the acoustic impedance between the two layers [e.g., *Rey et al*., 1994]. In shear zones, one of the reasons for differences in acoustic impedance is strain localization and development of CPO. However, strain localization and mylonitization may also decrease the CPO because of diffusion creep and grain boundary sliding deformation mechanisms. In such cases the CPO will not contribute to seismic anisotropy (and acoustic impedance) across the shear zone.

Certain configurations of mineral CPOs may yield destructive interference in terms of seismic anisotropy. *Ward et al*. [2012] predicted seismic velocities and anisotropy for two-phase mixtures of quartz and mica

and the modal composition of the two phases. At ~20:80 ratio of mica to quartz, the predicted seismic anisotropy reaches a minimum. Basal *a*-slip needs to be the active deformation mechanism in quartz leading to a concentration of *c* axes normal to the foliation, in order to yield this minimum in anisotropy. Destructive interference in this case arises because the seismically fast *c* axis of quartz, which orients normal to the foliation plane when basal *a*-slip is active, is parallel to the slow mica *c* axis. However, the quartz textures that develop during deformation are temperature dependent, and the actual seismic anisotropy that develops is governed by deformation conditions [*Paaschier and Trouw*, 2005]. Similarly, *Lamarque et al*. [2016] indicate that the interaction between CPOs of different minerals will tend to weaken the overall calculated seismic anisotropy, for example, in aggregates containing mixtures of feldspar, quartz, and pyroxene or mixtures of quartz and mica. Combined laboratory and texture measurements provide additional insights into the seismic properties of shear zones. *Cirrincione et al*. [2010] noted that seismic anisotropy decreased toward the highest strained portion (ultramylonite) of a shear zone in Montalto (Calabria, southern Italy), even though quartz CPO was high in this section of the shear zone. The presence of mica was found to be the most important factor in producing seismic anisotropy related to the shear zone. In contrast, shear zones that develop in carbonate rocks, with strong CPO of calcite (together with secondary presence of mica), have been suggested as a possible source for crustal-scale seismic reflections [*Burlini et al*., 1998; *Khazanehdari et al*., 1998; *Almqvist et al*., 2013]. The strong elastic anisotropy in deformed carbonates is found both in laboratory measurements and in calculated seismic properties from calcite CPO measurements, although discrepancies in the magnitude of anisotropy can occur, which need to be attributed either to small amounts of secondary phases or other microstructural features [*Burlini and Kunze*, 2000; *Almqvist et al*., 2013].

Metamorphic reactions are also important in determining seismic properties of metamorphic rocks. *Llana-Fúnez and Brown* [2012] noted that clinopyroxene chemical breakdown to plagioclase could represent a source contributing to increased seismic reflection at the petrological Moho. The slower velocities of plagioclase, compared to clinopyroxene, would increase the difference in acoustic impedance between the granulites in the lower crust (plagioclase bearing) and ultramafics of the upper mantle, and this potentially creates strong seismic reflectors. As an alternative, *Mookherjee et al*. [2016] showed that albite conversion to jadeite and quartz can lead to $>$1 km/s increase in velocity, from ~6.5 km/s to ~8.1 km/s. Such conversion may be occurring during the formation of the continental Moho, which would ultimately provide a very strong seismic impedance contrast between the feldspar-rich crust and the jadeite-rich mantle [i.e., *Jagoutz and Behn*, 2013].

Feldspars are the major constituents of the crustal mineral inventory (Figure 2). Several studies have investigated the seismic velocities and anisotropy related to CPO of plagioclase [*Ji and Mainprice*, 1988; *Seront et al*., 1993; *Satsukawa et al*., 2013; *Ji et al*., 2014]. One of the earliest studies on seismic properties from plagioclase CPO was carried out by *Ji and Mainprice* [1988], where calculated seismic velocities were provided for two samples with a composition of An_{53} (in the anorthite-albite solid solution series). *Ryzhova*'s [1964] elastic constants for plagioclase, at room temperature and pressure conditions, were used in calculations and resulted in V_p ranging from 6.12 to 7.15 km/s ($AV_p = 14.4\%$) and from 5.96 to 7.21 km/s ($AV_p = 17.3\%$). *Feinberg et al*. [2006] studied preferred orientation of plagioclase and pyroxene in gabbronorites from the Bushveld complex. They noted the strong CPO of plagioclase as a source for seismic anisotropy in the layered intrusion, with potential AV_p ranging from 4% to 8%, with a vertical axis of maximum velocity. *Seront et al*. [1993] carried out both laboratory velocity measurements and calculations of seismic velocities from samples of Oklahoma anorthosite, consisting by volume of 90% plagioclase and 10% olivine. It was found that laboratory velocities (measured at 0.8 GPa confining pressure) tended to exceed velocities predicted from texture-derived seismic properties. The calculated seismic anisotropy was substantial, with $AV_p = 11.8\%$ and $V_{s1} - V_{s2} = 0.5$ km/s. *Satsukawa et al*. [2013] compiled a set of 172 plagioclase CPO patterns in gabbroic rocks. Although this data set mainly applies to the oceanic crust, some insights into the seismic properties and anisotropy are applicable to magmatic rocks that occur in the continental crust. Maximum AV_p and AV_s for calculated seismic anisotropy, based on the set of plagioclase, reached 12% and 14%, respectively. *Ji et al*. [2014] further investigated the texture-related seismic properties of anorthosite, originating from layered mafic and ultramafic intrusions in lower continental (and oceanic) crust. Their findings indicate that the layered (laminated) plagioclase-rich rocks can give rise to significant seismic anisotropy, as well as act as source rocks for seismic reflections in lower crustal settings [i.e., *Meissner et al*., 2006]. Calculated seismic anisotropy ranged from 8.2% to 12.7% for AV_p and from 10.1% to 16.1% for maximum AV_s. The results of studies listed above therefore indicate that seismic anisotropy in layered intrusions can be significant, because of strong CPO

of plagioclase. Feldspars may, in general, be more important for seismic anisotropy in the crust than previously recognized.

6.3. High-Pressure and Ultrahigh-Pressure Rocks

High- and ultrahigh-pressure metamorphism of continental crust is generated in subduction zone settings and in crustal settings where crust becomes overthickened, for example, during orogeny. Seismic velocities and anisotropy in such a setting may yield insight into the physical and chemical conditions at depth, and calculated velocities based on rock samples of once deeply buried high-pressure rocks can be of importance. As an extreme of the continental crustal rocks, the seismic properties of high-pressure and ultrahigh-pressure rocks are, in general, considerably different than those of rocks in typical continental crust settings. Several studies have used calculated seismic velocities based on exhumed and exposed rock samples, including eclogites, ultrahigh-pressure rocks, and peridotites [*Ji et al*., 2003; *Wang et al*., 2005a, 2005b; *Xu et al*., 2006; *Wang et al*., 2009; *Bascou et al*., 2001; *Brownlee et al*., 2011; *Worthington et al*., 2013; *Cao et al*., 2013; *Jung et al*., 2013].

6.4. Microstructural Versus Textural Considerations in Seismic Anisotropy

How important is the microstructure for seismic anisotropy? The majority of predictive seismic anisotropy modeling studies only takes into account the CPO and modal mineral composition as sources for seismic anisotropy, despite indications and suggestions from some studies that microstructure has an impact on anisotropy [e.g., *Burlini and Kunze*, 2000; *Kern et al*., 2008]. One of the factors that make simple CPO volume fraction method acceptable in many cases is that minerals with significant aspect ratios are also minerals with a very strong elastic anisotropy. In these minerals the shape of the mineral and elastic anisotropy are both linked to the crystal structure, so that the shape factor has little influence on overall aggregate properties. The situation is entirely different for cracks, where the cracks have negligibly small elastic constants (unless they are fluid filled), although crack shape has a very important impact on the overall elastic constants [e.g., *Mainprice*, 2000]. Consideration of the microstructure takes into account (1) the shape-preferred orientation (SPO) of grains, (2) the effect of grain boundaries, and (3) the geometrical arrangement of grains and their elastic interaction in the aggregate (for example, layering). Recent studies [e.g., *Naus-Thijssen et al*., 2011a, 2011b; *Matthies*, 2010, 2012; *Wenk et al*., 2012; *Zhong et al*., 2014, 2015] have taken into account the role of microstructure and geometrical arrangement of phases in the rock, when calculating seismic velocities.

The mismatch of laboratory and calculated velocities, encountered by *Kern et al*. [2008] for a biotite-gneiss sample recovered from the Outokumpo borehole (Finland), prompted *Wenk et al*. [2012] to reconsider the calculation scheme used to predict the seismic properties for this sample. Differences between measured and calculated V_p were considerably different, where calculated values tended to overestimate laboratory measurements (when compared with measurements conducted at 200 MPa confining pressure). In addition, the measured V_p anisotropy (13.0% to 15.1%) was ~5–7% higher than the calculated V_p anisotropy (8%). *Wenk et al*. [2012] used the GeoMIXself method of *Matthies* [2010, 2012] in order to take into consideration grain shape of biotite. In addition, they carried out textural measurements with a neutron diffraction time-of-flight technique analyzed with the Rietveld technique. This yielded significantly stronger CPO of biotite than had originally been determined by *Kern et al*. [2008] and hence a stronger seismic anisotropy. The final calculation of *Wenk et al*. [2012] resulted in 12.9% AV_p, and the absolute velocities determined from each method agreed, in general, fairly well for different sample axes, *X*, *Y*, and *Z* (with the highest difference of ~3% parallel to the axis of lineation).

Naus-Thijssen et al. [2011a] used the asymptotic expansion homogenization (AEH) method, combined with Voigt-Reuss-Hill bounds, to constrain the elastic properties and anisotropy for a modeled mixture of quartz and muscovite. Particular to this method is the possibility to take into account elastic interactions of minerals on the grain scale. *Naus-Thijssen et al*. [2011a] focused on the geometrical arrangement of the mica and how this effect could influence the seismic anisotropy. Their conclusions are that microstructure (SPO and layering effects) may have considerable influence on seismic anisotropy. Notably, the AEH method does not take into consideration the effect of grain boundaries but only the grains themselves. Creating the 2-D medium used for the AEH analysis requires that there are no pixels that are not occupied by a mineral phase (i.e., nonindexed pixels in EBSD maps are not allowed). The results can therefore be biased somewhat by the processing the EBSD data, which requires that grains measured during the SEM-EBSD analysis are grown so that they juxtapose. In contrast to the results of *Naus-Thijssen et al*. [2011a], *Zhong et al*. [2014, 2015] show through

numerical modeling of elastic wave propagation that SPO has a negligible effect on seismic anisotropy in peridotite composed of mainly olivine and phlogopite.

In Figures 18 to 20 we present the results from a set of calculations, using MTEX, the AEH-FE method, and dynamic wave propagation [i.e., *Zhong et al*., 2014], which are calculated based on microstructural and textural analyses. The sample (COSC193) is a fairly homogeneous amphibolite collected from a scientific deep drilling project in the central Scandinavian Caledonides (Collisional Orogeny in the Scandinavian Caledonides; COSC). This sample is a suitable representative for metamorphosed mafic parts of the middle and lower continental crust. From the EBSD image (Figure 15), the modal composition was determined to be 67.0 area% amphibole (hornblende), 23.0 area% plagioclase (anorthite), 2.3 area% quartz, and <1 area % accessory phases of apatite, titanite, and pyrrhotite. Nonindexed zero solutions constituted 7.1 area% from the EBSD imaging, and the modal composition of the aggregate was normalized to 100%, thus correcting for zero solutions when calculating seismic properties. Texture strength of the amphibole, plagioclase, and quartz is shown in Figure 17, showing that both amphibole and plagioclase have fairly strong CPO, whereas the quartz CPO is weak (and make a negligible contribution to the seismic properties of the sample, because of its low volume). The SPO is also strong, with prominent elongated hornblende grains in the foliation plane. Accessory phases were not considered in the seismic calculations. Comparing results calculated using the three different methods shows that there are generally small differences in absolute values of V_p and V_s. Highest V_p and V_s are predicted with the Hill average computed using the MTEX, whereas the lowest velocities are predicted with the dynamic wave propagation method [*Zhong et al*., 2014, 2015]. Predicted seismic anisotropy is highest for the dynamic wave propagation method, although a prediction is only made for V_p ($AV_p = 11.1\%$). The MTEX and AEH-FE methods show fairly similar predicted anisotropy, with AV_p of 8.5% and 8.2%, and maximum AV_s of 7.3% and 8.1%, respectively. The SPO appears to have very little influence on the directionally dependent seismic velocity, as seen both from the AEH-FE and dynamic wave propagation methods, and for this amphibolite sample the CPO is the dominant contributor to the seismic anisotropy.

This is further supported by laboratory measurements, which were performed on the same sample material as the predictions were made and shown for comparison in Figure 20. Measurements represent the "crack-free" (V_0) velocities, which are based on measurements up to 300 MPa pressure. As discussed previously, this is likely not high enough pressure to close all microcracks and a contribution to velocity from cracks must therefore be considered. Compressional velocities in the X (parallel to lineation) and Z (normal to foliation) directions are shown in Figure 20, with highest velocity parallel to the lineation ($V_{px} = 7.23$ km/s) and slowest V_p normal to the foliation ($V_{pz} = 6.67$ km/s). The resulting anisotropy is smaller than all predictions, $AV_p = 8.0\%$, but agrees well with predictions made using the AEH-FE and MTEX methods. Although SPO does not appear to be of considerable importance in this sample, other studies indicate important cases for SPO- and microstructure-influenced seismic properties and anisotropy.

6.5. Intrinsic Versus Apparent Seismic Anisotropy

Seismologists tend to refer to the CPO-related seismic anisotropy as intrinsic and seismic anisotropy arising from small-scale heterogeneities, such as layering, SPO, and crack and fracture networks as apparent (or extrinsic) anisotropy. Separation of intrinsic and apparent seismic anisotropy is of considerable importance when trying to deduce the geological source and geodynamic processes responsible for the anisotropy. Intrinsic anisotropy is important when attempting to infer mantle flow directions based on olivine CPO, as well as for crustal and core geodynamics. Most geodynamic models that attempt to infer mantle flow regimes consider the mantle as a homogenous medium, without small-scale heterogeneities. The separation of the two is, however, challenging. *Fichtner et al*. [2013] have remarked that currently available seismic observables are not able to distinguish intrinsic from apparent anisotropy. Similarly, *Wang et al*. [2013] indicate that layering effects may in some cases be indistinguishable from CPO-related seismic anisotropy. The seismological, geodynamic, and rock physics communities are therefore facing a challenge when interpreting seismic data, using predictions based on CPO and effective medium models. A more integrated effort is likely needed, where the seismological, geodynamic, microstructural, and rock physics communities come together to address the source of the seismic signatures in Earth's crust and in the deeper Earth interior.

Some effort has been made to this end. *Lloyd et al*. [2011a, 2011b] considered purely texture-based calculations, in so-called rock recipe models. These models use measured mineral CPOs and vary the

modal composition of the different minerals. In such a way it becomes possible to explore the effect on seismic properties and anisotropy based on a wide variety of modal compositions. The CPO can also be changed, considering, for example, different deformation regimes (i.e., pure shear versus simple shear). Another approach is to actively combine prediction of seismic velocities obtained from samples in regional field studies and use these data to constrain seismological data in the same region. Examples are recent studies by *Cossette et al*. [2015a, 2015b], in the Aegean region, and *Xie et al*. [2015], in the Basin and Range province.

Few studies have attempted to reconcile both the effects of the texture and small-scale heterogeneities (microstructural parameters, cracks and fractures, and melt and fluids). The self-consistent approximation and differential effective medium model are two useful approaches to take into account both the intrinsic and apparent seismic anisotropy [e.g., *Mainprice*, 1997; *Nishizawa and Yoshino*, 2001; *Almqvist et al*., 2011; *Vasin et al*., 2013; *Kanitpanyacharoen et al*., 2015]. Cracks and fractures are fluid bearing, brine filled in the upper crust and potentially melt bearing in the middle and lower crust. *Mainprice* [1997] used a range of different effective medium models to predict seismic properties in a mixed solid and liquid (melt) medium, where the solid consisted of an anisotropic background with mantle peridotite composition, and the inclusion consisted of a basaltic melt with different geometries. *Hacker et al*. [2014] have integrated predicted seismic velocities derived from CPO, with a model that predicts seismic velocities in melt-bearing rocks. Results indicate that small amounts (~2 vol %) of granitic melt have a large impact of the seismic properties of an aggregate. Low seismic shear velocities in the middle to lower crust of the Tibetan Plateau do not therefore necessarily imply the presence of large amounts of fluids or melt.

Effective medium models are suitable in terms of addressing the combined effect of microfabric and fluid-bearing media. A particular challenge in incorporating fluids into averaging models is that a fluid-bearing medium does not exhibit a pure elastic response to a passing seismic wave (neither is this the case for solid aggregates of crystals, but the effect is much smaller). The fluid-bearing medium behaves viscoelastically and can display considerable seismic attenuation. Future applications must therefore incorporate factors of anelasticity and poroelastic theory [e.g., *Müller et al*., 2010; *Grab et al*., 2017], although much further work is required to understand how seismic anisotropy is influenced in such cases.

7. Conclusions

The continental crust is imaged at high resolution using a combination of active and passive seismic methods. Seismic anisotropy is a feature that appears almost ubiquitously in the continental crust. Transverse isotropy is readily found in middle and lower crustal settings and is often explained by lateral crustal flow and the development of layering. In particular, grainscale ductile deformation processes in the middle and lower crust develop CPO, which can strongly influence seismic properties. The intrinsic velocity and anisotropy of rock-forming minerals need also to be considered in the upper crust, although the contribution of fractured media is particularly relevant to the seismic properties in this depth interval. Seismic anisotropy in the upper crust has been linked to the regional stress field; fracture networks will tend to develop parallel to maximum stress axes. The importance of cracked and fractured media at deeper crustal conditions is uncertain, although KTB and Kola deep drilling projects indicate that cracked and fluid-bearing rocks exist at depths down to 9 to 12 km, respectively.

Interpretation of seismic data is generally based on mineral and rock physics, which constitute laboratory measurements on minerals and rocks at appropriate pressure and temperature conditions and predictive modeling schemes that takes into account the mineral composition, CPO, and microstructural features (e.g., distribution and geometric arrangement of crystals and cracked/fractured media). In this review we have discussed the predictive modeling of elastic and seismic properties, with a focus on the continental crust. Elastic constant data are paramount for predicting the seismic properties of the crust, and such data now exist for a large portion of the commonly occurring rock-forming minerals in the continental crust. Much of these data are, however, limited to measurements made at room conditions; high-temperature and high-pressure data are currently completely lacking for a number of important crustal minerals, including feldspars, amphiboles, mica, and many accessory minerals. High-temperature and high-pressure data exist mainly for minerals that also occur extensively in the uppermost mantle, such as olivine, pyroxene, and garnet. The application of ab initio first-principles methods has provided new determinations of the

single-crystal elastic constants of minerals found in the crust with complex structures such as clay minerals, chlorite, talc, antigorite, pyroxenes, and feldspars. Further contributions of ab initio first-principles methods to the elastic constants of crustal minerals at temperature and pressure are encouraged.

Several ways have been developed for calculating seismic velocities in anisotropic media. Fundamentally, all models consider the modal mineral composition and the CPO of the constituent minerals. These models are widely accepted to yield comparable results to laboratory measurements. More advanced models can be used to consider microstructural elements, such as the spatial distribution of minerals and their shape-preferred orientation, as well as the volume and orientation of cracks and fractures. A key challenge for the seismological, geodynamic, microstructure, and rock physics communities will be better separation of intrinsic seismic anisotropy related to the elastic constants of minerals, from apparent seismic properties arising from other sources (layering, cracks and fractures, fluids, and melt). This is an important challenge because seismic properties and anisotropy reveal unique information on geodynamic processes. The inability to separate intrinsic from apparent seismic properties therefore limits our insight into structural, compositional, and mass transfer processes in the Earth.

Future research may target some of the following aspects, which integrate mineral and rock physics, with disciplines of seismology and geodynamics:

1. Additional measurements of elastic constants for crustal mineral at high pressure and temperature, to obtain derivatives, particularly for minerals such as feldspars, micas, and amphiboles (as well as many other phases). Furthermore, it would be of interest to conduct measurements at simultaneous pressure and temperature to determine dC/dP derivatives, dC/dT derivatives, and cross derivatives (dC/dTdP). Even in the well-studied case of α-β quartz transition, there is only a complete sequence of measurements as a function of temperature at room pressure. Room temperature as a function of pressure to 10 GPa in the α-quartz field exists; however, these data are not relevant to in situ conditions in the crust. There is no data on β-quartz structure at pressure and temperature conditions, and no equation of state (EOS) for correct density estimates, and no data on elastic properties at pressure and temperature. There is good data on the α-β transition as a function of pressure and temperature from experimental petrology.
2. Improving the identification of intrinsic (crystal) versus extrinsic (i.e., cracks, layering, and faults) seismic anisotropy at depth, at different length and time scales. This seems like a challenge for collaborative efforts in fields of seismology, geodynamics, microstructures, and mineral physics.
3. Developing a better understanding of anelasticity in rock physics models and relationship to elastic anisotropy. Models should be developed to integrate anelasticity and elasticity, including their anisotropies.
4. Developing the link between thermodynamic equilibrium models [*Connolly and Petrini*, 2002; *Abers and Hacker*, 2016] and crystal tensor physical properties via, for example, atomic modeling codes.
5. Further development of measurement of spherical samples with simultaneous V_p and V_{s1}, at least, or preferentially both V_{s1} and V_{s2} that would greatly improve accuracy of elastic tensors of rocks and characterize the anisotropy of crack closure and role of fluid pressure. For spherical measurement setups [i.e., *Pros et al*., 1998, 2003], there is still only a limited range in applied pressure and no temperature. For a recent multimethod approach, see *Vasin et al*. [2017], which combines neutron and X-ray imaging, effective medium models, and laboratory measurements.

Glossary

Asymptotic expansion homogenization (AEH): Structure-based model that takes into account elastic interactions of neighboring mineral grains in a heterogeneous material. The method provides the possibility to macroscopically evaluate the effect of heterogeneous grain distributions in the medium. The benefit of the method is the possibility to use microphotographs and electron backscatter images that contain information both on the crystallographic preferred orientation of minerals and the microstructure.

Azimuthal seismic anisotropy: Directional dependence of seismic wave speed as a function of azimuth.

Crystallographic preferred orientation (CPO): The preferred orientation of crystallographic axes or poles to crystallographic planes, for a specified mineral (i.e., crystals are not randomly distributed); in this work CPO is used synonymously with lattice preferred orientation (LPO), but we recommend the term CPO as lattice of

LPO is a mathematical concept that describes a repeating arrangement of points, whereas we are defining the orientation of real crystals in this context, that has a much more complex motif than a lattice.

Differential effective medium (DEM): Effective medium model that considers two-phase materials, whose composite elastic properties are estimated by incremental addition of one phase (inclusion phase) into the second phase (matrix or background phase). The starting condition is a pure matrix medium, wherein inclusions of the second phase are added. A special property of the DEM is that inclusions are considered noninteracting (or isolated from each other).

Effective medium theory: Prediction of effective elastic moduli (or effective seismic velocities) in a composite material, using an analytical or theoretical solution. The most general analytical solution need to take into account volume fractions of the different phases in the composite, their elastic moduli (elastic constants), and the geometric and crystallographic information of the phases making up the composite.

Lattice-preferred orientation (LPO): synonymous with crystallographic preferred orientation (CPO); see crystallographic preferred orientation (CPO).

Microfabric: Follows the definition of *Paaschier and Trouw* [2005] and *Hobbs et al*. [1976], and describes, "the complete spatial and geometrical configuration of all those components that make up a rock". Emphasis is placed on the microscopic scale, generally observable with a petrographic microscope or smaller (i.e., Scanning Electron Microscope). Elements occurring on the nanometer scale are not included in the micro fabric. This definition includes, as an umbrella term, the concepts of texture or crystallographic preferred orientation (CPO) and microstructure. The latter term is used to describe mineral shape-preferred orientation (SPO), grain boundaries distribution of mineral grains, and deformation lamellae, on the scale of microns to centimetres.

Orientation distribution function (ODF): The function $f(\boldsymbol{g})$ that quantitatively describes the volume fraction of the sample within an orientation range $\boldsymbol{g} \pm \Delta\boldsymbol{g}$. The ODF can be described using spherical harmonics, as $f(\boldsymbol{g})$, may be expanded into a series function, which can be used to calculate ODF sections, pole figures, inverse pole figures, and aggregate anisotropic physical properties, such as elastic properties.

Pole Figure: Graphical representation of poles to crystallographic planes or crystallographic directions. The crystallographic data are shown with an equal area projection (Schmidt net) or equal angle projection (Wulff net) in sample coordinates.

Radial seismic anisotropy: Seismic anisotropy calculated from the horizontally polarized (*Vsh*) and vertically polarized (*Vsv*) shear waves. When $Vsh > Vsv$, the anisotropy is positive, whereas when $Vsv > Vsh$, the anisotropy is considered negative. A vertically transverse isotropic medium (VTI) usually shows positive radial anisotropy.

Reuss bound: The theoretical elastic or seismic velocity lower bound for an aggregate of minerals. Also known as the isostress bound, because this calculation considers all components in the medium to have equal stress, but strain varies throughout the medium.

Seismic anisotropy: Directional dependence of seismic velocity and polarization in a material. The *P* wave anisotropy is typically expressed as $AVp = (Vp_{max} - Vp_{min})/Vp_{mean}$, where Vp_{max} and Vp_{min} are the maximum and minimum seismic *P* wave velocities in the material, and Vp_{mean} is the average seismic *P* wave velocity in the material. Alternatively, seismic anisotropy can be calculated using the expression $200(Vp_{max}\text{-}Vp_{min})/(Vp_{max}+Vp_{min})$. The *S* wave anisotropy may be expressed in two ways. First, according to the difference between the fast and slow polarized shear waves, $Vs_1 - Vs_2$ (shear wave splitting). Secondly, the *S* wave anisotropy can be expressed as $AVs_{1,2} = (Vs_{1,2max} - Vs_{1,2min})/Vs_{1,2mean}$, where Vs_1 and Vs_2 are the fast and slow polarized shear waves. The maximum possible *AVs* is expressed by the greatest difference of the shear wave velocity, considering both Vs_1 and Vs_2. See also the glossary entry for seismic birefringence and shear wave splitting. A special case of radial shear wave anisotropy is defined by *S* waves with polarization in the horizontal plane (*Vsh*) and *S* waves polarized in the vertical plane (*Vsv*).

Shear wave splitting (seismic birefringence): The difference in velocity between the fast polarized and slow polarized shear waves in an anisotropic medium, defined as $dVs = Vs_1 - Vs_2$. Shear wave splitting can also be presented in terms of a delay time, which is the difference in arrival time between the of Vs_1 and Vs_2 at a seismic station; the delay time is expressed in seconds.

Self-consistent approximation (SCA): Theoretical estimates of elastic moduli for a composite material. The most general analytical solution needs to take into account volume fractions of the different phases in the composite, elastic moduli of each phase, and geometric and crystallographic information of each phase. These theoretical estimates may also be referred to as self-consistent schemes (SCS).

Shape preferred orientation (SPO): Term used to describe if grains comprising the microfabric has preferred shape, i.e., grains that have shape such as linear (prolate) or flattened (oblate) ellipsoids, and align along a specific structural element, for example, the foliation plane.

Texture: Term that is generally used in material sciences and structural geology, to describe the crystallographic preferred orientation (CPO) or its synonym lattice preferred orientation (LPO).

Transverse isotropic (TI) symmetry: A material with transverse isotropic symmetry has one unique axis, about which the seismic properties are symmetric and a plane of isotropy that is oriented normal to the symmetry axis. This symmetry is commonly assumed for the layering of the interior of the Earth with the symmetry axis oriented vertically (normal to the layering), which is known as vertical transverse isotropy (VTI); when the symmetry axis is horizontal the material shows horizontal transverse isotropy (HTI). The symmetry axis may not necessarily coincide with an axis that is vertical or horizontal, in which case it is dipping at some angle between the vertical and horizontal axis.

Voigt bound: The theoretical elastic or seismic velocity upper bound. Also known as the isostrain bound, because this calculation considers all components in the medium to have the strain, but stress varies throughout the medium.

Voigt-Reuss-Hill bound: Average arithmetic mean of the Voigt and Reuss bounds, introduced by *Hill* [1952], there is no theoretical justification for the average, but it is often close to experimental measurements as shown by Hill.

Acknowledgments
Daria Cyprych (Czaplinska) and Sandra Piazolo helped perform the EBSD measurements for sample COSC193, and Xin Zhong is thanked for allowing us to show results from the numerical modeling of dynamic wave propagation of the COSC193 sample (the results are based on the SEM-EBSD map in Figures 15 and 16). The EBSD work was made possible in part by a visiting fellowship to Macquarie University (Sydney, Australia). Data that are used and presented in this study can be obtained upon request from the corresponding author. BSGA thanks the Swedish Research Council for financial support, through a junior researcher grant (2012-4449). Walter Mooney kindly provided a copy of the high-resolution image shown in Figure 1 of this manuscript. We thank Haemyeong Jung, Sarah Brownlee, and an anonymous reviewer for thoughtful and constructive comments, which have greatly improved the manuscript.

References

Abers, G. A., and B. R. Hacker (2016), A MATLAB toolbox and Excel workbook for calculating the densities, seismic wave speeds, and major element composition of minerals and rocks at pressure and temperature, *Geochem. Geophys. Geosyst.*, *17*, 616–624, doi:10.1002/2015GC006171.

Abramson, E. H., J. M. Brown, L. J. Slutsky, and J. Zaug (1997), The elastic constants of San Carlos olivine to 17 GPa, *J. Geophys. Res.*, *102*, 12,253–12,263, doi:10.1029/97JB00682.

Aleksandrov, K. S., and L. A. Aizenberg (1967), Methods of calculating physical constants of polycrystallic materials, *Dokl. Akad. Nauk SSSR*, *167*, 1028.

Aleksandrov, K. S., and T. V. Ryzhova (1961), Elastic properties of rock forming minerals 2 layered silicates, *Bull. Acad. Sci. USSR Geophys. Sr.*, *11*, 871–875.

Aleksandrov, K. S., T. V. Ryzhova, and B. P. Belikov (1964), The elastic properties of pyroxenes, *Sov. Phys. – Crystallogr.*, *8*, 589–591.

Aleksandrov, K. S., U. V. Alchikov, B. P. Belikov, B. I. Zaslavskii, and A. I. Krupnyi (1974), Velocities of elastic waves in minerals at atmospheric pressure and increasing precision of elastic constants by means of EVM [in Russian], *Izv. Acad. Sci. USSR, Geo. Ser.*, *10*, 15–24.

Almqvist, B. S. G., D. Mainprice, C. Madonna, L. Burlini, and A. M. Hirt (2011), Application of differential effective medium, magnetic pore fabric analysis, and X-ray microtomography to calculate elastic properties of porous and anisotropic rock aggregates, *J. Geophys. Res.*, *116*, B01204, doi:10.1029/2010JB007750.

Almqvist, B. S. G., A. M. Hirt, M. Herwegh, A. Ebert, J. M. Walter, B. Leiss, and L. Burlini (2013), Seismic anisotropy in the Morcles nappe shear zone: Implication for seismic imaging of crustal scale shear zones, *Tectonophysics*, *603*, 162–178.

AlpArray Seismic Network (2015), AlpArray Seismic Network (AASN) temporary component, AlpArray Working Group, Other/Seismic Network, doi:10.12686/alparray/z3_2015.

Anderson, D. L., B. Minster, and D. Cole (1974), The effect of oriented cracks on seismic velocities, *J. Geophys. Res.*, *79*, 4011–4015, doi:10.1029/JB079i026p04011.

Arntsen, B. (2007), Validity of the long-wave approximation in peridically layered media, *Geophys. Prospect.*, *55*, 49–56.

BABEL Working Group (1990), Evidence for early Proterozoic plate tectonics from seismic reflection profiles in the Baltic shield, *Nature*, *348*, 34–38.

BABEL Working Group (1993), Deep seismic reflection/refraction interpretation of crustal structure along BABEL profiles A and B in the southern Baltic Sea, *Geophys. J. Int.*, *112*, 325–343.

Babuska, V., and M. Cara (1991), *Seismic Anisotropy in the Earth*, pp. 217, Kluwer Acad., Netherlands.

Babuska, V., J. Fiala, M. Kumazawa, I. Ohno, and Y. Sumino (1978), Elastic properties of garnet solid-solutions series, *Phys. Earth Planet. Int.*, *16*, 157–176.

Backus, G. E. (1962), Long-wave elastic anistropy produced by horizontal layering, *J. Geophys. Res.*, *67*, 4427–4440, doi:10.1029/JZ067i011p04427.

Baker, D. W., and N. L. Carter (1972), Seismic velocity anisotropy calculated for ultramafic minerals and aggregates, in *Flow and Fracture of Rocks*, *Geophys. Monogr. Ser.*, vol. 16, edited by H. C. Heard et al., pp. 157–166, AGU, Washington, D. C.

Barberini, V., L. Burlini, and A. Zappone (2007), Elastic properties, fabric and seismic anisotropy of amphibolites and their contribution to the lower crust reflectivity, *Tectonophysics*, *445*, 227–244.

Barnes, A. E., and T. J. Reston (1992), A study of two mid-crustal bright spots from southeast Georgia (USA), *Geophys. J. Int.*, *108*, 683–691.

Barruol, G., and H. Kern (1996), Seismic anisotropy and shear-wave splitting in lower-crustal and upper-mantle rocks from the Ivrea Zone—Experimental and calculated data, *Phys. Earth Planet. Inter.*, *95*, 175–194.
Barruol, G., and D. Mainprice (1993), 3-D seismic velocities calculated from lattice-preferred orientation and reflectivity of a lower crustal section: Examples of the Val Sesia section (Ivrea zone, northern Italy), *Geophys. J. Int.*, *115*, 1169–1188.
Bascou, J., G. Barruol, A. Vauchez, D. Mainprice, and M. Egydio-Silva (2001), EBSD-measured lattice-preferred orientations and seismic properties of eclogites, *Tectonophysics*, *342*, 61–80.
Bass, J. D. (1995), Elasticity of minerals, glasses, and melts, in *Minerals and Crystallography: A Handbook of Physical Constants*, edited by T. J. Ahrens, pp. 45–63, AGU, Washington, D. C.
Bass, J. D., and D. J. Weidner (1984), Elasticity of single-crystal orthoferrosilite, *J. Geophys. Res.*, *89*, 4359–4371, doi:10.1029/JB089iB06p04359.
Bass, J. D., and J. S. Zhang (2015), Theory and practice: Techniques for measuring high-P–T elasticity, in *Treatise on Geophysics*, vol. 2, 2nd ed., edited by G. Schubert, pp. 293–312, Elsevier, Oxford.
Bell, R. O., and G. Rupprecht (1963), Elastic constants of strontium titanite, *Phys. Rev.*, *129*, 90–94.
Ben Ismaïl, W., and D. Mainprice (1998), An olivine fabric database: An overview of upper mantle fabrics and seismic anisotropy, *Tectonophysics*, *296*, 145–157.
Berge, P. A., J. G. Berryman, and B. P. Bonner (1993), Influence of microstructure on rock elastic properties, *Geophys. Res. Lett.*, *20*, 2619–2622, doi:10.1029/93GL03131.
Berryman, J. G. (1995), Mixture theories for rock properties, in *Rock Physics and Phase Relations: A Handbook of Physical Constants*, edited by T. J. Ahrens, pp. 205–228, AGU, Washington, D. C.
Bezacier, L., B. Reynard, J. D. Bass, J. Wang, and D. Mainprice (2010), Elasticity of glaucophane, seismic velocities and anisotropy of the subducted oceanic crust, *Tectonophysics*, *494*, 201–210.
Bhagat, S. S., J. D. Bass, and J. R. Smyth (1992), Single-crystal elastic properties of omphacite-C2/c by Brillouin spectroscopy, *J. Geophys. Res.*, *97*, 6843–6848.
Bina, C. R., and G. R. Helffrich (1992), Calculation of elastic properties from thermodynamic equation of state principles, *Annu. Rev. Earth Planet. Sci.*, *20*, 257–552.
Biot, M. A. (1962), Generalized theory of acoustic propagation in porous media, *J. Acoust. Soc. Am.*, *34*, 1254–1264.
Birch, F. (1960a), The velocity of compressional waves in rock to 10 kilobars: Part 1, *J. Geophys. Res.*, *65*, 1083–1102, doi:10.1029/JZ065i004p01083.
Birch, F. (1960b), Elastic constants of rutile—A correction to a paper by R. K. Verma, "Elasticity of some high-density crystals", *J. Geophys. Res.*, *65*, 3855–3856, doi:10.1029/JZ065i011p03855.
Birch, F. (1961), The velocity of compressional waves in rock to 10 kilobars: Part 2, *J. Geophys. Res.*, *66*, 2199–2224, doi:10.1029/JZ066i007p02199.
Birch, F. (1972), Numerical experiments on the velocity in aggregates of olivine, *J. Geophys. Res.*, *77*, 6385–6391, doi:10.1029/JB077i032p06385.
Bristow, J. R. (1960), Microcracks and the static and dynamic elastic constants of annealed and heavily cold-worked metals, *Br. J. Appl. Phys.*, *11*, 81–85.
Brown, J. M. (2015), Determination of Hashin-Shtrikman bounds on the isotropic effective elastic moduli of polycrystals of any symmetry, *Comput. Geosci.*, *80*, 95–99.
Brown, J. M., and E. H. Abramson (2016), Elasticity of calcium and calcium-sodium amphiboles, *Phys. Earth Planet. Inter.*, *261*, 161–171.
Brown, J. M., L. J. Slutsky, K. A. Nelson, and L.-T. Cheng (1989), Single-crystal elastic constants for San Carlos peridot: An application of impulsive stimulated scattering, *J. Geophys. Res.*, *94*, 9485–9492, doi:10.1029/JB094iB07p09485.
Brown, J. M., E. H. Abramson, and R. L. Ross (2006), Triclinic elastic constants for low albite, *Phys. Chem. Miner.*, *33*, 256–265.
Brown, J. M., R. J. Angel, and N. L. Ross (2016), Elasticity of plagioclase feldspars, *J. Geophys. Res. Solid Earth*, *121*, 663–675, doi:10.1002/2015JB012736.
Brown, L. D., M. Barazangi, S. Kaufman, and J. E. Oliver (1986), The first decade of COCORP: 1974–1984, in *Reflection Seismology: A Global Perspective*, edited by M. Barazanghi and L. D. Brown, *AGU Geodyn. Ser.*, pp. 107–120.
Brown, L. D., W. Zhao, K. D. Nelson, M. Hauck, D. Alsdorf, A. Ross, M. Cogan, M. Clark, X. Liu, and J. Che (1996), Bright spots, structure, and magmatism in Southern Tibet from INDEPTH seismic reflection profiling, *Science*, *274*, 1688–1690.
Brownlee, S. J., B. R. Hacker, M. Salisbury, G. Seward, T. A. Little, S. L. Baldwin, and G. A. Abers (2011), Predicted velocity and density structure of the exhuming Papua New Guinea ultrahigh-pressure terrane, *J. Geophys. Res.*, *116*, B08206, doi:10.1029/2011JB008195.
Bruner, W. M. (1976), Comment on "Seismic velocities in dry and saturated cracked solids", *J. Geophys. Res.*, *81*, 2573–2576, doi:10.1029/JB081i014p02573.
Budiansky, B. (1965), On the elastic moduli of some heterogeneous materials, *J. Mech. Phys. Solids*, *13*, 223–227.
Budiansky, B., and R. J. O'Connell (1976), Elastic moduli of a cracked solid, *Int. J. Solids Structures*, *12*, 81–97.
Burlini, L., and D. M. Fountain (1993), Seismic anisotropy of metapelites from the Ivrea-Verbano zone and Serie dei Laghi (northern Italy), *Phys. Earth Planet. Inter.*, *78*, 301–317.
Burlini, L., and K. Kunze (2000), Fabric and seismic properties of Carrara marble mylonite, *Phys. Chem. Earth*, *25*, 133–139.
Burlini, L., D. Marquer, N. Challandes, S. Mazzola, and N. Zangarini (1998), Seismic properties of highly strained marbles from the Splügenpass, central Alps, *J. Struct. Geol.*, *20*, 277–292.
Cao, Y., H. Jung, and S. Song (2013), Petro-fabrics and seismic properties of blueschist and eclogite in the North Qilian suture zone, NW China: Implications for the low-velocity upper layer in subducting slab, trench-parallel seismic anisotropy and eclogite detectability in the subduction zone, *J. Geophys. Res. Solid Earth*, *118*, 3037–3058, doi:10.1002/jgrb.50212.
Carcione, J. M., D. Kosloff, and A. Behle (1991), Long-wave anisotropy in stratified media: A numerical test, *Geophysics*, *56*, 245–254.
Carpenter, M. A. (2006), Elastic properties of minerals and the influence of phase transitions, *Am. Mineral.*, *91*, 229–246.
Carpenter, M. A., E. K. H. Salje, A. Graeme-Barber, B. Wrucki, M. T. Dove, and K. S. Knight (1998), Calibration of excess thermodynamic properties and elastic constant variations associated with the alpha-beta phase transition in quartz, *Am. Mineral.*, *83*, 2–22.
Chai, M., J. M. Brown, and L. J. Slutsky (1997a), The elastic constants of an aluminous orthopyroxene to 12.5 GPa, *J. Geophys. Res.*, *102*, 14,779–14,785, doi:10.1029/97JB00893.
Chai, M., J. M. Brown, and L. J. Slutsky (1997b), The elastic constants of a pyrope-grossular-almandine garnet to 20 GPa, *Geophys. Res. Lett.*, *24*, 523–526, doi:10.1029/97GL00371.
Chen, C.-C., C.-C. Lin, L.-G. Liu, V. Sinogeikin, and J. D. Bass (2001), Elasticity of single-crystal calcite and rhodochrosite by Brillouin spectroscopy, *Am. Mineral.*, *86*, 1525–1529.

Chen, L., C. Cheng, and Z. Wei (2009), Seismic evidence for significant lateral variations in lithospheric thickness beneath the central and western North China Craton, *Earth Planet. Sci. Lett.*, *286*, 171–183.
Cheng, C., L. Chen, H. Yao, M. Jiang, and B. Wang (2013), Distinct variations of crustal shear wave velocity structure and radial anisotropy beneath the North China Craton and tectonic implications, *Gondwana Res.*, *23*, 25–38.
Chheda, T. D., M. Mookherjee, D. Mainprice, A. M. dos Santos, J. J. Molaison, J. Chantel, G. Manthilake, and W. A. Bassett (2014), Structure and elasticity of phlogopite under compression: Geophysical implications, *Phys. Earth Planet. Inter.*, *233*, 1–12.
Cholach, P. Y., and D. R. Schmitt (2006), Intrinsic elasticity of a textured transversely isotropic muscovite aggregate: Comparisons to the seismic anisotropy of schists and shales, *J. Geophys. Res.*, *111*, B09410, doi:10.1029/2005JB004158.
Christensen, N. I. (1965), Compressional wave velocities in metamorphic rocks at pressure to 10 kilobars, *J. Geophys. Res.*, *70*, 6147–6164, doi:10.1029/JZ070i024p06147.
Christensen, N. I. (1971), Shear wave propagation in rocks, *Nature*, *229*, 549–550.
Christensen, N. I. (1974), Compressional wave velocities in possible mantle rocks to pressures of 30 kilobars, *J. Geophys. Res.*, *79*, 407–412, doi:10.1029/JB079i002p00407.
Christensen, N. I. (1979), Compressional wave velocities in rocks at high temperatures and pressures, critical thermal gradients, and crustal low-velocity zones, *J. Geophys. Res.*, *84*, 6849–6857, doi:10.1029/JB084iB12p06849.
Christensen, N. I. (1984), Pore pressure and oceanic crustal seismic structure, *Geophys. J. R. Astron. Soc.*, *79*, 411–423.
Christensen, N. I. (1996), Poisson's ratio and crustal seismology, *J. Geophys. Res.*, *101*, 3139–3156, doi:10.1029/95JB03446.
Christensen, N. I., and W. D. Mooney (1995), Seismic velocity structure and composition of the continental crust: A global view, *J. Geophys. Res.*, *100*, 9761–9788, doi:10.1029/95JB00259.
Christoffel, E. B. (1877), Über die Fortpflanzung von Stössen durch elastiche feste Körper, *Ann. Mat. Pura Appl.*, *8*, 193–243.
Cirrincione, R., E. Fazio, R. Heilbronner, H. Kern, K. Mengel, G. Ortolano, A. Pezzino, and R. Punturo (2010), Microstructure and elastic anisotropy of naturally deformed leucogneiss from a shear zone in Montalto (southern Calabria, Italy), *Geol. Soc. London, Spec. Publ.*, *332*, 49–68.
Clowes, R. M., M. Brandon, A. Green, C. Yorath, and A. Sutherland-Brown (1987), LITHOPROBE—Southern Vancouver Island: Cenozoic subduction complex imaged by deep seismic reflections, *Can. J. Earth Sci.*, *24*, 31–51.
Clowes, R. M., F. A. Cook, and J. N. Ludden (1998), Lithoprobe leads to new perspective on continental evolution, *GSA Today*, *8*, 1–7.
Coe, R. S., and M. S. Paterson (1969), The α-β inversion in quartz: A coherent phase transition under nonhydrostatic stress, *J. Geophys. Res.*, *74*, 4921–4948, doi:10.1029/JB074i020p04921.
Collins, M. D., and J. M. Brown (1998), Elasticity of an upper mantle clinopyroxene, *Phys. Chem. Miner.*, *26*, 7–13.
Connolly, J. A. D., and A. Khan (2016), Uncertainty of mantle geophysical properties computed from phase equilibrium models, *Geophys. Res. Lett.*, *43*, 5026–5034, doi:10.1002/2016GL068239.
Connolly, J. A. D., and K. Petrini (2002), An automated strategy for calculation of phase diagram sections and retrieval of rock properties as a function of physical conditions, *J. Metamorph. Petrol.*, *20*, 697–708.
Cook, A., S. Vel, S. E. Johnson, C. Gerbi, and W. J. Song (2013), Elastic and seismic properties (ESP) toolbox (beta version). [Available at http://umaine.edu/mecheng/faculty-and-staff/senthil-vel/software/ESP-Toolbox.]
Cordier, P., D. Mainprice, and J. L. Mosenfelder (2004), Mechanical instability near the stishovite-$CaCl_2$ phase transition: Implications for crystal preferred orientations and seismic properties, *Eur. J. Mineral.*, *16*, 387–399.
Cossette, E., D. Schneider, P. Audet, B. Grasemann, and G. Habler (2015a), Seismic properties and mineral crystallographic preferred orientations from EBSD data: Results from a crustal-scale detachment system, Aegean region, *Tectonophysics*, *651–652*, 66–78.
Cossette, E., P. Audet, D. Schneider, and B. Grasemann (2015b), Structure and anisotropy of the crust in the Cyclades, Greece, using receiver functions constrained by in situ rock textural data, *J. Geophys. Res. Solid Earth*, *121*, 2661–2678, doi:10.1002/2015JB012460.
Crampin, S., Y. Gao, and J. Bukits (2015), A review of retrospective stress-forecasts of earthquakes and eruptions, *Phys. Earth Planet. Inter.*, *245*, 76–87.
Crosson, R. S., and J.-W. Lin (1971), Voigt and Reuss prediction of anisotropic elasticity of dunite, *J. Geophys. Res.*, *76*, 570–578, doi:10.1029/JB076i002p00570.
Dandekar, D. P. (1968), Pressure dependence of the elastic constants of calcite, *Phys. Rev.*, *172*, 873–877.
Darot, M., and T. Reusché (2000), Effect of pore and confining pressures on V_P in thermally pre-cracked granites, *Geophys. Res. Lett.*, *27*, 1057–1060, doi:10.1029/1999GL008414.
Delle Piane, C., B. S. G. Almqvist, C. M. MacRae, A. Torpy, A. J. Mory, and D. N. Dewhurst (2015), Texture and diagenesis of Ordovician shale from the Canning Basin, Western Australia: Implications for elastic anisotropy and geomechanical properties, *Mar. Pet. Geol.*, *59*, 56–71.
Doraiswami, M. S. (1947), Elastic constants of magnetite, pyrite and chromite, *Proc. Math. Sci.*, *25*, 413–416.
Duffy, T. S., and M. T. Vaughan (1988), Elasticity of enstatite and its relationship to crystal structure, *J. Geophys. Res.*, *93*, 383–391, doi:10.1029/JB093iB01p00383.
Eberhart-Phillips, D., D. H. Han, and M. D. Zoback (1989), Empirical relationships among seismic velocity, effective pressure, porosity, and clay content in sandstone, *Geophysics*, *54*, 82–89.
ECORS Pyrenees Team (1988), The ECORS deep reflection seismic survey across the Pyrenees, *Nature*, *331*, 508–511.
Emmermann, R., and J. Lauterjung (1997), The German Continental Deep Drilling Program KTB: Overview and major results, *J. Geophys. Res.*, *102*, 18,179–18,201, doi:10.1029/96JB03945.
Endrun, B., S. Lebedev, T. Meier, C. Tirel, and W. Friederich (2011), Complex layered deformation within the Aegean crust and mantle revealed by seismic anisotropy, *Nat. Geosci.*, *4*, 203–207.
Erdman, M. E., B. R. Hacker, G. Zandt, and G. Seward (2013), Seismic anisotropy of the crust: Electron-backscatter diffraction measurements from the Basin and Range, *Geophys. J. Int.*, doi:10.1093/gji/ggt287.
Eshelby, J. S. (1957), The determination of the elastic field of an ellipsoidal inclusion, and related problems, *Proc. R. Soc. London, Ser. A*, *241*, 376–396.
Faccenda, M., and F. A. Capitanio (2012), Development of mantle seismic anisotropy during subduction-induced 3D flow, *Geophys. Res. Lett.*, *39*, L11305, doi:10.1029/2012GL051988.
Fedorov, E. S. (1892), Eine neue Methode der optischen untersuchung von Krystallplatten in parallelem Lichte, *Tschermak's Mineralgische und Petrographische Mittheilungen*, *12*, 505–509.
Fedorov, E. S. (1894), Universal- (Theodolith-) Methode in der Mineralogie und Petrographie, *Zeitschrift für Kristallographie und Mineralogie*, *22*, 229–268.
Fei, Y. (1995), Thermal expansion, in *Minerals and Crystallography: A Handbook of Physical Constants*, edited by T. J. Ahrens, pp. 29–44, AGU, Washington, D. C.

Feinberg, J. M., H.-R. Wenk, G. R. Scott, and P. R. Renne (2006), Preferred orientation and anisotropy of seismic and magnetic properties in gabbronorites from the Bushveld layered intrusion, *Tectonophysics*, *420*, 345–356.
Fichtner, A., B. L. N. Kennett, and J. Trampert (2013), Separating intrinsic and apparent anisotropy, *Phys. Earth Planet. Inter.*, *219*, 11–20.
Firestone, F. A., and J. R. Fredrick (1946), Refinements in the supersonic reflectoscopy. Polarized sound, *J. Acoustical Soc. Am.*, *18*, 200–211.
Fouch, M. J., and S. Rondenay (2006), Seismic anisotropy beneath stable continental interiors, *Phys. Earth Planet. Inter.*, *158*, 292–320.
Fountain, D. M. (1976), The Ivera-Verbano and Strona-Ceneri zones, northern Italy: A cross-section of the continental crust—New evidence from seismic velocities of rock samples, *Tectonophysics*, *33*, 145–165.
Frehner, M., S. M. Schmalholz, E. H. Saenger, and H. Steeb (2008), Comparison of finite difference and finite element methods for simulating two-dimensional scattering of elastic waves, *Phys. Earth Planet. Inter.*, *171*, 112–121.
Frisillo, A. L., and G. R. Barsch (1972), Measurements of single-crystal elastic constants of bronzite as a function of pressure and temperature, *J. Geophys. Res.*, *77*, 6360–6384, doi:10.1029/JB077i032p06360.
Fu, Y. V., Y. Gao, A. Li, L. Lu, Y. Shi, and Y. Zhang (2016), The anisotropic structure in the crust in the northern part of North China from ambient seismic noise tomography, *Geophys. J. Int.*, *204*, 1649–1661.
Gassmann, F. (1951), Uber die elastizitat poroser medien, *Vierteljahrsschr. Naturforsch. Ges.*, *96*, 1–23.
Grab, M., B. Quintal, E. Caspari, H. Maurer, and S. Greenhalgh (2017), Numerical modeling of fluid effects on seismic properties of fractured magmatic geothermal reservoirs, *Solid Earth*, *8*, 255–279.
Graham, E. K., and G. R. Barsch (1969), Elastic constants of single-crystal forsterite as a function of temperature and pressure, *J. Geophys. Res.*, *74*, 5949–5960, doi:10.1029/JB074i025p05949.
Graham, E. K., J. A. Schwab, S. M. Sopkin, and H. Takei (1988), The pressure and temperature dependence of the elastic properties of single-crystal fayalite Fe_2SiO_4, *Phys. Chem. Miner.*, *16*, 186–198.
Grechka, V., and M. Kachanov (2006), Seismic characterization of multiple fracture sets: Does orthotropy suffice?, *Geophysics*, *71*(3), D93–D105.
Guéguen, Y., and V. Palciauskas (1994), *Introduction to the Physics of Rocks*, pp. 304, Princeton Univ. Press, New Jersey.
Gwanmesia, G. D., L. Wang, R. Triplett, and R. C. Liebermann (2009), Pressure and temperature dependence of the elasticity of pyrope-majorite [Py60Mj40 and Py50Mj50] garnets solid solution measured by ultrasonic interferometry technique, *Phys. Earth Planet. Int.*, *174*, 105–112.
Hacker, B. R., and G. A. Abers (2004), Subduction Factory 3: An Excel worksheet and macro for calculating the densities, seismic wave speeds, and H_2O contents of minerals and rocks at pressure and temperature, *Geochem. Geophys. Geosyst.*, *5*, Q01005, doi:10.1029/2003GC000614.
Hacker, B. R., M. H. Ritzwoller, and J. Xie (2014), Partially melted, mica-bearing crust in central Tibet, *Tectonics*, *33*, 1408–1424, doi:10.1002/2014TC003545.
Hacker, B. R., P. B. Keleman, and M. D. Behn (2015), Continental lower crust, *Annu. Rev. Earth Planet. Sci.*, *43*, 167–205.
Hansen, L. N., C. Qi, and J. M. Warren (2016), Olivine anisotropy suggests Gutenberg discontinuity is not the base of the lithosphere, *Proc. Natl. Acad. Sci. U.S.A.*, *113*, 10,503–10,506.
Haussühl, S. (1960), Thermo-elastische Konstanten der Alkalihalogenide vom NaCl-Typ, *Zeitschrift für Physik*, *159*, 223–229.
Haussühl, S. (1965), Elastische und thermoelastische Eigenschaften von CaSO4.2H2O (Gips), *Zeitschrift für Kristallographie*, doi:10.1515/zkri-1965-1-628.
Haussühl, S. (1993), Thermoelastic properties of beryl, topaz, diaspore, sanidine and periclase, *Z. Kristallogr.*, *204*, 67–76.
Hearmon, R. F. S. (1979), The elastic constants of crystals and other anisotropic materials, in *Landolt-Börnstein Tables, Group III*, vol. 11, edited by K. H. Hellwege and A. M. Hellwege, pp. 1–244, Springer, Berlin.
Hearmon, R. F. S. (1984), The elastic constants of crystals and other anisotropic materials, in *Landolt-Börnstein Tables, Group III*, vol. 18, edited by K. H. Hellwege and A. M. Hellwege, pp. 1–154, Springer, Berlin.
Helbig, K., and M. Schoenberg (1987), Anomalous polarizations elastic waves in transversely isotropic media, *J. Acoust. Soc. Am.*, *81*, 1235–1245.
Henyey, F. S., and N. Pomphrey (1982), Self-consistent elastic moduli of a cracked solid, *Geophys. Res. Lett.*, *9*, 903–906, doi:10.1029/GL009i008p00903.
Hess, H. H. (1964), Seismic anisotropy of the uppermost mantle under oceans, *Nature*, *203*, 629–631.
Heyliger, P., H. Ledbetter, and S. Kim (2003), Elastic constants of natural quartz, *J. Acoust. Soc. Am.*, *114*, 644–650.
Hielscher, R., and H. Schaeben (2008), A novel pole figure inversion method: Specification of the MTEX algorithm, *J. Appl. Crystallogr.*, *41*, 1024–1037.
Hill, R. (1952), The elastic behaviour of a crystalline aggregate, *Proc. Phys. Soc., London, Sect. A*, *A65*, 349–354.
Hill, R. (1965), A self-consistent mechanics of composite materials, *J. Mech. Phys. Solids*, *13*, 213–222.
Hirn, A., B. Damotte, G. Torreilles, and E. C. O. R. S. Scientific Party (1987), Crustal refection seismic: The contributions of oblique, low frequency and shear wave illuminations, *Geophys. J. R. Astron. Soc.*, *89*, 287–296.
Hood, J. A. (1991), A simple method for decomposing fracture induced anisotropy, *Geophysics*, *56*, 1275–1279.
Hornby, B. E. (1998), Experimental laboratory determination of the dynamic elastic properties of wet, drained shales, *J. Geophys. Res.*, *103*, 29,945–29,964.
Hornby, B. E., L. M. Schwartz, and J. A. Hudson (1994), Anisotropic effective medium modelling of the elastic properties of shales, *Geophysics*, *59*, 1570–1583.
Hsu, C.-J., and M. Schoenberg (1993), Elastic waves through a simulated fractured medium, *Geophysics*, *58*, 964–977.
Huang, T. Y., Y. Gung, B.-Y. Kuo, L.-Y. Chiao, and Y.-N. Chen (2015), Layered deformation in the Taiwan orogen, *Science*, *349*, 720–723.
Hudson, J. A. (1980), A higher order approximation to the wave propagation constants for a cracked solid, *Geophys. J. Int.*, *87*, 265–274.
Huenges, E., J. Erzinger, J. Kuick, B. Engeser, and W. Kessels (1997), The permeable crust: Geohydraulic properties down to 9101 m depth, *J. Geophys. Res.*, *102*, 18,255–18,265, doi:10.1029/96JB03442.
Humbert, P., and F. Plique (1972), Propriétés élastiques de carbonates rhombohédriques monocristallines: Calcite, magnésite, dolomie, *C. R. Acad. Sci. Paris, Ser. B*, *275*, 391–394.
Hurich, C. A., and S. B. Smithson (1987), Compositional variation and the origin of deep crustal reflections, *Earth Planet. Sci. Lett.*, *85*, 416–426.
Inbal, A., J. P. Ampuero, and R. W. Clayton (2016), Localized seismic deformation in the upper mantle revealed by dense seismic arrays, *Science*, *354*, 88–92.
Isaak, D. G. (1992), High-temperature elasticity of iron-bearing olivines, *J. Geophys. Res.*, *97*(B2), 1871–1885, doi:10.1029/91JB02675.
Isaak, D. G. (2001), Elastic properties of minerals and planetary objects, in *Handbook of Elastic Properties of Solids, Liquids, and Gases, Elastic Prop. Solids: Biol. Org. Mater., Earth Mar. Sci.*, vol. 3, edited by M. Levy, H. Bass, and R. Stern, pp. 325–376, Academic Press, San Diego, Calif.

Isaak, D. G., and I. Ohno (2003), Elastic constants of chrome-diopside: Application of resonant ultrasound spectroscopy to monoclinic single-crystal, *Phys. Chem. Miner.*, *30*, 430–439.
Isaak, D. G., O. L. Anderson, T. Goto, and I. Suzuki (1989), Elasticity of single-crystal forsterite measured to 1700 K, *J. Geophys. Res.*, *94*, 5895–5906.
Isaak, D. G., E. K. Graham, J. D. Bass, and H. Wang (1993), The elastic properties of single-crystal fayalite as determined by dynamical measurement techniques, *Pure Appl. Geophys.*, *141*, 393–414.
Isaak, D. G., J. D. Carnes, O. L. Anderson, H. Cynn, and E. Hake (1998), Elasticity of TiO_2 rutile to 1800 K, *Phys. Chem. Miner.*, *26*, 31–43.
Isaak, D. G., I. Ohno, and P. C. Lee (2006), The elastic constants of monoclinic single-crystal chrome-diopside to 1300 K, *Phys. Chem. Miner.*, *32*, 691–699.
Isida, S., M. Suzuki, S. Todo, N. Môri, and K. Siratori (1996), Pressure effect on the elastic constants of magnetite, *Physica B*, *219–220*, 638–640.
Jackson, J. M., S. V. Sinogeikin, and J. D. Bass (1999), Elasticity of $MgSiO_3$ orthoenstatite, *Am. Mineral.*, *84*, 677–680.
Jackson, J. M., S. V. Sinogeikin, and J. D. Bass (2007), Sound velocities and single-crystal elasticity of orthoenstatite to 1073 K at ambient pressure, *Phys. Earth Planet. Inter.*, *161*, 1–12.
Jagoutz, O., and M. D. Behn (2013), Foundering of lower island-arc crust as an explanation for the origin of the continental Moho, *Nature*, *504*, 131–134, doi:10.1038/nature12758.
Ji, S., and D. Mainprice (1988), Natural deformation fabrics of plagioclase: Implications for slip systems and seismic anisotropy, *Tectonophysics*, *147*, 145–163.
Ji, S., M. Salisbury, and S. Hanmer (1993), Petrofabric, P-wave anisotropy and seismic reflectivity of high-grade tectonites, *Tectonophysics*, *222*, 195–226.
Ji, S., K. Saruwatari, D. Mainprice, R. Wirth, Z. Xu, and B. Xia (2003), Microstructure, petrofabrics and seismic properties of ultra high-pressure eclogites from Sulu region, China: Implications for rheology of subducted continental crust and origin of mantle reflections, *Tectonophysics*, *370*, 49–76.
Ji, S., Q. Wang, D. Marcotte, M. H. Salisbury, and Z. Xu (2007), P wave velocities, anisotropy and hysteresis in ultrahigh-pressure metamorphic rocks as a function of confining pressure, *J. Geophys. Res.*, *112*, B09204, doi:10.1029/2006JB004867.
Ji, S., T. Shao, K. Michibayashi, C. Long, Q. Wang, Y. Kondo, W. Zhao, H. Wang, and M. H. Salisbury (2013), A new calibration of seismic velocities, anisotropy, fabrics, and elastic moduli of amphibole-rich rocks, *J. Geophys. Res. Solid Earth*, *118*, 4699–4728, doi:10.1002/jgrb.50352.
Ji, S., T. Shao, M. H. Salisbury, S. Sun, K. Michibayashi, W. Zhao, C. Long, F. Liang, and T. Satsukawa (2014), Plagioclase preferred orientation and induced seismic anisotropy in mafic igneous rocks, *J. Geophys. Res. Solid Earth*, *119*, 8064–8088, doi:10.1002/2014JB011352.
Ji, S., T. Shao, K. Michibayashi, S. Oya, T. Satsukawa, Q. Wang, W. Zhao, and M. Salisbury (2015), Magnitude and symmetry of seismic anisotropy in mica- and amphibole-bearing metamorphic rocks and implications for tectonic interpretation of seismic data from the southeast Tibetan Plateau, *J. Geophys. Res. Solid Earth*, *120*, doi:10.1002/2015JB012209.
Jiang, F., S. Speziale, and T. S. Duffy (2004), Single-crystal elasticity of grossular- and almandine-rich garnets to 11 GPa by Brillouin scattering, *J. Geophys. Res.*, *109*, B10210, doi:10.1029/2004JB002081.
Johnston, J. E., and N. I. Christensen (1995), Seismic anisotropy of shales, *J. Geophys. Res.*, *100*, 5991–6003, doi:10.1029/95JB00031.
Jung, H., J. Lee, B. Ko, S. Jung, M. Park, Y. Cao, and S. Song (2013), Natural type-C olivine fabrics in garnet peridotites in North Qaidam UHP collision belt, NW China, *Tectonophysics*, *594*, 91–102.
Kachanov, M. (1980), Continuum model of medium with cracks, *J. Eng. Mech. Div.*, *106*, 1039–1051.
Kachanov, M. (1987), Elastic solid with many cracks: A simple method of analysis, *Int. J. Solids Struct.*, *23*, 23–43.
Kachanov, M. (1992), Effective elastic properties of cracked solids: Critical review of some basic concepts, *Appl. Mech. Rev.*, *45*, 304–335.
Kachanov, M. (1994), Elastic solids and many cracks and related problems, in *Advances in Applied Mechanics*, vol. 30, edited by J. W. Hutchinson and T. Wu, pp. 259–445, Academic Press, Elsevier.
Kachanov, M., R. Prioul, and J. Jocker (2010), Incremental linear-elastic response of rocks containing multiple rough fractures: Similarities and differences with traction-free cracks, *Geophysics*, *75*, D1–D11.
Kammer, E. W., T. E. Pardue, and H. F. Frissel (1948), A determination of the elastic constants for beta-quartz, *J. Appl. Phys.*, *19*, 265–270, doi:10.1063/1.1715056.
Kandelin, J., and D. J. Weidner (1988a), The single-crystal elastic properties of jadeite, *Phys. Earth Planet. Inter.*, *50*, 251–260.
Kandelin, J., and D. J. Weidner (1988b), Elastic properties hedenbergite, *J. Geophys. Res.*, *93*, 1063–1072, doi:10.1029/JB093iB02p01063.
Kanitpanyacharoen, W., R. Vasin, H.-R. Wenk, and D. N. Dewhurst (2015), Linking preferred orientations to elastic anisotropy in Muderong Shale, Australia, *Geophysics*, *80*, C9–C19.
Karki, B. B., L. Stixrude, and J. Crain (1997), Ab initio elasticity of three high-pressure polymorphs of silica, *J. Geophys. Res.*, *24*, 3269–3272, doi:10.1029/97GL53196.
Katahara, K. W. (1996), Clay mineral elastic properties, Society of Exploration Geophysicists, Annual Meeting Expanded Technical Program Abstracts with Biographies, 66, 1691–1694.
Kendall, J.-M., et al. (2007), Seismic anisotropy as an indicator of reservoir quality in siliciclastic rocks, *Geol. Soc. London, Spec. Publ.*, *292*, 123–136.
Kern, H. (1978), The effect of high temperature and high confining pressure on compressional wave velocities in quartz-bearing and quartz-free igneous and metamorphic rocks, *Tectonophysics*, *44*, 185–203.
Kern, H. (1979), Effect of high-low quartz transition on compressional and shear wave velocities in rocks under high pressure, *Phys. Chem. Miner.*, *4*, 161–171.
Kern, H., and A. Richter (1981), Temperature derivatives of compressional and shear wave velocities in crustal and mantle rocks at 6 kbar confining pressure, *J. Geophys.*, *49*, 47–56.
Kern, H., L. Burlini, and I. V. Ashchepkov (1995), Fabric-related seismic anisotropy in upper-mantle xenoliths: Evidence from measurements and calculations, *Phys. Earth Planet. Inter.*, *95*, 195–209.
Kern, H., S. Gao, and Q.-S. Liu (1996), Seismic properties and densities of middle and lower crustal rocks exposed along the North China Geoscience Transect, *Earth Planet. Sci. Lett.*, *139*, 439–455.
Kern, H., S. Gao, Z. Jin, T. Popp, and S. Jin (1999), Petrophysical studies on rocks from the Dabie ultrahigh-pressure (UHP) metamorphic belt, Central China: Implications for the composition and delamination of the lower crust, *Tectonophysics*, *301*, 191–215.
Kern, H., Z. Jin, S. Gao, T. Popp, and Z. Xu (2002), Physical properties of ultrahigh-pressure metamorphic rocks from the Sulu terrain, eastern central China: Implications for the seismic structure at the Donghai (CCSD) drilling site, *Tectonophysics*, *354*, 315–330.
Kern, H., T. I. Ivankina, A. N. Nikitin, T. Lokajíček, and Z. Pros (2008), The effect of oriented microcracks and crystallographic and shape preferred orientation on bulk elastic anisotropy of a foliated biotite gneiss from Outokumpu, *Tectonophysics*, *457*, 143–149.

Khazanehdari, J., E. H. Rutter, M. Casey, and L. Burlini (1998), The role of crystallographic fabric in the generation of seismic anisotropy and reflectivity of high strain zones in calcite rocks, *J. Struct. Geol.*, *20*, 293–299.
Kimizuka, H., H. Kaburaki, and Y. Kogure (2000), Mechanism for negative Poisson ratios over the α-β transition of cristobalite, SiO_2: A molecular-dynamics study, *Phys. Rev. Lett.*, *24*, 5549–5551.
Kinoshita, N., and T. Mura (1971), Elastic fields of inclusions in anisotropic media, *Phys. Status Solidi A*, *5*, 759–768.
Kitamura, K. (2006), Constraint of lattice-preferred orietatio (LPO) on Vp anisotropy of amphibole-rich rocks, *Geophys. J. Int.*, *165*, 1058–1065.
Kittel, C. (2005), *Introduction to Solid State Physics*, 8th ed., pp. 704, John Wiley.
Klíma, K., and V. Babuška (1968), A comparison of measured and calculated elastic anisotropies of marble, *Stud. Geophys. Geod.*, *12*, 377–384.
Klumbach, S., and F. R. Schilling (2014), Elastic and anelastic properties of α- and β-quartz single crystals, *Eur. J. Mineral.*, *26*, 211–220.
Knittle, E. (1995), Static compression measurements of equations of state, in *Minerals and Crystallography: A Handbook of Physical Constants*, edited by T. J. Ahrens, pp. 98–142, AGU, Washington, D. C.
Kinoshita, N., and T. Mura (1971), Elastic fields of inclusions in anisotropic media, *Phys. Status Solidi (A)*, *5*, 759–768.
Ko, B., and H. Jung (2015), Crystal preferred orientation of an amphibole experimentally deformed by simple shear, *Nat. Commun.*, *6*, doi:10.1038/ncomms7586.
Kumazawa, M. (1964), Application of the finite strain theory to anisotropic minerals: Anisotropy of olivine in the upper mantle, *J. Earth Sci.*, *12*, 177–191.
Kumazawa, M. (1969), The elastic constants of single-crystal orthopyroxene, *J. Geophys. Res.*, *74*, 5973–5980, doi:10.1029/JB074i025p05973.
Kumazawa, M., and O. L. Anderson (1969), Elastic moduli, pressure derivatives, and temperature derivatives of single-crystal olivine and single-crystal forsterite, *J. Geophys. Res.*, *74*, 5961–5972, doi:10.1029/JB074i025p05961.
Kusky, T., B. Windley, and M. Zhai (2007), Tectonic evolution of the North China block: From orogen to craton to orogen, *Geol. Soc. London, Spec. Publ.*, *280*, 1–34.
Lakshtanov, D. L., S. V. Sinogeikin, and J. D. Bass (2007), High-temperature phase transitions and elasticity of silica polymorphs, *Phys. Chem. Miner.*, *34*, 11–22.
Lamarque, G., J. Bascou, C. Maurice, J.-Y. Cottin, N. Riel, and R.-P. Ménot (2016), Microstructuresm deformation mechanisms and seismic properties of a Palaeoproterozoic shear zone: The Mertz shear zone, East-Antarctica, *Tectonophysics*, *680*, 174–191.
Landau, L. L., and E. M. Lifshitz (1959), *Theory of Elasticity*, 134 pp., Pergamon Press.
Le Ravalec, M., and Y. Gueguen (1996), High and low frequency elastic moduli for a saturated porous/cracked rock—Differential self consistent and poroelastic theories, *Geophysics*, *61*, 1080–1094.
Leary, P. C., S. Crampin, and T. V. McEvilly (1990), Seismic fracture anisotropy in the Earth's crust: An overview, *J. Geophys. Res.*, *95*, 11,105–11,114.
Lebedev, A. Y., B. S. Abdurakhmanov, and R. B. Hargraves (1989), *Sov. Phys. Tech. Phys.*, *34*, 231.
Legendre, C. P., F. Deschamps, L. Zhao, and Q.-F. Chen (2015), Rayleigh-wave dispersion reveals crust-mantle decoupling beneath eastern Tibet, *Sci. Rep.*, *5*, doi:10.1038/srep16644.
Lerch, D. W., S. L. Klemperer, J. M. G. Glen, D. A. Ponce, and E. L. Miller (2007), Crustal structure of the northwestern Basin and Range Province and its transition to unextended volcanic plateaus, *Geochem. Geophys. Geosyst.*, *8*, Q02011, doi:10.1029/2006GC001429.
Levien, L., D. J. Weidner, and C. T. Prewitt (1979), Elasticity of diopside, *Phys. Chem. Miner.*, *4*, 105–113.
Lin, F.-C., and B. Schmandt (2014), Upper crustal azimuthal anisotropy across the continuous U.S. determined by Rayleigh wave ellipticity, *Geophys. Res. Lett.*, *41*, 8301–8307, doi:10.1002/2014GL062362.
Lin, J.-F., J. Wu, J. Zhu, Z. Mao, A. H. Said, B. M. Leu, J. Cheng, Y. Uwatoko, C. Jin, and J. Zhou (2014), Abnormal elastic and vibrational behaviors of magnetite at high pressures, *Sci. Rep.*, *4*, 6282, doi:10.1038/srep06282.
Liu, H., and F. Niu (2011), Receiver function study of the crustal structure of northeast China: Seismic evidence for a mantle upwelling beneath the eastern flank of the Songliao Basin and the Changbaishan region, *Earthquake Sci.*, *24*, doi:10.1007/s11589-011-0766-6.
Liu, H., and F. Niu (2012), Estimating crustal seismic anisotropy with a joint analysis of radial and transverse receiver function data, *Geophys. J. Int.*, *188*, 144–164.
Llana-Fúnez, S., and D. Brown (2012), Contribution of crystallographic preferred orientation to seismic anisotropy across a surface analog of the continental Moho at Cabo Ortegal, Spain, *Geol. Soc. Am. Bull.*, *124*, 1495–1513.
Llana-Fúnez, S., D. Brown, R. Carbonell, J. Álvarez-Marrón, and M. Salisbury (2009), Seismic anisotropy of upper mantle-lower continental crust in Cabo Ortegal (NW Spain) from crystallographic preferred orientation (CPO) patterns, *Trab. Geol. (Univ. Oviedo)*, *29*, 432–436.
Lloyd, G. E., and J.-M. Kendall (2005), Petrofabric-derived seismic properties of a mylonitic quartz simple shear zone: Implications for seismic reflection profiling, *Geol. Soc. London, Spec. Publ.*, *240*, 75–94.
Lloyd, G. E., R. W. H. Butler, M. Casey, and D. Mainprice (2009), Mica, deformation fabrics and the seismic properties of the continental crust, *Earth Planet. Sci. Lett.*, *288*, 320–328.
Lloyd, G. E., R. W. H. Butler, M. Casey, D. J. Tatham, and D. Mainprice (2011a), Constraints on the seismic properties of the middle and lower continental crust, *Geol. Soc. London, Spec. Publ.*, *360*, 7–32.
Lloyd, G. E., J. M. Halliday, R. W. H. Butler, M. Casey, J.-M. Kendall, J. Wookey, and D. Mainprice (2011b), From crystal to crustal: Petrofabric-derived seismic modelling of regional tectonics, *Geol. Soc. London, Spec. Publ.*, *360*, 49–78.
Lokajíček, T., H. Kern, T. Svitek, and T. Ivankina (2014), 3D velocity distribution of P- and S waves in a biotite gneiss, measured in oil as the pressure medium: Comparison with velocity measurements in a multi-anvil pressure apparatus and with texture-based calculated data, *Phys. Earth Planet. Inter.*, *231*, 1–15.
Lonardelli, I., H.-R. Wenk, and R. Yen (2007), Preferred orientation and elastic anisotropy in shales, *Geophysics*, *72*(2), D33–D40.
Long, M. D. (2013), Constraints on subduction geodynamics from seismic anisotropy, *Rev. Geophys.*, *51*, 76–112, doi:10.1002/rog.20008.
Long, M. D. (2015), How mountains get made, *Science*, *349*, 687–688.
Long, M. D., A. Levander, and P. M. Shearer (2014), An introduction to the special issue of Earth and Planetary Science Letters on USArray science, *Earth Planet. Sci. Lett.*, *402*, 1–5.
Lui, Y., and D. R. Schmitt (2006), The transition between the scale domains of ray and effective medium theory and anisotropy: Numerical models, *Pure Appl. Geophys.*, *162*, 1–23, doi:10.1007/s00024-006-0075-5.
Madonna, C., B. S. G. Almqvist, and E. H. Saenger (2012), Digital rock physics: Numerical prediction of pressure-dependent velocities using micro-CT imaging, *Geophys. J. Int.*, doi:10.1111/j.1365-246X.2012.05437.x.
Mainprice, D. (1990), A FORTRAN program to calculate seismic anisotropy from the lattice preferred orientation of minerals, *Comput. Geosci.*, *16*, 385–393.

Mainprice, D. (1997), Modelling the anisotropic seismic properties of partially molten rocks found at mid-ocean ridges, *Tectonophysics*, *279*, 161–179.
Mainprice, D. (2000), The estimation of seismic properties of rocks with heterogeneous microstructures using a local cluster model—Preliminary results, *Phys. Chem. Earth*, *25*, 155–161.
Mainprice, D. (2007), Seismic anisotropy of the deep Earth from a mineral and rock physics perspective, in *Treatise in Geophysics*, vol. 2, edited by G. Schubert, pp. 437–492, Elsevier, Oxford.
Mainprice, D. (2015), Seismic anisotropy of the deep Earth from a mineral and rock physics perspective, in *Treatise in Geophysics*, 2nd ed., vol. 2, edited by G. Schubert, pp. 487–539, Elsevier, Oxford.
Mainprice, D., and A. Nicolas (1989), Development of shape and lattice preferred orientations: Application to the seismic anisotropy of the lower crust, *J. Struct. Geol.*, *11*, 175–189.
Mainprice, D., and B. Ildefonse (2009), Seismic anisotropy of subduction zone minerals—Contribution of hydrous phases, in *Subduction Zone Dynamics*, *Front. Earth Sci.*, edited by S. Lallemand and F. Funiciello, pp. 63–84, Springer, Berlin, doi:10.1007/978-3-540-87974-9.
Mainprice, D., and M. Casey (1990), The calculated seismic properties of quartz mylonites with typical fabrics: Relationship to kinematics and temperature, *Geophys. J. Int.*, *103*, 599–608.
Mainprice, D., and M. Humbert (1994), Methods of calculating petrophysical properties from lattice preferred orientation data, *Surv. Geophys.*, *15*, 575–592.
Mainprice, D., G. Barruol, and W. Ben Ismaïl (2000), The seismic anisotropy of the Earth's mantle: From single crystal to polycrystal, in *Earth's Deep Interior: Mineral Physics and Tomography From the Atomic to the Global Scale*, *Geophys. Monogr. Ser.*, vol. 117, pp. 237–264, AGU, Washington, D. C.
Mainprice, D., Y. Le Page, J. Rodgers, and P. Jouanna (2008), Ab initio elastic properties of talc from 0 to 12 GPa: Interpretation of seismic velocities at mantle pressure and prediction of auxetic behaviour at low pressure, *Earth Planet. Sci. Lett.*, *274*, 327–338, doi:10.1016/j.epsl.2008.07.047.
Mainprice, D., R. Hielscher, and H. Schaeben (2011), Calculating anisotropic physical properties from texture data using the MTEX open-source package, *Geol. Soc. London, Spec. Publ.*, *360*, 175–192.
Mainprice, D., F. Bachmann, R. Hielscher, and H. Schaeben (2014), Calculating anisotropic piezoelectric properties from texture data using the MTEX open source package, *Geol. Soc. London, Spec. Publ.*, *409*, doi:10.1144/SP409.2.
Makovsky, Y., and S. L. Klemperer (1999), Measuring the seismic properties of Tibetan bright spots: Evidence for free aqueous fluids in the Tibetan middle crust, *J. Geophys. Res.*, *104*(B5), 10,795–10,825, doi:10.1029/1998JB900074.
Mao, Z., F. Jiang, and T. Duffy (2007), Single-crystal elasticity of zoisite $Ca_2Al_3Si_3O_{12}(OH)$ by Brillouin scattering, *Am. Mineral.*, *92*, 570–576.
Mao, Z., D. Fan, J.-F. Lin, J. Yang, S. N. Tkachev, K. Zhuravlev, and V. B. Prakapenka (2015), Elasticity of single-crystal olivine at high pressures and temperatures, *Earth Planet. Sci. Lett.*, *426*, 204–215.
Marion, D., T. Mukerji, and G. Mavko (1994), Scale effects on velocity dispersion: From ray to effective medium theories in stratified media, *Geophysics*, *59*, 1613–1619.
Matthews, D. H., and the BIRPS group (1990), Progress in BIRPS deep seismic reflection profiling around the British Isles, *Tectonophysics*, *173*, 387–396.
Matthies, S. (2010), On the combination of self-consistent and geometric mean elements for the calculation of the elastic properties textured multi-phase samples, *Solid State Phenom.*, *160*, 87–93.
Matthies, S. (2012), GEO-MIX-SELF calculations of the elastic properties of a textured graphite sample different hydrostatic pressures, *J. Appl. Crystallogr.*, *45*, 1–16.
Matthies, S., and M. Humbert (1993), The realization of the concept of a geometric mean for calculating physical constants of polycrystalline materials, *Phys. Status Solidi B*, *177*, K47–K50.
Matthies, S., and M. Humbert (1995), On the principle of a geometric mean of even-rank symmetric tensors for textured polycrystals, *J. Appl. Crystallogr.*, *28*, 254–266.
Marini, L., and A. Manzella (2005), Possible seismic signature of the alpha-beta quartz transition in the lithosphere of Southern Tuscany (Italy), *J. Volcanol. Geotherm. Res.*, *148*, 81–97.
Mavko, G., T. Mukerji, and J. Dvorkin (2009), *The Rock Physics Handbook*, 2nd ed., pp. 511, Cambridge Univ. Press.
Mechie, J., S. V. Sobolev, L. Ratschbacher, A. Y. Babeyko, G. Bock, A. G. Jones, K. D. Nelson, K. D. Solon, L. D. Brown, and W. Zhao (2004), Precise temperature estimation in the Tibetan crust from seismic detection of the alpha-beta quartz transition, *Geology*, *32*, 601–604.
McLaughlin, R. A. (1977), A study of the differential scheme for composite materials, *Int. J. Eng.*, *15*, 237–244.
McLennan, S. M., and S. R. Taylor (1999), *Earth's continental crust*, Encyclopedia of Geochemistry, 712 pp.
McQuarrie, N., and B. P. Wernicke (2005), An animated tectonic reconstruction of southwestern North America since 36 Ma, *Geosphere*, *1*, 147–172.
McSkimin, H. J. (1950), Ultrasonic measurement techniques applicable to small solid specimens, *J. Acoust. Soc. Am.*, *22*, 413–418.
McSkimin, H. J. (1961), Pulse superposition method for measuring ultrasonic wave velocities in solids, *J. Acoust. Soc. Am.*, *33*, 12, doi:10.1121/1.1908386.
McSkimin, H. J., J. R. Anreatch, and R. N. Thurston (1965), Elastic moduli of quartz vs hydrostatic pressure at 25.0°C and −195.8°C, *J. Appl. Phys.*, *36*, 1624–1635.
Meissner, R., W. Rabbel, and H. Kern (2006), Seismic lamination and anisotropy of the lower continental crust, *Tectonophysics*, *416*, 81–99.
Melia, P. J., and R. L. Carlson (1984), An experimental test of *P*-wave anisotropy in stratified media, *Geophysics*, *49*, 374–378.
Menzies, M., and Y. Xu (1998), Geodynamics of the North China Craton, in *Mantle Dynamics and Plate Interactions in East Asia*, *Geodyn. Ser.*, edited by M. Flower et al., pp. 155–165, AGU, Washington, D. C.
Militzer, B., H.-R. Wenk, S. Stackhouse, and L. Stixrude (2011), First-principles calculation of the elastic moduli of sheet silicates and their application to shale anisotropy, *Am. Mineral.*, *96*, 125–137.
Mookherjee, M., D. Mainprice, K. Maheshwari, O. Heinonen, D. Patel, and A. Hariharan (2016), Pressure induced elastic softening in framework aluminosilicate-albite ($NaAlSi_3O_8$), *Sci. Rep.*, *6*, doi:10.1038/srep34815.
Mooney, W. D. (2015), Crust and lithospheric structure—Global crustal structure, in *Treatise of Geophysics*, 2nd ed., vol. 1, pp. 339–390, Elsevier, Amsterdam.
Mooney, W. D., and R. Meissner (1992), Multi-genetic origin of crustal reflectivity: A review of seismic reflection profiling of the continental lower crust and Moho, in *Continental Lower Crust*, vol. 23, edited by D. M. Fountain, R. Arculus, and R. W. Kay, pp. 45–79, Elsevier, Amsterdam.
Morawiec, A. (1989), Calculation of polycrystal elastic constants from single-crystal data, *Phys. Status Solidi B*, *154*, 535–541.

Moschetti, M. P., M. H. Ritzwoller, F. Lin, and Y. Yang (2010), Seismic evidence for widespread western-US deep-crustal deformation caused by extension, *Nature*, *464*, 885–890, doi:10.1038/nature08951.
Müller, T. M., B. Gurevich, and M. Lebedev (2010), Seismic wave attenuation and dispersion resulting from wave-induced flow in porous rocks—A review, *Geophysics*, *75*, 75A147–75A164.
Mura, T. (1987), *Micromechanics of Defects in Solids*, 2nd ed., pp. 587, Kluwer Acad., Dordrecht, Netherlands.
Nábělek, J., et al. (2009), Underplating in the Himalaya-Tibet collision zone revealed by the Hi-CLIMB experiments, *Science*, *325*, 1371–1374.
Naus-Thijssen, F. M. J., A. J. Goupee, S. S. Vel, and S. E. Johnson (2011a), The influence of microstructure on seismic wave speed anisotropy in the crust: Computational analysis of quartz-muscovite rocks, *Geophys. J. Int.*, *185*, 609–621.
Naus-Thijssen, F. M. J., A. J. Goupee, S. E. Johnson, S. S. Vel, and C. Gerbi (2011b), The influence of crenulation cleavage development on the bulk elastic and seismic properties of phyllosilicate-rich rocks, *Earth Planet. Sci. Lett.*, *311*, 212–224.
Nelson, K. D., et al. (1996), Partially molten middle crust beneath Southern Tibet: Synthesis of project INDEPTH results, *Science*, *274*, 1684–1688.
Nesbitt, H. W., and G. M. Young (1984), Prediction of some weathering trends of plutonic and volcanic rocks based on thermodynamic and kinetic considerations, *Geochim. Cosmochim. Acta*, *48*, 1523–1534.
Nishizawa, O., and T. Yoshino (2001), Seismic velocity anisotropy in mica-rich rocks: An inclusion model, *Geophys. J. Int.*, *145*, 19–32.
Nye, J. F. (1957), *Physical Properties of Crystals*, pp. 322, Oxford Univ. Press.
O'Connell, R. J., and B. Budiansky (1974), Seismic velocities in dry and saturated cracked solids, *J. Geophys. Res.*, *79*, 4626–4627, doi:10.1029/JB079i035p05412.
Ogi, H., Ohmori, T., Nakamura, N., and M. Hirao (2006), Elastic, anelastic, and piezoelectric coefficients of α-quartz determined by resonance ultrasound spectroscopy, *J. Appl. Phys.*, *100*, 053511, doi:10.1063/1.2335684.
Ohno, I., K. Harada, and C. Yoshitomi (2006), Temperature variation of elastic constants of quartz across the α-β transition, *Phys. Chem. Miner.*, *33*, 1–9.
Oliver, J., M. Dobrin, S. Kaufman, R. Meyer, and R. Phinney (1976), Continuous seismic reflection profiling of the deep basement, Hardeman County, Texas, *Geol. Soc. Am. Bull.*, *87*, 1537–1546.
Ozacar, A. A., and G. Zandt (2009), Crustal structure and seismic anisotropy near the San Andreas Fault at Parkfield, California, *Geophys. J. Int.*, *178*, 1098–1104.
Özkan, H., and J. C. Jamieson (1978), Pressure dependence of the elastic constants of nonmetamict zircon, *Phys. Chem. Miner.*, *2*, 215–224.
Özkan, H., L. Cartz, and J. C. Jamieson (1974), Elastic constants of nonmetamict zirconium silicate, *J. Appl. Phys.*, *45*, 556–562.
Paaschier, C. W., and R. Trouw (2005), *Microtectonics*, pp. 366, Springer, Heidelberg, Berlin.
Pacalo, R. E., and D. J. Weidner (1997), Elasticity of majorite, $MgSiO_3$ tetragonal garnet, *Phys. Earth Planet. Int.*, *99*, 145–154.
Paterson, M., and T.-F. Wong (2005), *Experimental Rock Deformation—The Brittle Field*, pp. 347, Springer, Berlin.
Peselnick, L., A. Nicolas, and P. R. Stevenson (1974), Velocity anisotropy in a mantle peridotite from the Ivrea zone: Application to upper mantle anisotropy, *J. Geophys. Res.*, *79*, 1175–1182, doi:10.1029/JB079i008p01175.
Phillips, F. C. (1938), Mineral orientation in some olivine-rich rocks from Rum and Skye, pp. 130–135, Cambridge Univ. Press.
Postma, G. W. (1955), Wave propagation in a stratified medium, *Geophysics*, *20*, 780–806.
Pratt, T. L., E. C. Hauser, T. M. Hearn, and T. J. Reston (1991), Reflection polarity of the midcrustal Surrency bright spot beneath southeasten Georgia: Testing the fluid hypothesis, *J. Geophys. Res.*, *96*, 10,145–10,158, doi:10.1029/91JB00766.
Prior, D. J., et al. (1999), The application of electron backscatter diffraction and orientation contrast imaging in the SEM to textural problems in rocks, *Am. Mineral.*, *84*, 1741–1759.
Pros, Z., T. Lokajíček, and K. Klíma (1998), Laboratory approach to the study of elastic anisotropy on rock samples, *Pure Appl. Geophys.*, *151*, 619–629.
Pros, Z., T. Lokajíček, R. Přikryl, and K. Klíma (2003), Direct measurement of 3D elastic anisotropy on rocks from the Ivrea Zone (Southern Alps, NW Italy), *Tectonophysics*, *370*, 31–47.
Ranganathan, S. I., and M. Ostoja-Starzewski (2008), Universal elastic anisotropy index, *Phys. Rev. Lett.*, *101*, doi:10.1103/PhysRevLett.101.055504.
Rawlinson, N., and S. Fishwick (2011), Seismic structure of the southeast Australian lithosphere from surface and body wave tomography, *Tectonophysics*, doi:10.1016/j.tecto.2011.11.016.
Reichmann, H. J., and S. D. Jacobsen (2004), High-pressure elasticity of a natural magnetite crystal, *Am. Mineral.*, *89*, 1061–1066.
Reuss, A. (1929), Berechnung der Fliessgrenze von Mischkristallen auf Grund der Plastizitätsbedingung für Einkristalle, *Z. Angew. Math. Mech.*, *9*, 49–58.
Rey, P. F., D. M. Fountain, and W. P. Clement (1994), P wave velocity across a noncoaxial ductile shear zone and its associated strain gradient: Consequences for upper crustal reflectivity, *J. Geophys. Res.*, *99*, 4533–4548, doi:10.1029/93JB03105.
Riznichenko, Y. V. (1949), On seismic quasi-anisotropy, *Izv. Akad. Nauk. SSSR, Geograf. Geofiz.*, *13*, 518–544.
Ronov, A. B., and A. A. Yaroshev (1967), Chemical structure of Earths crust, *Geochem. Int. USSR*, *4*(6), 1041.
Royden, L., B. C. Burchfiel, R. W. King, E. Wang, Z. Chen, F. Shen, and Y. Liu (1997), Surface deformation and lower crustal flow in eastern Tibet, *Science*, *276*, 788–790.
Rudnick, R., and D. Fountain (1995), Nature and composition of the continental crust: A lower crustal perspective, *Rev. Geophys.*, *33*, 267–309, doi:10.1029/95RG01302.
Rudnick, R., and S. Gao (2003), Composition of the continental crust, *Treatise Geochem.*, *3*, 1–64.
Rudnick, R., and S. Gao (2014), Composition of the continental crust, in *The Crust*, *Treatise Geochem.*, 2nd ed., vol. 4, pp. 1–51, Elsevier, Amsterdam.
Rümpker, G., A. Kaviani, and K. Latifi (2014), Ps-splitting analysis for multilayered anisotropic media by azimuthal stacking and layer stripping, *Geophys. J. Int.*, *199*, 146–163.
Ryzhova, T. V. (1964), Elastic properties of plagioclases, *Akad. SSSR Izv. Ser. Geofiz.*, *7*, 1049–1051.
Ryzhova, T. V., and K. S. Aleksandrov (1965), The elastic properties of potassiun-sodium feldspars. Izvestiya of the Academy of Sciences, USSR, 89-102, Earth Physics Series, Physics of the Soldid Earth [English translation], vol. 1, pp. 53–56.
Ryzhova, T. V., K. S. Aleksandrov, and V. M. Korobkova (1966), The elastic properties of rock-forming minerals: V. Additional data on silicates, *Izu. Earth Phys.*, *2*, 63–65.
Sang, L., and J. D. Bass (2014), Single-crystal elasticity of diopside to 14 GPa by Brillouin scattering, *Phys. Earth Planet. Inter.*, *228*, 75–79.
Satsukawa, T., B. Ildefonse, D. Mainprice, L. F. G. Morales, K. Michibayashi, and F. Barou (2013), A database of plagioclase crystal preferred orientations (CPO) and microstructures—Implications for CPO origin, strength, symmetry and seismic anisotropy in gabbroic rocks, *Solid Earth*, *4*, 511–542.

Savage, M. (1999), Seismic anisotropy and mantle deformation: What have we learned from shear wave splitting?, *Rev. Geophys.*, *37*, 65–106, doi:10.1029/98RG02075.
Sayers, C. M. (1999), Stress-dependent seismic anisotropy of shales, *Geophysics*, *64*, 93–98.
Sayers, C. M. (2005), Seismic anisotropy of shales, *Geophys. Prospect.*, *33*, 667–676.
Sayers, C. M. (2009), Seismic characterization of reservoirs containing multiple fracture sets, *Geophys. Prospect.*, *57*, 187–192.
Sayers, C. M., and M. Kachanov (1991), A simple technique for finding effective elastic constants of cracked solids for arbitrary crack orientation statistics, *Int. J. Solids Struct.*, *12*, 81–97.
Sayers, C. M., and M. Kachanov (1995), Microcrack-induced elastic wave anisotropy, *J. Geophys. Res.*, *100*, 4149–4156, doi:10.1029/94JB03134.
Schilling, F. R., S. V. Sinogeikin, and J. D. Bass (2003), Single-crystal elastic properties of lawsonite and their variation with temperature, *Phys. Earth Planet. Inter.*, *136*, 107–118.
Schoenberg, M. A. (1980), Elastic wave behavior across linear slip interfaces, *J. Acoust. Soc. Am.*, *68*, 1516–1521.
Schoenberg, M. A., and C. M. Sayers (1995), Seismic anisotropy of fractured rock, *Geophysics*, *60*, 204–211.
Schoenberg, M. A., and J. Douma (1988), Elastic wave propagation in media with parallel fractures and aligned cracks, *Geophys. Prospect.*, *36*, 571–590, doi:10.1111/j.1365-2478.1988.tb02181.x.
Schoenberg, M., and F. Muir (1989), A calculus for finely layered anisotropic media, *Geophysics*, *54*, 581–589.
Schubnel, A., and Y. Guéguen (2003), Dispersion and anisotropy of elastic waves in cracked rocks, *J. Geophys. Res.*, *108*(B2), 2101, doi:10.1029/2002JB001824.
Schubnel, A., O. Nishizawa, K. Masuda, X. J. Lei, Z. Xue, and Y. Gueguen (2003), Velocity measurements and crack density determination during wet triaxial experiments on Oshima and Toki granites, *Pure Appl. Geophys.*, *160*, 869–887.
Schulte-Pelkum, V., and K. H. Mahan (2014), A method for mapping crustal deformation and anisotropy with receiver functions and first results from USArray, *Earth Planet. Sci. Lett.*, *402*, 221–233, doi:10.1016/j.epsl.2014.01.050.
Schulte-Pelkum, V., G. Monsalve, A. Sheehan, M. R. Pandey, S. Sapkota, R. Bilham, and F. Wu (2005), Imaging the Indian subcontinent beneath Himalaya, *Nature*, *435*, 1222–1225.
Seront, B., D. Mainprice, and N. I. Christensen (1993), A determination of the three-dimensional seismic properties of anorthosite: Comparison between values calculated from the petrofabric and direct laboratory measurements, *J. Geophys. Res.*, *98*, 2209–2221, doi:10.1029/92JB01743.
Sha, M. C., Z. Li, and R. C. Bradt (1994), Single-crystal elastic constants of fluorapatite, Ca5F(PO4)3, *J. Appl. Phys.*, *75*, 7784, doi:10.1063/1.357030.
Shao, T., S. Ji, S. Oya, K. Michibayashi, and Q. Wang (2016), Mica-dominated seismic properties of mid-crust beneath west Yunnan (China) and geodynamic implications, *Tectonophysics*, *677–678*, 324–338.
Shapiro, N. M., M. H. Ritzwoller, P. Molnar, and V. Levin (2004), Thinning and flow of Tibetan crust constrained by seismic anisotropy, *Science*, *305*, 233–236.
Sherrington, H. F., G. Zandt, and A. Fredriksen (2004), Crustal fabric in the Tibetan Plateau based on waveform inversions for seismic anisotropy parameters, *J. Geophys. Res.*, *109*, B02312, doi:10.1029/2002JB002345.
Siegesmund, S., T. Takeshita, and H. Kern (1989), Anisotropy of V_p and V_s in an amphibolite of the deeper crust and its relationship to the mineralogical, microstructural and textural characteristics of the rock, *Tectonophysics*, *157*, 25–38.
Silver, P. G. (1996), Seismic anisotropy beneath the continents: Probing the depths of geology, *Annu. Rev. Earth Planet. Sci.*, *24*, 385–432.
Simmons, G., and F. Birch (1963), Elastic constants of pyrite, *J. Appl. Phys.*, *34*, 2736–2738.
Sinogeikin, S. V., and J. D. Bass (2002), Elasticity of pyrope and majorite-pyrope solid solutions to high temperatures, *Earth Planet. Sci. Lett.*, *203*, 549–555.
Sinogeikin, S. V., F. R. Schilling, and J. D. Bass (2000), Single crystal elasticity of lawsonite, *Am. Mineral.*, *85*, 1834–1837.
Skemer, P., and L. Hansen (2016), Inferring upper-mantle flow from seismic anisotropy: An experimental perspective, *Tectonophysics*, *668–669*, 1–14.
Slepko, A., and A. A. Demkov (2011), First-principles study of the biomineral hydroxylapatite, *Phys. Rev. B*, *84*, doi:10.1103/PhysRevB.84.134108.
Soga, N. (1967), Elastic constants of garnet under pressure and temperature, *J. Geophys. Res.*, *72*, 4227–4234, doi:10.1029/JZ072i016p04227.
Speziale, S., T. S. Duffy, and R. J. Angel (2004), Single-crystal elasticity of fayalite to 12 GPa, *J. Geophys. Res.*, *109*, B12202, doi:10.1029/2004JB003162.
Sumino, Y. (1979), The elastic constants of Mn_2SiO_4, Fe_2SiO_4 and Co_2SiO_4 and the elastic properties olivine group minerals at high temperature, *J. Phys. Earth*, *27*, 209–238.
Sumino, Y., and O. L. Anderson (1984), Elastic constants of minerals, in *Handbook of Physical Propertiesm: III*, edited by R. S. Carmichael, pp. 39–138, CRC Press, Boca Raton, Fla.
Tatham, D. J., G. E. Lloyd, R. W. H. Butler, and M. Casey (2008), Amphibole and lower crustal seismic properties, *Earth Planet. Sci. Lett.*, *267*, 118–128.
Tian, Y., D. Zhao, R. Sun, and J. Teng (2009), Seismic imaging of the crust and upper mantle beneath the North China Craton, *Phys. Earth Planet. Inter.*, *172*, 169–182.
Todd, T., and G. Simmons (1972), Effect of pore pressure velocity of compressional waves in low-porosity rocks, *J. Geophys. Res.*, *77*, 3731–3743.
Toohill, K., S. Siegesmund, and J. D. Bass (1999), Sound velocities and elasticity of cordierite and implications for deep crustal seismic anisotropy, *Phys. Chem. Miner.*, *26*, 333–343.
Turner, F. J. (1942), Preferred orientation of olivine crystals in peridotites, with special reference to New Zealand examples, *Trans. R. Soc. New Zealand*, *72*, 280–300.
Ullemeyer, K., D. I. Niklayev, N. I. Christensen, and J. H. Behrmann (2011), Evaluation of intrinsic velocity-pressure trends from low-pressure *P*-wave velocity measurements in rocks containing microcracks, *Geophys. J. Int.*, *185*, 1312–1320.
Vakulenko, A. A., and M. Kachanov (1971), Continuum theory of medium with cracks, *Mehanika Tverd. Tela*, *6*, 159–166.
Valcke, S. L. A., M. Casey, G. E. Lloyd, J.-M. Kendall, and Q. J. Fisher (2006), Lattice preferred orientation and seismic anisotropy in sedimentary rocks, *Geophys. J. Int.*, *166*, 652–666.
Vasin, R. N., H.-R. Wenk, W. Kanitpanyacharoen, S. Matthies, and R. Wirth (2013), Elastic anisotropy modelling of Kimmeridge shale, *J. Geophys. Res. Solid Earth*, *118*, 3931–3956, doi:10.1002/jgrb.50259.
Vasin, R. N., H. Kern, T. Lokajíček, T. Svitek, E. Lehmann, D. C. Mannes, M. Chaouche, and H.-R. Wenk (2017), Elastic anisotropy of Tambo gneiss from Promontogno, Switzerland: A comparison of crystal orientation and microstructure-based modelling and experimental measurements, *Geophys. J. Int.*, *209*, 1–20.

Vaughan, M. T., and J. D. Bass (1983), Single crystal elastic properties of protoenstatite: A comparison with orthoenstatite, *Phys. Chem. Miner.*, *10*, 62–68.
Vaughan, M. T., and S. Guggenheim (1986), Elasticity of muscovite and its relationship to crystal structure, *J. Geophys. Res.*, *91*, 4657–4664, doi:10.1029/JB091iB05p04657.
Vaughan, M. T., and D. J. Weidner (1978), The relationship of elasticity and crystal structure in andalusite and sillimanite, *Phys. Chem. Miner.*, *3*, 133–144.
Vel, S., A. C. Cook, S. E. Johnson, and C. Gerbi (2016), Computational homogenization and micromechanical analysis of textured polycrystalline materials, *Comput. Methods Appl. Mech. Eng.*, *310*, 749–779.
Verma, R. K. (1960), Elasticity of some high-density crystals, *J. Geophys. Res.*, *65*, 757–766, doi:10.1029/JZ065i002p00757.
Voigt, W. (1928), *Lehrbuch der Kristallphysik*, Teubner-Verlag, Leipzig.
Wachtman, J. B., Jr., W. E. Tefft, and D. G. Lam Jr. (1962), Elastic constants of rutile (TiO_2), *J. Res. Natl. Bur. Stand., Sect. A*, *66*, 465–471.
Walker, A. M. (2012), The effect of pressure on the elastic properties and seismic anisotropy of diopside and jadeite from atomic scale simulation, *Phys. Earth Planet. Int.*, *192–193*, 81–89.
Walker, A. M., and J. Wookey (2012), MSAT—A new toolkit for the analysis of elastic and seismic anisotropy, *Comput. Geosci.*, *49*, 81–90.
Walsh, J. B. (1965), The effect of cracks on the compressibility of rock, *J. Geophys. Res.*, *70*, 381–389, doi:10.1029/JZ070i002p00381.
Walsh, J. B. (1969), New analysis of attenuation in partially melted rocks, *J. Geophys. Res.*, *74*, 4333–4337, doi:10.1029/JB074i017p04333.
Wang, H. (2000), *Theory of Linear Poroelasticity With Applications to Geomechanics and Hydrogeology*, pp. 304, Princeton Univ. Press, Princeton, N. J.
Wang, Z. (2002), Seismic anisotropy in sedimentary rocks, part 2: Laboratory data, *Geophysics*, *67*(5), 1423–1440.
Wang, J., Z. Mao, F. Jiang, and T. S. Duffy (2015), Elasticity of single-crystal quartz to 10 GPa, *Phys. Chem. Miner.*, *42*, 203–212, doi:10.1007/s00269-014-0711-z.
Wang, N., J.-P. Montagner, A. Fichtner, and Y. Capdeville (2013), Intrinsic versus extrinsic seismic anisotropy: The radial anisotropy in reference Earth models, *Gephys. Res. Lett.*, *40*, 4284–4288, doi:10.1002/grl.50873.
Wang, Q., S. Ji, M. H. Salisbury, B. Xia, M. Pan, and Z. Xu (2005a), Pressure dependence and anisotropy of P-wave velocities in ultrahigh-pressure metamorphic rocks from the Dabie-Sulu orogenic belt (China): Implications for seismic properties of subducted slabs and origin of mantle reflections, *Tectonophysics*, *398*, 67–99.
Wang, Q., S. C. Ji, M. H. Salisbury, M. B. Xia, B. Pan, and Z. Q. Xu (2005b), Shear wave properties and Poisson's ratios of ultrahigh-pressure metamorphic rocks from the Dabie-Sulu orogenic belt: Implications for the crustal composition, *J. Geophys. Res.*, *110*, B08208, doi:10.1029/2004JB003435.
Wang, Q., L. Burlini, D. Mainprice, and Z. Xu (2009), Geochemistry, petrofabrics and seismic properties of eclogites from the Chinese Continental Scientific Drilling boreholes in the Sulu UHP terrane, eastern China, *Tectonophysics*, *475*, 251–266.
Ward, D., K. Mahan, and V. Schulte-Pelkum (2012), Roles of quartz and mica in seismic anisotropy of mylonites, *Geophys. J. Int.*, *190*, 1123–1134, doi:10.1111/j.1365-246X.2012.05528.x.
Warner, M. (1990), Absolute reflection coefficients from deep seismic reflections, *Tectonophysics*, *173*, 15–23.
Waeselmann, N., J. M. Brown, R. J. Angel, N. Ross, J. Zhao, and W. Kaminsky (2016), The elastic tensor of monoclinic alkali feldspars, *Am. Mineral.*, *101*, 1228–1231.
Webb, S. L., and I. Jackson (1993), The pressure dependence of the elastic moduli of single-crystal orthopyroxene ($Mg_{0.8}Fe_{0.2}$)SiO_3, *Eur. J. Mineral.*, *5*, 1111–1119.
Webb, S. L., I. Jackson, and H. Takei (1984), On the absence of shear mode softening in single-crystal fayalite Fe_2SiO_4 at high pressure and room temperature, *Phys. Chem. Miner.*, *11*, 167–171.
Weidner, D. J., and E. Ito (1985), Elasticity of $MgSiO_3$ in the ilmenite phase, *Phys. Earth Planet. Inter.*, *40*, 65–70.
Weidner, D. J., and H. R. Carleton (1977), Elasticity of coesite, *J. Geophys. Res.*, *82*, 1334–1346.
Weidner, D. J., H. Wang, and J. Ito (1978), Elasticity of orthoenstatite, *Phys. Earth Planet. Inter.*, *17*, P7–P13.
Weidner, D. J., J. D. Bass, A. E. Ringwood, and W. Sinclair (1982), The single-crystal elastic moduli of stishovite, *J. Geophys. Res.*, *87*, 4740–4746, doi:10.1029/JB087iB06p04740.
Weiss, T., S. Siegesmund, W. Rabbel, T. Bohlen, and M. Pohl (1999), Seismic velocities and anisotropy of the lower continental crust: A review, *Pure Appl. Geophys.*, *156*, 97–122.
Wenk, H.-R., and A. Bulakh (2004), *Minerals: Their Constitution and Origin*, pp. 646, Cambridge Univ. Press, Cambridge, U. K.
Wenk, H.-R., I. Lonardelli, H. Franz, K. Nihei, and S. Nakagawa (2007), Preferred orientation and elastic anisotropy of illite-rich shale, *Geophysics*, *72*(2), E69–E75.
Wenk, H.-R., R. N. Vasin, H. Kern, S. Matthies, S. C. Vogel, and T. I. Ivankina (2012), Revisiting elastic anisotropy of biotite gneiss from the Outokumpu scientific drill hole based on new texture measurements and texture-based velocity calculations, *Tectonophysics*, *570–571*, 123–134.
Wenning, Q., B. S. G. Almqvist, P. Hedin, and A. Zappone (2016), Seismic anisotropy in mid to lower orogenic crust: Insights from laboratory measurements of V_p and V_s in drill core from central Scandinavian Caledonides, *Tectonophysics*, doi:10.1016/j.tecto.2016.07.002.
Wepfer, W. W., and N. I. Christensen (1991), A seismic velocity-confining pressure relation, with applications, *Int. J. Min. Sci. Geomech. Abstr.*, *28*, 451–456.
Wernicke, B. P. (1981), Low-angle normal faults in the Basin and Range Province: Nappe tectonics in an extending orogen, *Nature*, *291*, 645–648.
Wernicke, B. P., G. J. Axen, and J. K. Snow (1988), Basin and Range extensional tectonics at the latitude of Las Vegas, Nevada, *Geol. Soc. Am. Bull.*, *100*, 1738–1757.
Willis, J. R. (1977), Bounds and self-consistent estimates for the overall properties of anisotropic composites, *J. Mech. Phys. Solids*, *25*, 185–202.
Winkler, B., M. Hytha, M. C. Warren, V. Milman, J. D. Gale, and J. Schreuer (2001), Calculation of the elastic constants of the Al2SiO5 polymorphs andalusite, sillimanite and kyanite, *Zeitschrift für Kristallographie*, doi:10.1524/zkri.216.2.67.20336.
Worthington, J. R., B. R. Hacker, and G. Zandt (2013), Distinguishing eclogite from peridotites: EBSD-based calculations of seismic velocities, *Geophys. J. Int.*, *193*, 489–505, doi:10.1093/gji/ggt004.
Wu, F. T., H. Kuo-Chen, and K. D. McIntosh (2014), Subsurface imaging, TAIGER experiments and tectonic models of Taiwan, *J. Asian Earth Sci.*, *90*, 173–208.
Wu, T. T. (1966), The effect of inclusion shape on the elastic moduli of a two-phase material, *Int. J. Solids Struct.*, *2*, 1–18.
Wyllie, M. R. J., A. R. Gregory, and G. H. F. Gardner (1958), An experimental investigation of factors affecting elastic wave velocities in porous media, *Geophysics*, *23*, 459–493.

Xie, J., M. H. Ritzwoller, W. Shen, Y. Yang, Y. Zheng, and L. Zhou (2013), Crustal radial anisotropy across Eastern Tibet and the Western Yangtze Craton, *J. Geophys. Res. Solid Earth*, *118*, 4226–4252, doi:10.1002/jgrb.50296.

Xie, J., M. H. Ritzwoller, S. J. Brownlee, and B. R. Hacker (2015), Inferring the oriented elastic tensor from surface wave observations: Preliminary application across the western United States, *Geophys. J. Int.*, *201*, 996–1021.

Xu, Z., Q. Wang, S. Ji, J. Chen, L. Zeng, J. Yang, F. Chen, F. Liang, and H.-R. Wenk (2006), Petrofabrics and seismic properties of garnet peridotite from the UHP Sulu terrane (China): Implications for olivine deformation mechanism in a cold and dry subducting continental slab, *Tectonophysics*, *421*, 111–127.

Yeganeh-Haeri, A., D. J. Weidner, and J. B. Parise (1992), Elasticity of alpha-cristobalite: A silicon dioxide with negative Poisson's ratio, *Science*, *257*, 650.

Zappone, A., and P. M. Benson (2013), Effect of phase transitions on seismic properties of metapelites: A new high-temperature laboratory calibration, *Geology*, *41*, 463–466.

Zhang, J. S., and J. D. Bass (2016a), Single crystal elasticity of natural Fe-bearing orthoenstatite across a high-pressure phase transition, *Geophys. Res. Lett.*, *43*, 8473–8481, doi:10.1002/2016GL069963.

Zhang, J. S., and J. D. Bass (2016b), Sound velocities of olivine and high pressures and temperatures, and composition of Earth's upper mantle, *Geophys. Res. Lett.*, *43*, 9611–9618, doi:10.1002/2016GL069949.

Zhao, W., K. D. Nelson, and Project INDEPTH Team (1993), Deep seismic reflection evidence for continental underthrusting beneath southern Tibet, *Nature*, *366*, 557–559.

Zhong, X., M. Frehner, K. Kunze, and A. Zappone (2014), A novel EBSD-based finite-element wave propagation model for investigating seismic anisotropy: Application to Finero Peridotite, Ivrea-Verbano Zone, Northern Italy, *Geophys. Res. Lett.*, *41*, 7105–7114, doi:10.1002/2014GL060490.

Zhong, X., M. Frehner, K. Kunze, and A. S. Zappone (2015), A numerical and experimental investigation on seismic anisotropy of Finero peridotites, Ivrea-Verbano Zone, Northern Italy, *IOP Conf. Ser.: Mater. Sci. Eng.*, *82*, doi:10.1088/1757-899X/82/1/012072.

Zimmerman, R. W., W. H. Somerton, and M. S. King (1986), Compressibility of porous rocks, *J. Geophys. Res.*, *91*, 12,765–13,277, doi:10.1029/JB091iB12p12765.